# DYNAMICS OF THE HYDROGEN EXCHANGE REACTION USING THE PHOTOLOC TECHNIQUE

A DISSERTATION
SUBMITTED TO THE DEPARTMENT OF CHEMISTRY
AND THE COMMITTEE ON GRADUATE STUDIES
OF STANFORD UNIVERSITY
IN PARTIAL FULFILLMENT OF THE REQUIREMENTS
FOR THE DEGREE OF
DOCTOR OF PHILOSOPHY

Félix Fernández-Alonso
September 1999

I certify that I have read this dissertation and that in my opinion it is fully adequate, in scope and quality, as a dissertation for the degree of Doctor of Philosophy.

Richard N. Zare
(Principal Adviser)

I certify that I have read this dissertation and that in my opinion it is fully adequate, in scope and quality, as a dissertation for the degree of Doctor of Philosophy.

John Ross

I certify that I have read this dissertation and that in my opinion it is fully adequate, in scope and quality, as a dissertation for the degree of Doctor of Philosophy.

Michael D. Fayer

Approved for the University Committee on Graduate Studies:

# Abstract

The dynamics of the $H + D_2$ exchange reaction has been studied experimentally using laser, velocity-sensitive time-of-flight (TOF) methods. These measurements are performed by expanding a mixture of a photolytic precursor and the $D_2$ reagent with a pulsed supersonic nozzle into a vacuum chamber. Laser photolysis generates a monoenergetic population of H atoms, initiating the chemical reaction. The measured collision energy spread is 50 meV. $HD(v', J')$ products are detected via (2+1) resonance-enhanced multiphoton ionization (REMPI) inside a Wiley-McLaren time-of-flight spectrometer. Integral cross section measurements are performed by measuring the total ion yield into different product rovibrational states. In addition, core extraction of the ion packet prior to detection allows an unambiguous inversion of the laboratory product velocity distribution into a corresponding center-of-mass differential cross section with an angular resolution of 3–15°.

We describe in detail the procedures followed for the calibration of the time-of-flight instrument using known, single-speed atomic or molecular sources. These procedures include: HBr photolysis; $O_2$ photolysis; and the $H + HBr$ reaction which generates $H_2$ at a single laboratory speed. Detailed procedures are also given on how the reaction conditions were characterized and the experimental conditions improved to enable a reliable measurement of integral and differential cross sections of the nascent reaction product.

The measured rotational distributions for the $HD(v' = 1, 2, J')$ vibrational manifolds at collision energies ca. 1.6 eV agree closely with quasiclassical trajectory calculations. These distributions are colder than the "prior" or statistical limit indicating that other constraints besides energy conservation are dictating energy disposal

into the rotational degree of freedom of the diatomic product. Further insight into the dynamics of this reaction is given by the differential cross section measurements into particular $\mathrm{HD}(\mathrm{v}' = 1, \mathrm{J}')$ and $\mathrm{HD}(\mathrm{v}' = 2, \mathrm{J}')$ quantum states. In each vibrational manifold, the product angular distributions are completely backward scattered for low-$\mathrm{J}'$ states, and they shift toward side scattering as the rotational excitation of the product increases. Experimental data at a lower angular resolution for $\mathrm{HD}(\mathrm{v}' = 3, \mathrm{J}')$ also show a similar trend in the angular distributions. The differential cross section data can be qualitatively explained by invoking a line-of-centers with nearly elastic specular scattering model which links the most probable scattering angle for a given $\mathrm{HD}(\mathrm{v}', \mathrm{J}')$ product state with initial impact parameter. Within the framework of this model, the angular distributions for $\mathrm{HD}(\mathrm{v}' = 1, \mathrm{J}')$ and $\mathrm{HD}(\mathrm{v}' = 2, \mathrm{J}')$ only show differences that can be attributed to a smaller hard-sphere radius leading to the more vibrationally excited product. Moreover, this model is capable of predicting from the differential cross section data alone the maximum product rotational excitation for a given vibrational level that agrees well with the observed rotational distributions. Analysis of the experimental data recorded by Schnieder and co-workers at 1.29 eV for the same reaction system shows very similar trends in both the integral and differential cross sections, an indication that similar dynamics are governing the outcome of this chemical reaction at this lower collision energy.

*A mis padres, Joaquín y Maria Teresa*

*The known is finite, the unknown infinite; spiritually we find ourselves on a tiny island in the middle of a boundless ocean of the inexplicable.*
*It is our task, from generation to generation, to drain a small amount of additional land.*

*T. Huxley*

# Acknowledgments

Many people have contributed to the work I will present in this thesis, both from a professional and a personal standpoint.

First, I would like to acknowledge and thank my parents Joaquín and Maria Teresa for their unconditional support and love during my years away from home. This August it is going to be a decade since I left Spain. Despite the long distance that have separated us for so long they have always been there for me. It is my sincere hope that someday I will be able to repay what I have been given by them. My many thanks to my brothers Joaquín and Rodrigo, and sister Maite. They were probably too young at the time to realize they would not be able to count on my presence during their teens. Sorry for not being there.

The first person who probably hinted at my passion for the study of elementary chemical reactions was Prof. Carl Trindle. I worked with Carl during the Summer of 1992 at the University of Virginia doing computational chemistry. On numerous occasions, I was "caught" sitting by his extensive scientific library reading Levine and Bernstein's *Molecular Reaction Dynamics and Chemical Reactivity*. By the end of my stay in Charlottesville, he left on my desk a dedicated copy of this book. That, I think, marked the beginning of it.

I owe a great deal to Dr. George A. Raiche, who took me during his sabbatical year to work at the Molecular Physics Laboratory, SRI International. At SRI, I had the pleasure to be initiated to the world of experimental physical chemistry and laser spectroscopy. Thanks for giving me this splendid opportunity. I also had the support (and patience!) of many people in the laser-based diagnostics group: David R. Crosley, Jay B. Jeffries, Gregory P. Smith, Ulf Westblom and Jorge Luque. In a

time I was not sure about my immediate future they decided to "push" me into the graduate school adventure.

My friends and colleages at the Department of Chemistry and the Zarelab have also been a source of both inspiration and support. Special thanks go to my classmates Néstor Rodríguez, Danny Hughes, and Mike Everest (Yes Mike, after Alex I am the second one on your list of LaTeX supporters), as well as many zarelabbers including, without trying to be exhaustive, Zee-Hwan Kim, Carl Matthews, Alex Kandel, Peter Rakitzis, Ian Konen, Andrew Alexander, Jing-Ran Chen, Richard Green, J. C. Poutsma, Clyde Wilson ...

During my five years at the Zarelab I have had the opportunity of working and benefitting from the work of very talented people. With Kostantinos Kalogerakis and Stefano Falcinelli I learned the intricacies of crossed beam experiments and mass spectrometric detection. Thanks for being so patient with such an uninitiated yet stubborn individual. Before me, Neil E. Shafer-Ray, Hao Xu and Danny Hughes worked in the $H + H_2$ section. Without their work, this thesis would have probably taken twice as long to accomplish. Many, many thanks to my coworker Brian D. Bean. With Brian I have spent more than three years assembling and disassembling the experimental setup in order to get the sensitivities that would allow state-resolved angular distribution measurements. Without his discipline, the experimental setup would not be even close to what it presently is. Also thanks to James D. Ayers for not believing everything I tell him everytime he asks me something about the experiment. Both Brian and James have been kind enough to go through this manuscript and make very useful comments and suggestions. I hope you may find some use to its contents in the future.

The Zarelab critically depends on all those people who work behind the scene. Lots of thanks go to Hank, Liz, Maritza, Lisa, Nguyet, Crystal and Loretta for making our lives so easy that we do not have to worry about anything but science. Other people have also helped me stay focused on science by taking care of the technical aspects of the experiment, especially Larry Wolford and Manuel Gutierrez.

Last, but definitely not least, I would like to thank my advisor Dick Zare. Dick is an excellent advisor, gifted with a very sharp scientific mind as well as with a

continuous and indestructible enthusiasm for science. His deep respect for independent thought makes working with him a real pleasure. Moreover, I was originally attracted to Dick's lab by its multidisciplinary character. Surely, my expectations fell quite short in comparison to what really goes on in his laboratory! Thanks Dick.

# Contents

# List of Tables

# List of Figures

# Chapter 1

# Introduction

*We see in nature not words,*
*but rather only the first letters of words,*
*and if we then wish to read, we discover*
*that the new so-called words*
*are again merely first letters of others.*

*G. C. Lichtenberg*

## 1.1 The Study of Elementary Chemical Reactions

The field of chemical reaction dynamics is a relatively young one in comparison with other more traditional areas of chemistry and physics. As the name implies, the major concern lies in an attempt to answer the most basic questions about chemical reactivity at the microscopic level [1–5].

Today, the methods employed for such a purpose may be highly sophisticated but the problems we attempt to address have been with us from a much earlier time. Already in the 6th century A. D., the latin philosopher Simplicius wrote: *"The* *atoms move in the void and catching each other up jostle together, and some recoil in any direction that may chance, and others become entangled with one another in various degrees according to the symmetry of their shapes and sizes and positions and order, and they remain together and thus the coming into being of composite things is effected."* Anyone with a general notion of the history of science should be apalled by the clarity and vision of this early text, specially if we remember that not until the turn of this century scientists universally accepted the foundations of the molecular theory of matter.

What has kept humankind from believing Simplicius statements at an earlier time? In the answer to this question lies the triumph of modern science, that is, the realization that a hypothesis has limited value until it is empirically corroborated. In this particular case, it has taken over a millenium to reach the point we have the tools to study and understand the microscopic underpinnings of chemistry and, therefore, make definite statements about what is happenning at the molecular level as we proceed from reagents to products.

In the early days, chemists could only take a glance at these details via the measurement of bulk properties. In such a manner, the Swedish physical chemist Svante Arrhenius [6] found more than a century ago that reaction rates increase with temperature in an exponential fashion. From the physical interpretation of this phenomenon important concepts such as that of an activation energy for reaction emerged. There was, however, a complication to surmount: nature hides its secrets through extensive averaging over initial conditions. Consequently, bulk observations are not directly connectable with what we may postulate are the elementary steps that lead to such an effect. Often we hear the phrase "a reaction mechanism can never be proved but only refuted." In other words, whatever makes A go into B may not necessarily involve a single step and, consequently, measurements on either A or B are not sufficient to make definite and precise statements about what causes such a change. There was, therefore, a need to find ways of looking at those "elementary steps" and try to fix and limit the initial conditions as much as possible so that a "clean" comparison with our theoretical expectations could be realized. For the chemical dynamicist, this wish has become possible in the last thirty to forty years with the advent of atomic and molecular beam methods in combination with molecular spectroscopy [7]. By careful control of the experimental conditions, the measurement of reaction cross sections, angular distributions, etc as a function of collision energy or reagent internal energy has become almost routine in the laboratory. Parallel to this experimental progress, quantum mechanics has provided a solid theoretical foundation to explain the details of bonding, structure, and ultimately chemical reactivity. The advent of powerful computer power has made it possible to carry out detailed calculations to be contrasted against experiment.

Experimentally, two different approaches are used for the study of reactive collisions [8]. Since the timescale for the breaking and forming of chemical bonds is in the femtosecond range, ultrafast techniques offer the possibility of "watching" molecules break apart and come together in real time [9, 10]. These techniques have recently been capable of observing directly the for-so-long-sought transition state in a chemical reaction [11–14]. These techniques, however, are rather recent and their range of applicability has been limited mainly because of the technical difficulties associated with the generalization of ultrafast techniques to any type of reactive process. Another approach, which is adopted in this work, is to carefully prepare the reagents, wait for reaction to take place, and then observe the outcome of single-collision events. We refer to these measurements as "asymptotic." By looking at the properties of the reaction product in this asymptotic limit we can attempt to learn about what happened during the course of the collision. This approach could be likened to that of a person who is given the task of finding out how a car accident occurred by carefully inspecting the skidmarks on the pavement as well as the damage in each vehicle.

The first generation of experiments using this asymptotic approach dates back to the decade of the sixties, the so-called "alkali-age." Rearrangement reactions involving alkali metals have unusually large cross sections. Mechanistically, this is believed to be the case because reaction occurs via an initial charge-transfer mechanism between the alkali metal and the other reagent at large impact parameters. The strong coulombic attraction between the ion pair makes the reaction probability to be close to unity once this electron transfer occurs, the so-called "harpoon" model [15]. Moreover, the low ionization potentials of the reaction products, generally alkali salts, greatly facilitates their detection using surface ionization detectors. During the seventies the pioneering work of the group led by Y. T. Lee made it possible to extend experimental work into a more general arena with the "universal molecular scattering chamber" [16]. The detection method of choice for these experiments became mass spectrometry with electron impact ionization. Despite its universal character, the unspecificity of the electron impact ionization method made internal energy resolution of the reaction products a very difficult task, only succesful in a few specific cases. Such is the case of F + $H_2$ reaction [17, 18]. At the same time, Zare and co-workers [19] introduced the use of laser-induced fluorescence to probe the internal energy distribution of the reaction product. The use of laser-based methods not only for product detection but also for reagent preparation [20] as an alternative to "brute-force" methods [21] has been quickly adopted by the chemical dynamics community [22–24].

## 1.2 The H + $H_2$ Reaction

### 1.2.1 Brief History

The history of the H + $H_2$ reaction and its isotopic counterparts follows very closely the developments in our current understanding of chemical reactivity. In the same way physics relies on the successes of quantum mechanics to describe the hydrogen atom, chemical reaction dynamics looks at three hydrogen atoms in an attempt to describe the most elementary step involving the breaking and forming of a chemical bond.

By 1926, Schrödinger, Heisenberg and others laid out the foundations of the new theory of wave mechanics [25, 26]. Shortly after, in 1929, London [27] proposed without a rigorous justification an expression of the potential energy for the interaction of three hydrogen atoms as a function of their relative positions. The work of London was followed by Eyring and Polanyi [28] shortly after and it laid out the foundations of the field of chemical reaction dynamics. It was realized that the outcome of a chemical reaction was dependent on the topology of the potential energy surface for reaction. All observables such as reaction cross sections, temperature-dependent rate coefficients, etc were reduced to the proper averaging of single-collision events taking place between particles on such a surface. The first classical trajectory study of the dynamics of a chemical reaction was carried out in 1936 for the hydrogen exchange reaction on the London potential energy surface by Hirschfelder, Eyring and Topley [29]. J. O. Hirschfelder evokes these early days before the availability of digital computers with the following words: *"when I was a graduate student, Eyring's office was filled with both cardboard and plaster of paris potential energy surfaces to simulate head-on collisions of atoms with diatomic molecules; and one of our functions was to roll the marbles!"* [30]. Despite the crudeness of these early methods, much of this work remains as a landmark in the field. A modified version of the London, Eyring, Polanyi (LEP) potential energy surface by Sato [31] in 1955, henceforth called LEPS parameterization, has been extensively used by several generations of chemical dynamicists. On such LEPS surfaces, Polanyi and co-workers [32–35] have carried a large body of classical trajectory calculations in their attempt to correlate dynamical behaviour with the details of the potential energy surface (location of energy barrier, attractive or repulsive character, etc). This work has led to the "Polanyi rules" [36] and to concepts as familiar today as "early" and "late" reaction barriers and their relation to the specific details of product internal energy distributions.

The history of $H_3$ kinetics prior to 1976 has been beautifully reviewed by Truhlar and Wyatt [37]. Until this time, most experiments had focused primarily on rate constant measurements under thermal as well as hot-atom conditions. Crossed-beam experiments had been attempted by Datz and Taylor [38] as early as 1963 and by Geddes, Krause and Fite in 1972 [39] but it became clear that new refinements in the experimental technique were necessary for a more systematic study of this reaction system. In the words of F. Kaufman [40]: *"Of all the elementary chemical processes, the $H + H_2$ reaction and its isotopic equivalents continue to be the critical test of theory and experiment ... I would stress that the reaction well deserves the wide attention which is receiving, that more kinetic data would be welcome, especially at the low temperature range, that crossed molecular beams would be particularly valuable*

*..., that rigurous computer calculations are still needed for comparison with quasi-equilibrium theories, but the calculations of transition state theory including tunneling corrections are based on too many questionable assumptions to represent a fruitful approach."*

The decade of the 1980's marked the beginning of a much richer period of experiments with the first state-to-state cross section measurements by the groups of Zare [41] and Valentini [42], and partially product-state-resolved crossed beam experiments by the groups of Kwei [43], Toennies [44], Gentry [45] and Lee [46]. The relatively large body of experimental data has been reviewed by several authors up to the year 1990 [47, 48] and will be described in more detail in chapters 7 and 8 in connection with our integral and differential cross section measurements.

Aside from scattering experiments, several groups have studied the spectroscopy of the excited states of the $H_3$ molecule after its first identification by Herzberg in 1979 [49]. Collings et al. [50] have reported the observation of the $HD_2^{\ddagger}$ transition state from the H+ $D_2$ reaction using resonance enhanced multiphoton ionization detection. These measurements, however, have not been duplicated by any other group to date. Figger and co-workers [51–53] have conducted an extensive investigation of the continuous UV and visible electronic spectra of $H_3$, $D_3$, $D_2H$ and $H_2D$. This experimental data allows for the determination of the lifetimes for the lower and upper adiabatic surfaces by the analysis of spectral widths. Comparison with two- and three-dimensional ab initio calculations of Mahapatra and Köppel [54, 55] show a reasonable degree of agreement between the two. The fragmentation dynamics of the low Rydberg states of $H_3$ into $H + H_2(v', J')$ or $H + H + H$ using laser excitation has been studied by Cosby, Helm and Müller [56–58] using double-coincidence techniques. Most recently, Müller and co-workers [59] have reported the first triple-coincidence experiment for the three-body breakup of $H_3$ in the 3s $^2A_1'$ and 3d $^2E''$ states.

Progress in the theoretical front has been reviewed by Truhlar and Wyatt [60] prior to 1977, just before the publication of the Liu-Siegbahn-Truhlar-Horowitz [61, 62] (LSTH) potential energy surface, the first ab initio surface with "chemical accuracy" (i.e., a fraction of a kcal/mol). The availability of increased computational power also allowed the first fully converged, quantum mechanical, three-dimensional calculations at low collision energies by Schatz and Kuppermann [63] in 1976. These early "exact" calculations on the hydrogen system motivated both the development of increasingly accurate potential energy surfaces as well as the improvement of the computational algorithms necessary to solve the Schrödinger equation more efficiently. These efforts have led to the double-many-body-expansion (DMBE) surface of Varandas, Brown, Mead and Truhlar [64], the BKMP [65] and BKMP2 [66] by Boothroyd, Keogh, Martin and Peterson and the Exact Quantum Monte Carlo (EQMC) surface of Wu, Kuppermann, and Anderson [67]. The calculation of the EQMC surface is based on the Quantum Monte Carlo method which has already provided the most accurate value for the barrier height of this reaction ($9.61 \pm 0.01$ kcal/mol) [68]. As such, it is expected to be the most accurate. A total of 76,000 nuclear geometries have been calculated via ab initio methods and the absolute value of the maximum error is 0.018 kcal/mol, in contrast with the more modest error of 0.55 kcal/mol obtained with the 267 ab initio points of the original LSTH potential energy surface.

### 1.2.2 Quantum Effects

Interest in this reaction system is not only dictated by the simplicity of its constituents and the possibility to carry out exact quantum mechanical scattering calculations. Also, the possibity for the manifestation of quantum mechanical effects in reactive scattering has drawn a great deal of attention on this system for decades [69]. For example, it was early realized via rate measurements that the Arrhenius plot displayed some curvature in the low-temperature region [70, 71], providing a model for theories of quantum-mechanical tunneling in chemical reactions.

The possibility for resonance behavior in this reaction system has also been a matter of considerable interest and controversy. In 1971 Levine and Wu [72] observed the presence of resonance scattering in their exact treatment of collinear H + $H_2$ reactive collisions. This behavior corresponded to "snarled" trajectories at the resonance energies as it would be expected from the stardard semiclassical interpretation of this phenomenon [73–75]. Almost twenty years after these first indications, measurements of state-to-state integral cross sections as a function of collision energy by the group of

Valentini [76, 77] seemed to show structure attributable to the sampling of the internal degrees of freedom of the $H_3$ transition state. This resonance behavior was later shown to be an experimental artifact by the experiments of Zare and co-workers [78] and the theoretical calculations of Miller and Zhang [79].

A more subtle quantum mechanical effect in this reaction system is related to the influence of excited potential energy surfaces on the outcome of a chemical reaction. At first thought, this effect may be thought to be small for collision energies below 2.7 eV, energy which corresponds to the minimum of the lowest excited adiabatic potential energy surface. This assertion turns out to be inaccurate in the case of the hydrogen exchange reaction. For geometries approaching $D_{3h}$ symmetry, Jahn-Teller mixing between surfaces leads the presence of a conical intersection in the topology of the two degenerate electronic surfaces. The consequences of this effect on the structure and nature of molecular energy levels had already been anticipated by Longuett-Higgins [80] as early as 1961. It was not until 1979 that Mead and Truhlar [81, 82] applied a similar reasoning in the context of reactive scattering to predict interference effects in the scattering amplitudes for reactions exhibiting conical intersections. In their formulation of the problem, the effect of the upper potential surface is incorporated by the introduction of a vector field and thus it has been given the name of the molecular Bohm-Aharonov [83] or the Geometric Phase effect [84]. As the latter name implies, interference between indistinguishable paths is accounted for by the introduction of a phase factor multiplying each scattering amplitude which ultimately leads to quantum mechanical interference. Unlike the resonance behavior described previously, this phenomenon is purely quantum mechanical in nature and, therefore, lacks a classical analogue. The implications of the Geometric Phase effect for the hydrogen exchange reaction and its isotopic counterparts have been explored theoretically by Kuppermann and co-workers [85, 86]. From these calculations, it was found that the introduction of this effect had quite visible signatures specially in state-resolved differential cross sections over a wide range of collision energies as much as 1.5 eV below the intersection with the upper potential energy surface. Experimentally, however, there has not been conclusive evidence supporting this theoretical work. The major reason between this apparent disagreement between theory and experiment resides in the lack of state-resolved data beyond integral cross section measurements.

## 1.3 Motivation and Outline

Section 1.2 presented a brief overview of the long and interesting history behind the $H + H_2$ reaction system. Despite over sixty years of continuous experimental and theoretical efforts, much remains to be done to reach a complete understanding of the dynamics underlying this seemingly simple chemical reaction. The work presented in the next chapters is part of our current efforts to carry out detailed experimental studies on the hydrogen exchange reaction. As such it has been organized in a way similar to the recent progress in the $H + H_2$ section of the Zarelab in the study of this fundamental chemical reaction.

We begin in Chapter 2 with a description of the photoloc technique and its specific application to this reaction system. Special attention is given in Section 2.3 to the different experimental approaches that have been used till present for the measurement of speed distributions from elementary processes such as photodissociation or chemical reactions.

In Chapter 3 we describe the current experimental apparatus. Although its contents are purely descriptive, they also begin to demonstrate the required level of sophistication needed to carry out detailed scattering measurements in the hydrogen-atom, hydrogen-molecule reactive system.

This chapter is followed by a discussion of the spectroscopy of the $H_2$ molecule and its isotopomers in Chapter 4. There, we focus on the description on the various spectroscopic techniques used to detect the hydrogen molecule. We will show how resonance-enhanced multiphoton ionization (REMPI) methods offer a means of detecting the minute amounts of reaction product into single rovibrational levels of the diatomic product. Even though there exists a well-studied (2+1) REMPI scheme for hydrogen molecule detection, investigation of alternative spectroscopic transitions is an area of great interest to us, specially in regard to the measurement of the rotational polarization of the diatomic product. Such a measurement will mark the beginning of a new generation of experiments beyond what is nowadays possible.

Chapter 5 presents a detailed account of the calibration procedures we have used to characterize the time-of-flight instrument using single-speed velocity distributions arising from either one-photon photodissociation or chemical reaction. It is not easy to emphasize enough the importance of these measurements for a reliable interpretation of velocity distributions from chemical reactions. Similarly, in Chapter 6 we explain in detail the results of our studies to characterize the reaction conditions so as to provide as much information as possible for a close comparison with theoretical predictions.

Chapters 7 and 8 present integral and differential cross section data obtained for the hydrogen exchange reaction using the methods and procedures previously described. Special attention is given to the details of the experimental protocol followed for each type of measurement.

Chapter 9 attempts to combine our current knowledge of the dynamics governing the hydrogen exchange reaction with the trends found in the experimental data of Chapters 7 and 8. We find that our experimental findings are consistent with a simple model that emphasizes the importance of entrance-channel dynamics in this reactive system.

This thesis is based on both unpublished and published work performed in our laboratory in the last four years. Much of the contents of Chapters 2, 4, 5, and 6 have been adapted from F. Fernández-Alonso, B. D. Bean, and R. N. Zare, "Measurement of the $\mathrm{HD(v'=2, J'=3)}$ product differential cross section for the $\mathrm{H + D_2}$ reaction at $1.55 \pm 0.05$ eV using the photoloc technique," J. Chem. Phys. 111, 1022 (1999). The experimental results from Chapter 7 are part of a manuscript by B. D. Bean, F. Fernández-Alonso, and R. N. Zare in preparation for submission to the Journal of Chemical Physics. Similarly, Chapters 8, and 9 have been taken from F. Fernández-Alonso, B. D. Bean, and R. N. Zare, "Differential cross section for $\mathrm{H + D_2} \rightarrow \mathrm{HD(v'=1, J'=1,5,8) + D}$ at 1.7 eV," J. Chem. Phys. 111, 1035 (1999), and from F. Fernández-Alonso, B. D. Bean, and R. N. Zare, "Differential cross section for $\mathrm{H + D_2} \rightarrow \mathrm{HD(v'=2, J'=0,3,5) + D}$ reaction at 1.55 eV" J. Chem. Phys. 111, 2490 (1999).

# Chapter 2

# The Photoloc Technique

*Men love jargon. It is so palpable, tangible, visible, audible; it makes so obvious what one has learned; it satisfies the craving for results. It is impressive for the uninitiated. It makes one feel one belongs. Jargon divides Men into Us and Them.*

*M. Buber, "I and Thou"*

## 2.1 Principles of the Technique

Photoloc is an acronym for "*photo*initiated reaction analyzed via the *l*aw *o*f *c*osines." This name stems from the two major elements of the technique: first, laser photolysis initiates the chemical reaction in a mixture of a photolytic precursor and reagent; and second, the law of cosines relates the product laboratory velocity distribution to the center-of-mass angular distribution, i.e., the product differential cross section. In this section we describe the principles of this technique. In the next section, we will illustrate the power of the technique with specific examples relevant to the hydrogen exchange reaction and its isotopic counterparts. The structure of this exposition follows closely that of Shafer-Ray and co-workers [87–89]. The reader should consult these references for further details about the expressions presented here.

The two steps in the photoloc sequence are shown below

$$AX \xrightarrow{h\nu} A + X \tag{2.1}$$

$$A + BC \longrightarrow AB + C \tag{2.2}$$

Initially, a polarized laser beam photolyzes the AX precursor, generating A fragments with a well-defined laboratory speed and spatial anisotropy which subsequently collide with the BC reagent to generate AB and C products. A second laser beam probes the $\mathrm{AB(v', J')}$ or C products.

In the limit of zero relative speed between AX and BC, which is achievable by coexpanding them into a vacuum, the center-of-mass speed is solely dictated by the photolysis wavelength and the nature of the photolytic precursor AX. The translational energy of photofragment A is given below

$$E_A = \left(\frac{m_A}{m_{AX}}\right) \cdot (h\nu - \Delta E_A) \tag{2.3}$$

where the m's are the masses of A and AX, $h\nu$ is the photon energy and $\Delta E_A$ is the endoergicity of the photolysis process. From Eq. (2.3), and the fact that AX and BC are stationary with respect to each other, the center-of-mass speed is fixed at a value

$$u_{CM} = \left(\frac{m_A}{M}\right) \cdot \sqrt{\left(\frac{2E_A}{m_A}\right)} \tag{2.4}$$

where $M = m_A + m_{BC}$, and $E_A$ has been calculated from Eq. (2.3). For a specific $\mathrm{AB(v', J')}$ product state of known endoergicity $\Delta E$, conservation of energy and linear momentum in the center-of-mass frame yield the following expression for the magnitude of the center-of-mass speed of the $\mathrm{AB(v', J')}$ product

$$u_{AB} = \left(\frac{m_C}{M}\right) \cdot \sqrt{2\left[\frac{\left(\frac{\mu}{m_A}\right) E_A - \Delta E}{\mu'}\right]} \tag{2.5}$$

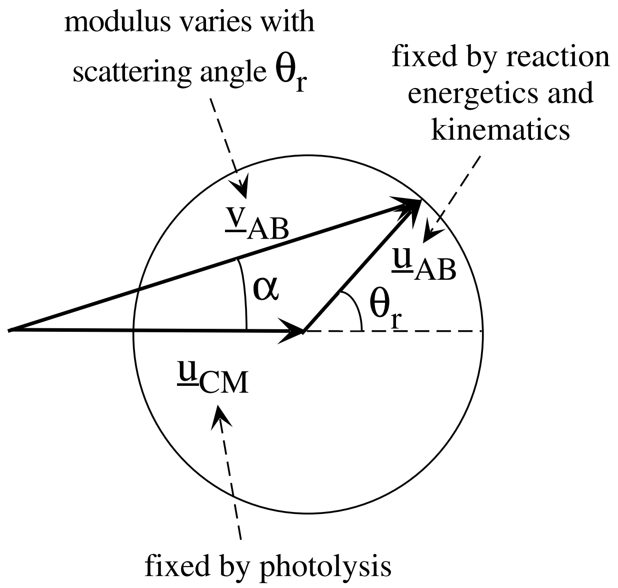


Figure 2.1: Collapsed Newton diagram pertinent to the photoloc technique. For detection of a particular AB(v′, J′) state, the only vector in this figure with a variable modulus is the laboratory product speed. This change in modulus can be mapped directly into a change in center-of-mass scattering angle.

where $\mu$ and $\mu'$ are the reduced masses of the reagent and product collision partners respectively. Finally, the product velocity $\underline{\vec{v}}_{AB}$ is the vector sum of $\underline{\vec{u}}_{CM}$ and $\underline{\vec{u}}_{AB}$, whose moduli have been given by Eqs. (2.4) and (2.5) respectively, namely

$$v_{AB}^2 = u_{CM}^2 + u_{AB}^2 + 2u_{CM}u_{AB}\cos\theta_r \tag{2.6}$$

where $\theta_r$ is the center-of-mass scattering angle. An excellent way to picture the above quantites given by Eqs. (2.1)-(2.6) is to use a "collapsed" Newton diagram as shown in Fig. 2.1 The straightforward trigonometric relationship between $\underline{\vec{v}}_{AB}$, $\underline{\vec{u}}_{CM}$, and $\underline{\vec{u}}_{AB}$ is very clear and it immediately implies that a measurement of the product laboratory distribution can be related to the center-of-mass scattering angular distribution, i.e., the product differential cross section.

In what follows, we outline the steps of the derivation of the three-dimensional laboratory velocity distribution for the case of a one-photon photolysis with linearly polarized radiation. Further details may be obtained from Shafer et al. [88]. The extension of this treatment to more complex photolysis processes, i.e., circularly polarized light or multiphoton photodissociation, is very similar to the one given here but complicates the algebra of the derivation.

For the case of a single photolysis channel with anisotropy $\beta_{phot}$, photodissociation with linearly polarized light yields a spatial distribution of photogragment A laboratory speeds of the form

$$f\left(\underline{\vec{u}}_A\right) = \frac{1 + \beta_{phot} \cdot P_2\left(\underline{\vec{u}}_A \cdot \underline{\vec{\epsilon}}_{phot}\right)}{4\pi} \tag{2.7}$$

where $\underline{\vec{u}}_A$ and $\underline{\vec{\epsilon}}_{phot}$ are unit vectors corresponding to the photofragment velocity and photolysis laser polarization vectors, and $P_2(x) = \frac{1}{2}\left(3x^2 - 1\right)$ is the second Legendre polynomial. The argument in $P_2(x)$ is simply the cosine of the angle between the velocity vector of the photofragment and the direction of the laser polarization. This expression leads to the familiar perpendicular and parallel angular distributions typically found in photodissociation processes under the fast-recoil approximation [90, 91].

From the above considerations, it is not surprising to find that if Eq. (2.7) governs the photodissociation step, then the laboratory distribution of AB product velocities is given by an analogous expression, namely,

$$f\left(\underline{\vec{v}}_{AB}\right) = \left(\frac{1}{2v_{AB}u_{AB}u_{CM}}\right)\left(\frac{1}{\sigma}\frac{\partial\sigma}{\partial\Omega_r}\right)\left\{1 + \beta_{rxn}P_2\left(\underline{\vec{v}}_{AB} \cdot \underline{\vec{\epsilon}}_{phot}\right)\right\} \tag{2.8}$$

where $\frac{1}{\sigma}\frac{\partial\sigma}{\partial\Omega_r}$ is the normalized differential cross section into a particular solid angle $\Omega_r$ and $\beta_{rxn}$ is a velocity-dependent anisotropy parameter. This expression has been defined so that it is normalized to unity. The similarites between Eqs. (2.7) and (2.8) are striking in the sense that for a single laboratory product speed, the spatial distribution has the same functional form as that of a photodissociation experiment with an anisotropy given by $\beta_{rxn}(v_{AB})$. It follows that the total distributions of laboratory speeds is a weighted sum of photolysis-like spatial distributions, the weights being proportional to the differential cross section for reaction at a particular scattering angle. Referring to Fig. 2.1 , we find that the product anisotropy is related to the photolysis anisotropy by

$$\beta_{rxn}\left(\underline{\vec{v}}_{AB}\right) = \beta_{phot} P_2\left(\underline{\vec{v}}_{AB} \cdot \underline{\vec{u}}_{CM}\right) \tag{2.9}$$

where $\underline{\vec{v}}_{AB} \cdot \underline{\vec{u}}_{CM} = \cos\alpha$, and $\alpha$ is the angle between the center-of-mass velocity and the laboratory product velocity. This angle is fixed for a particular laboratory product speed by the expression

$$\underline{\vec{v}}_{AB} \cdot \underline{\vec{u}}_{CM} = \cos\alpha = \frac{v_{AB}^2 + u_{CM}^2 - u_{AB}^2}{2 v_{AB} u_{CM}} \tag{2.10}$$

From Fig. 2.1, we can see that $\underline{\vec{v}}_{AB}$ has a maximum and minimum value corresponding to the vector addition of the center-of-mass vectors $\underline{\vec{u}}_{AB}$ and $\underline{\vec{u}}_{CM}$ in a parallel and antiparallel fashion, i.e., forward and backward center-of-mass scattering. The range of laboratory speeds possible for a particular AB(v′, J′) state depends on the particular details of the kinematics and energetics of the reaction of interest. It is convenient to define the parameter $\gamma$ as the ratio of the center-of-mass product speed and the center-of-mass speed. This parameter is then given by

$$\gamma = \frac{u_{AB}}{u_{CM}} = \left(\frac{m_C}{m_A}\right) \cdot \sqrt{\frac{\mu E_A - m_A \Delta E}{\mu' E_A}} \tag{2.11}$$

Next, we consider the three limiting values of the value of $\gamma$ and what type of experimental information may be obtained in each case.

1. $u_{AB} << u_{CM}$ ($\gamma << 1$)

   If the product speed in the center-of-mass is much smaller than the center-of-mass speed, the laboratory product speed equals the center-of-mass speed which is dictated by the mass combination of the collision partners and the collision energy as shown explicitly by Eq. 2.4. In this case, no information about the center-of-mass angular distribution is experimentally accessible.

| Species | Fast Channel (eV) | Slow Channel (eV) |
|---|---|---|
| HI | 3.054 | 3.997 |
| HBr | 3.758 | 4.210 |
| $H_2S$ | 3.898 | |

Table 2.1: Dissociation energies in eV for the three most common H-atom photolytic precursors.

2. $u_{AB} >> u_{CM}$ ($\gamma >> 1$)

   If the center-of-mass speed is negligible compared to the center-of-mass speed of the product, the laboratory speed is also fixed at a single value, namely, $\underline{\vec{v}}_{AB} = \underline{\vec{u}}_{AB}$. In this case, however, measurement of the spatial anisotropy, $\beta_{rxn}$, of the product velocity distribution gives the second moment of the angular distribution, i.e., the average value of the second Legendre polynomial.

3. $u_{AB} = u_{CM}$ ($\gamma = 1$)

   This is the optimal case since we now have a maximal range of laboratory speeds, i.e., from zero to $2u_{AB}$. Measurement of the laboratory product speed distribution allows a direct measurement of the product differential cross section.

## 2.2 Application to the H + $D_2$ Reaction

It is instructive to use the formalism introduced above to the chemical reaction pertinent to this work to help us understand what are the major prerequisites for the state-resolved measurements we intend to carry out.

Suitable photolytic precursors to generate hot hydrogen atoms include the HI, HBr, and $H_2S$ molecules. Other potential candidates that have or may be used as hot H-atom sources are compiled in the monographs by Robin [92] and Sato [93]. We list

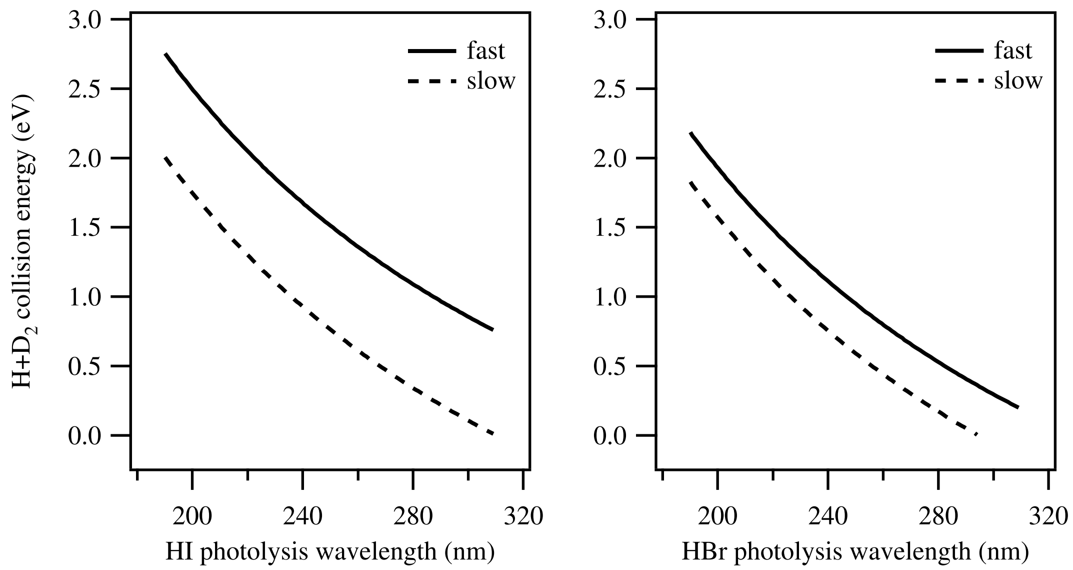


Figure 2.2: Center-of-mass collision energies from the photolysis of HI (left) and HBr (right) as a function of photolysis wavelength.

in Table 2.1 the best values for the bond energies for these three photolytic precursors. At typical photolysis wavelengths, generally between 190 and 310 nm, HI and HBr photodissociate into ground-state and excited-state I and Br atoms respectively. Dissociation energies for the halogen halides HI and HBr have been obtained from Huber and Herzberg [94]. The value for the H-HS bond energy shown in the third row has been taken from Wilson et al. [95]. The case of $H_2S$ is more complicated since many $HS(v', J')$ states are energetically acessible and the subsequent H-atom velocity distribution is no longer unique. Photodissociation experiments by Ashfold and co-workers [95–97] on this molecule show, however, that the H-atom velocity distribution is usually peaked close to the maximally allowed value at the wavelengths of interest, i.e., HS molecules are rotationally and vibrationally cold. The same experiments show, however, a noticeable change in the shape of the velocity distribution of the H photofragments over wavelength. Even though this molecule can be used to initiate the chemical reaction in experiments that do not require a well-defined collision energy and photofragment spatial anisotropy, the experiments presented in this thesis will be restricted to the use of HI and mostly HBr as photolytic precursors.

Fig. 2.2 shows the collision energy versus photolysis wavelength for the HBr and HI photolytic precursors. It is important to note the ample range of collision energies at our disposal, in principle ranging from 0.0 eV to 3.00 eV. For our particular reaction system, this collision energy window ranges from the energetic threshold for reaction ($\sim$ 0.40 eV) to energies above the intersection with the first excited adiabatic surface. Collision energy energy tunability is possible by either tuning the photolysis wavelength or by changing the photolytic precursor. The major drawback from using these photolytic sources is the presence of more than one photodissociation channel over most of the wavelength range. This problem can be circumvented by spatially separating the HX and $D_2$ sources as it has been implemented by Schnieder et al. [98]. The fact that the two possible photolysis channels have almost opposite spatial anisotropies makes it possible to direct either H-atom population toward the other reactant beam by changing the polarization of the photolysis beam. This approach, though more elegant, adds an extra degree of difficulty to the measurements, making the detection of the diatomic product in a quantum-specific fashion practically impossible. Measurements carried out in the same molecular beam are restricted to those cases that have a negligible contribution from one of the photolysis channels. This occurs, for example, when the photolysis energy is sufficiently low that only ground state halogen atoms can be produced, i.e. at the longest photolysis wavelengths. Additionally, it is often the case that the nature of the photodissociation step is such that it favors the production of one channel over the other by factors as high as five or ten. Such is the case of the production of fast H atoms from HBr photolysis between 200 and 250 nm. At these wavelengths there is seven to eight times more fast hydrogen atoms than slow ones. Finally, we can take advantage of the difference in collision energies for both velocity groups and target those $HD(v', J')$ levels that can only be accessed at the higher collision energy. For these states, the presence of the additional velocity group is inconsequential. In summary, even though the carrying out of experiments in a single molecular beam using HI or HBr as photolytic precursors has its disadvantages and cannot be made general, it is still possible to carry out clean state-resolved measurements for a relatively large number of internal energy states and collision energies.

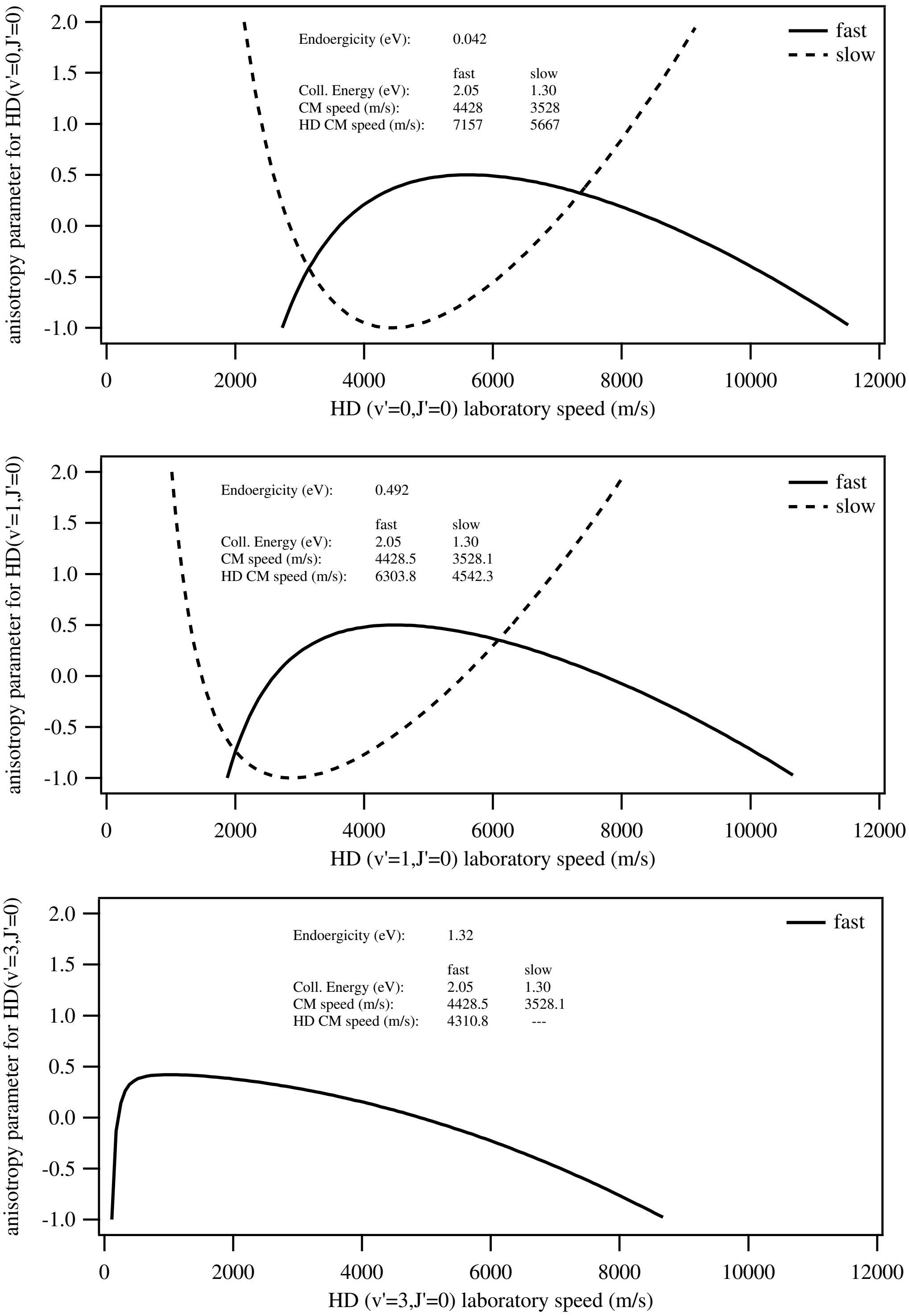


Figure 2.3: Angular anisotropy vs product speed for HD in selected internal energy states originating from the photolysis of HI at 220 nm.

Another concern pertains the range of speeds attained by the HD product since under some unfavorable kinematic and energetic situations it is not possible to obtain angular information from the laboratory velocity distributions. To assess quantitatively this complication we introduced in the previous section the $\gamma$ parameter (see Eq. (2.11)). This parameter is both dependent on the mass combination, collision energy and reaction endoergicity, i.e, the rovibrational state of the detected $\mathrm{HD(v', J')}$ product. As a first approximation, we take the engoercity to be zero, yielding a value of $\gamma \approx 1.6$. This value is very close to the ideal case of unity, which occurs when the product and center-of-mass speeds are equal and the range of product laboratory speeds is maximal. Fig. 2.3 shows the reaction product anisotropy as given by Eq. (2.9) vs product speed for increasingly higher $\mathrm{HD(v', J')}$ product states using HI photolysis at 220 nm. The anisotropies of the fast and slow channels are $\beta = -1$ and $\beta = +2$ respectively. Despite the obvious decrease of the range of product speeds with increasing product internal energy, there is still an easily detectable change in product laboratory speeds corresponding to forward and backward scattering. For the particular case of $\mathrm{HD(v' = 3, J' = 0)}$, shown at the bottom of the figure, only the fast photolysis channel at a collision energy of 2.05 eV can access this state, but the range of speeds is still more than 8000 m/s, comparable to the other less endoergic channels shown in the same figure. As the figure also shows, to each laboratory speed there corresponds a specific value of the spatial anisotropy. The very different behaviour of the spatial anisotropy for each photolysis channel can be advantageous to avoid even further the contribution of the undesired photolysis channel to the detected signal if it is possible to find a means of discriminating against particular velocity groups to further reduce the contribution of the unwanted photodissociation channel.

## 2.3 The Measurement of Velocity Distributions

In Section 2.1 we showed how the measurement of a laboratory speed distribution can be related to the center-of-mass differential cross section. We have not mentioned, however, how this distribution can be measured. To date, several methods have been proposed and used to achieve this goal. All of them share in common the same unifying feature, namely, the measurement of the laboratory speed distribution along a given laboratory axis and the subsequent inversion of the experimental data to obtain the three-dimensional velocity distribution. The details of how such an inversion is performed is specific to the particular technique in use. In general, a sound experimental technique ought to allow for a straightforward and reliable inversion method.

Fig. 2.4 illustrates the relationship between a given three-dimensional single-speed distribution with a known spatial anisotropy and the corresponding projection of this distribution onto a given laboratory axis, what we call the detection axis. This projection is not only sensitive to the magnitude of the speed which is given by the maximum shift from the center of the distribution. Its shape is also related to the anisotropy of the velocity distribution in three-dimensional space. Therefore, by analyzing both the width and the shape of a projection onto a one-dimensional axis it is possible to learn about the full three-dimensional spatial distribution of laboratory speeds.

We have chosen to subdivide the realm of "velocity-sensitive" techniques into two domains that we will call "Dopplerimetry" and "TOF-based methods," which we now turn to describe in more detail.

### 2.3.1 Dopplerimetry

Everyone is familiar with the Doppler effect in atomic and molecular spectroscopy. The velocity of the probed species relative to the direction of propagation of light translates into a shift in the frequency of absorption [99]. This shift results in what is commonly called the inhomogeneous broadening of spectral lineshapes. In the case of a randomly oriented molecular sample at a well-defined temperature (i.e., the distribution of speeds obeys a Maxwell-Boltzmann distribution), this distribution is gaussian. If we account for other lineshape broadening effects such as for example excited-state lifetime, then a frequency scan over the lineshape can be directly related to the projection of the velocity distribution along the laser propagation axis, i.e., the frequency shift being proportional to the velocity of the molecule along the light

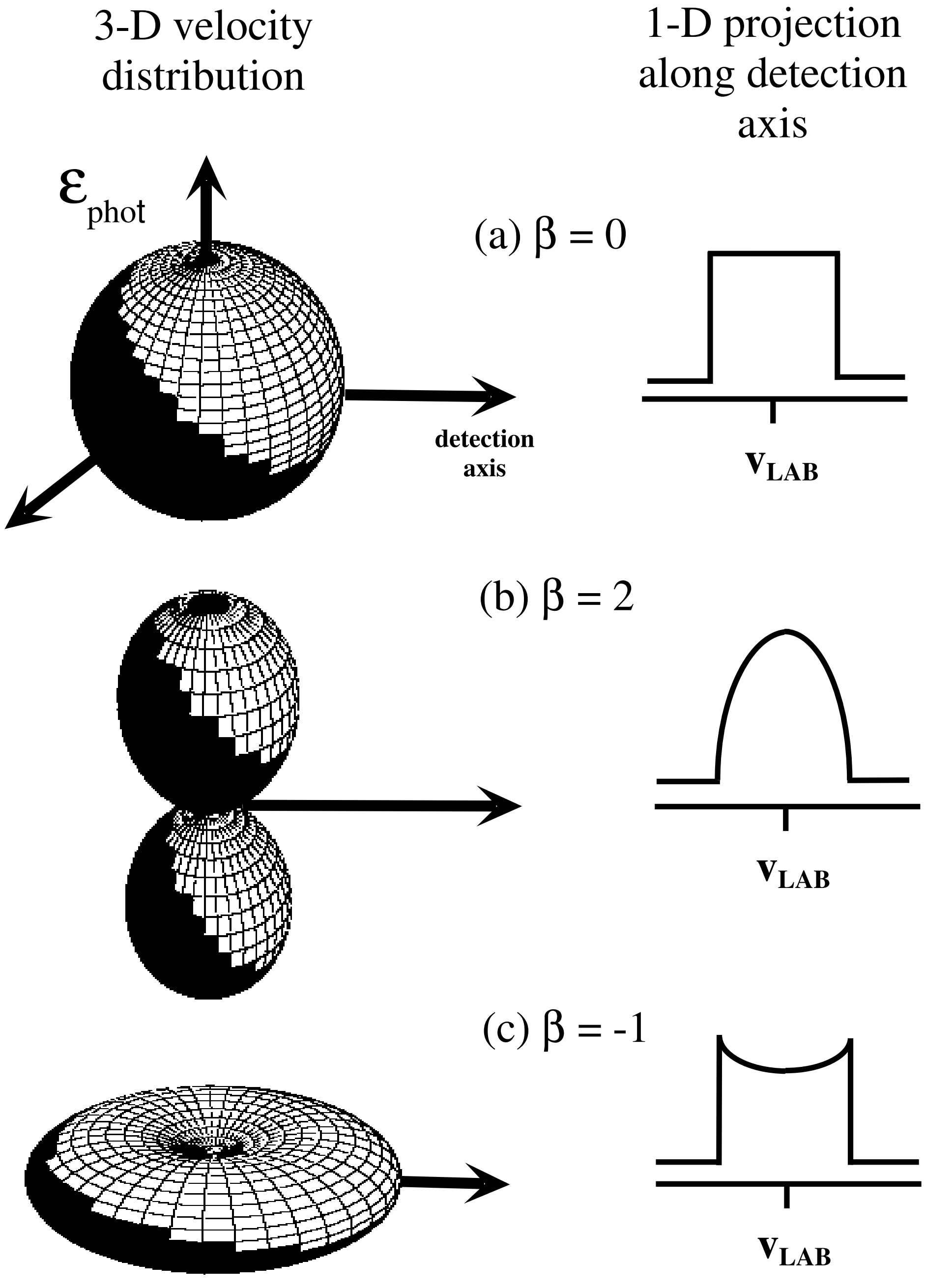


Figure 2.4: Three dimensional velocity distributions and corresponding one-dimensional projections onto a plane perpendicular to the detection axis.

propagation axis. In other words, since we know the relationship between velocity and frequency shift it is possible to find a mapping between these two variables if proper account is taken of other broadening effects.

The availability of well-collimated light sources such as the laser have made these measurements routine in the laboratory and today there is an extensive amount of work that uses Doppler spectroscopy for the study of inelastic and reactive collisions. McCaffery and coworkers [100–103] have used velocity-selected double resonance (VSDR) techniques to study inelastic state-to-state differential cross sections in rare gas-diatom collisions. Vigué and coworkers [104, 105] have been capable of carrying out state-selected measurements for the $F + I_2$ reaction in a crossed molecular beam experiment by the use of the ADDS (angular distributions using the Doppler shift) and PADDS (perpendicular ADDS) techniques first suggested by Kinsey [106–109]. Simons and co-workers have applied laser photolysis and Doppler spectroscopy to the study of the stereodynamics of various chemically relevant systems including $O(^1D) + N_2O$ [110, 111], $O(^1D) + CH_4$ [112, 113], $O(^1D) + H_2$ [114, 115], and $H + CO_2$ [116]. Hall and co-workers [117] have utilized Monte Carlo techniques to invert the OH Doppler profiles arising from the $H + O_2$ reaction to obtain center-of-mass angular distributions. The degree of resolution of these experiments is determined not only by the spread of speeds of the reaction product but also by the inherent resolution of the light source. Consequently, an increase in the angular resolution is accompanied by an increase in the degree of sophistication of the required laser technology. In general, studies have been restricted to either the very light atoms or molecules such as hydrogen, and/or to spectral regions easily accessible by high-resolution laser sources. Moreover, Doppler spectroscopy relies on the scanning over the line profile of the species of interest, the signal shape becoming susceptible to the laser power and other sources of signal fluctuations during the course of the experiment. While this may be tolerable in large-signal experiments, it may become prohibitely dangerous in beam experiments with low signal yields.

### 2.3.2 Velocity-Sensitive Time-of-Flight Spectrometry

Time-of-flight mass spectrometry (TOF-MS) has become a standard method for the mass analysis of chemical samples [118]. Electric fields (static or pulsed) are used to accelerate ions toward a detector, the flight time being proportional to the mass-to-charge ratio. Aside from this conventional use of the technique, TOF-MS can be made to be formally identical to Doppler spectroscopy by exploiting the relationship between the projection of the ion speed along the detection axis and the arrival time at the detector. The dependence of the arrival time on the initial speed is generally much smaller than the dependence on the mass-to-charge ratio and leads to a loss of mass resolution. Such an unwanted effect for most applications is useful for our purposes of doing velocity analysis of reaction products.

Since we want to study neutral-neutral reactions, it is necessary first that we generate ions that can then be mass and velocity-analyzed. This is accomplished by the use of resonance-enhanced multiphoton ionization (REMPI) techniques. A more complete discussion of this technique will be deferred to Chapter 4. For the purposes of the present discussion we take as a fact that it is possible, by the use of laser spectroscopy, to generate ions with the same velocity as the original neutral. This is true because of the disparity of masses between the ejected electron in the REMPI process and the remaining positive molecular ion.

Two methods have been implemented to realize velocity-sensitive TOF-MS in our laboratory. Shafer et al [119] have used 2D-REMPI-TOF and impulse-extraction TOF [120] to infer the three-dimensional distribution arising from photoinitiated reactions. Alternatively, Simpson et al. [121] have used the core-extraction technique in a Wiley-McLaren TOF spectrometer for the study of bimolecular reactions and photodissociation processes. We turn now to provide the reader with the operational principles of the latter technique since it will be used in the remainder of this work.

#### Wiley McLaren REMPI-TOF with Core Extraction

The simplest time-of-flight spectrometer consists of a repeller and an extractor plate held at a known potential difference. The constant electric field between these two

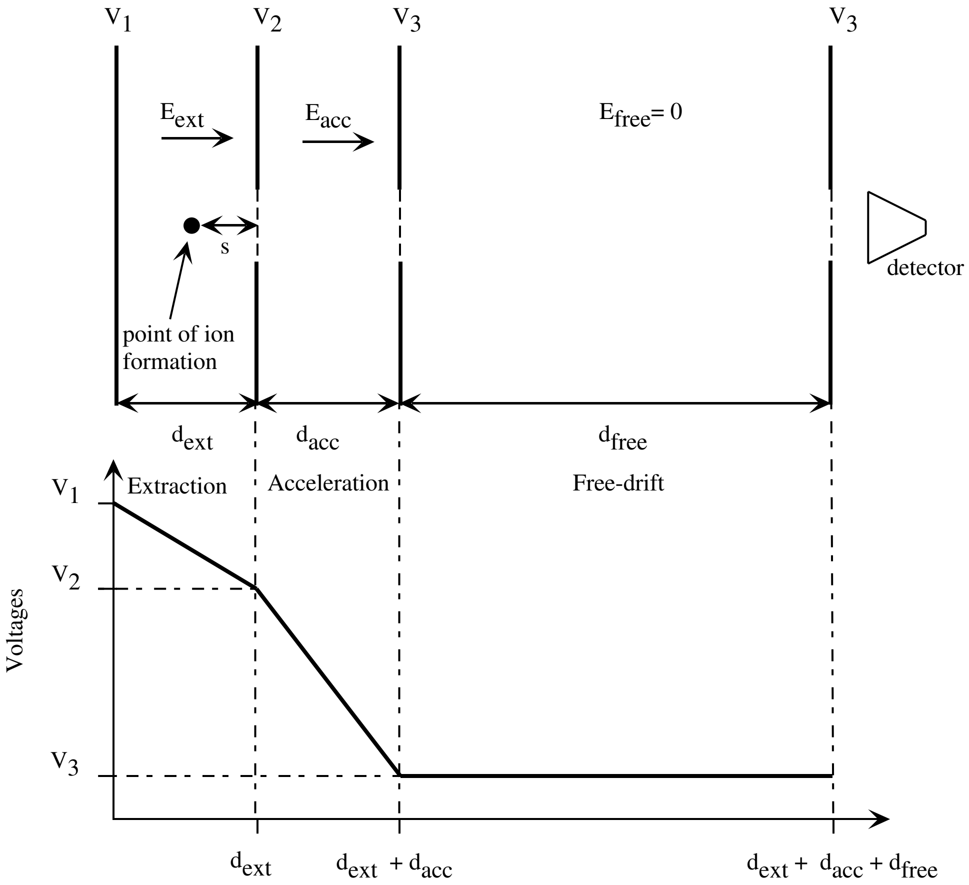


Figure 2.5: Schematic diagram of a Wiley-McLaren time-of-flight spectrometer.

plates determines the force exerted on the ions and, therefore, the arrival time at the detector. It was early realized by Wiley and McLaren [122] that such an arrangement had a major problem, namely, that the arrival time was quite dependent on the starting position of the ion. If the ion source is not capable of creating ions at the same place reproducibly, this effect necessarily translates into a degradation of mass resolution and a lack of reproducibility of the instrument. To solve this problem, they proposed a slightly more complicated arrangement. The spectrometer consists of the original extraction and field-free regions plus an acceleration region in between these two. By adjusting the fields in the extraction and acceleration regions it became possible to make the arrival time largely insensitive to the original point of ion formation.

Figure 2.5 shows a schematic diagram of a typical Wiley-McLaren time-of-flight spectrometer as well as a diagram of the voltages (fields) in each region of the instrument. The appropriate expressions for the flight times in each region can be readily calculated from simple kinematics and will not be reproduced here. The reader is referred to the original paper by Wiley and McLaren [122] for more details.

Insensitivity to the specific place of ion formation, also called "space focusing" is given from the condition

$$\left(\frac{\partial T}{\partial s}\right)_{s_0} = 0 \tag{2.12}$$

where T is the total flight time and $s_0$ is the point where the ions are created in the extraction region. This condition can be written in terms of the design parameters of the time-of-flight instrument in the form of an explicit equation as shown below

$$d_{free} = 2s_0 k_0^{\frac{3}{2}} \left(1 - \frac{1}{k_0 + k_0^{\frac{1}{2}}} \cdot \frac{d_{acc}}{s_0}\right) \tag{2.13}$$

where $k_0$ is the ratio of fields or voltages under which space focusing conditions hold and is explicitly given by

$$k_0 = \frac{(s_0 E_{ext} + d_{acc} E_{acc})}{s_0 E_{ext}} \tag{2.14}$$

The electric fields $E_{ext}$ and $E_{acc}$ are given by (refer to Figure 2.5)

$$E_{ext} = \frac{V_1 - V_2}{d_{ext}} \tag{2.15}$$

$$E_{acc} = \frac{V_2 - V_3}{d_{acc}} \tag{2.16}$$

More complicated experimental arrangements have been proposed in the literature [123, 124]. By including additional acceleration stages, deviations from the space focusing conditions can be corrected to higher order.

To investigate the effects of initial ion velocities we consider two ions formed at the same initial position s, with equal, but oppositely directed speeds. The ion moving

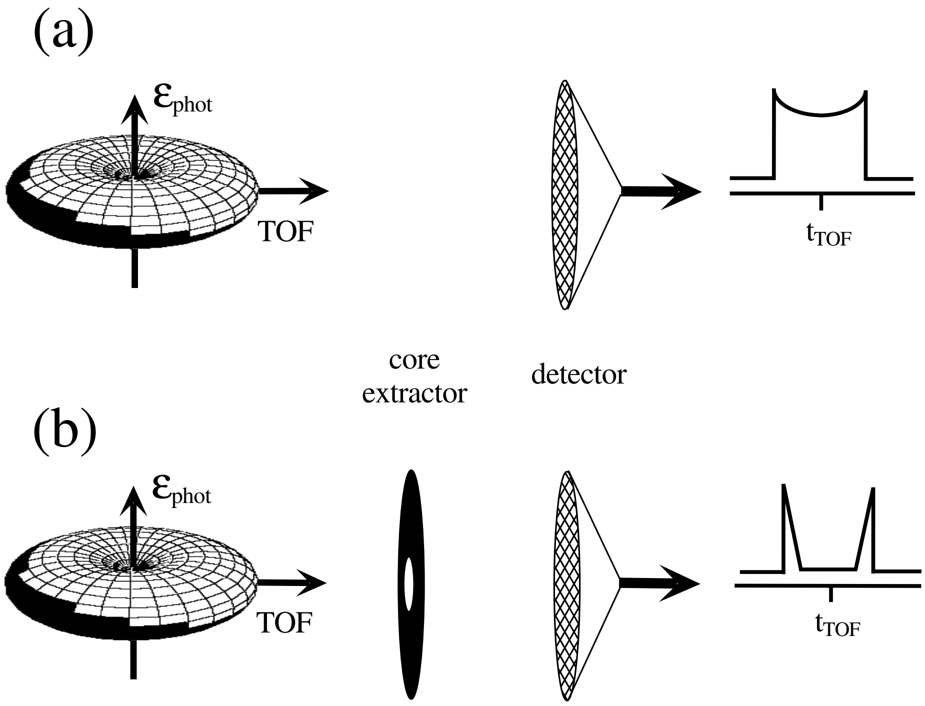


Figure 2.6: Cartoon showing the principle of core extraction for a single-speed population with anisotropy $\beta = -1$. (a) Shows the time-of-flight profile arising from the projection of such a three-dimensional distribution on a plane detector. (b) shows the effect of placing a conical mask that only allows detection of those ions with a maximal projection of the laboratory speed onto the time-of-flight axis.

away from the detector will decelerate until it stops and is then accelerated returning to the point of origin s with its original speed (but opposite direction). From then onwards, its motion is identical to that of an ion originally moving at the same speed toward the detector. The final flight time will then be increase by a "turn-around" time equal to

$$\Delta T = \frac{2v_{init}}{a_{ext}} \tag{2.17}$$

where $v_{init}$ is the initial speed of the ion along the time-of-flight axis (along the electric field lines) and $a_{ext}$ is the acceleration imparted to the ion of charge q and mass m by the extraction field, namely

$$a_{ext} = \frac{qE_{ext}}{m} \tag{2.18}$$

Up to this point, a time-of-flight profile is completely identical to a Doppler measurement since Eq. (2.18) allows us to relate a time-of-flight shift to an original speed in the same way a frequency shift in an optical spectrum is related to the same observable. We next implement core-extraction by placing a small hole in front of the detector, and detect only those ions with a maximal projection of their velocities on the detection axis, i.e, those ions that have not moved away from the detection axis during their flight time toward the detector. This process is shown in Fig. 2.6, which shows the effect of core extracting a single-speed ion sample of known spatial anisotropy. Core extraction amounts to throwing away all the signal from the original profile except the edges, thus providing a one-to-one mapping between the ion speed along the detection axis and the corresponding time-of-flight shift. This approach is particularly useful when there is an inherent continuous distribution of speeds in the ion of interest, as it is the case of the products from photoinitiated reactions. As shown in Section 2.1, in our case each laboratory speed can then be mapped onto a single center-of-mass scattering angle. This technique, therefore, allows a direct measurement of the angular distribution of reaction products. Moreover, without core extraction, each speed component would partially overlap with others and the signal would become congested to the point a reliable inversion of the data may become difficult in practical situations.

# Chapter 3

# Experimental Apparatus

*Experiments are the only means of knowledge at our disposal. The rest is poetry, imagination.*

*M. Plank*

Figure 3.1 shows a schematic diagram of the experimental apparatus employed in the studies described in this work. The setup can be subdivided into four parts: vacuum chamber and reagents, time-of-flight spectrometer, optical setup, and data acquisition. We next turn to a detailed description of each constituent paying special attention to those experimental details necessary for an understanding of the reactive scattering experiments described in later chapters.

## 3.1 Vacuum Chamber and Reagents

The vacuum chamber (Fig. 3.1) consists of two differentially pumped chambers connected by a 6-mm diameter hole and separately pumped by two 6-inch, liquid-nitrogen-baffled diffusion pumps (Varian VHS-6 in the ionization region, and Varian M-6 in the detection region. Typical base pressures in both chambers are $5.0 \text{x} 10^{-8}$ Torr

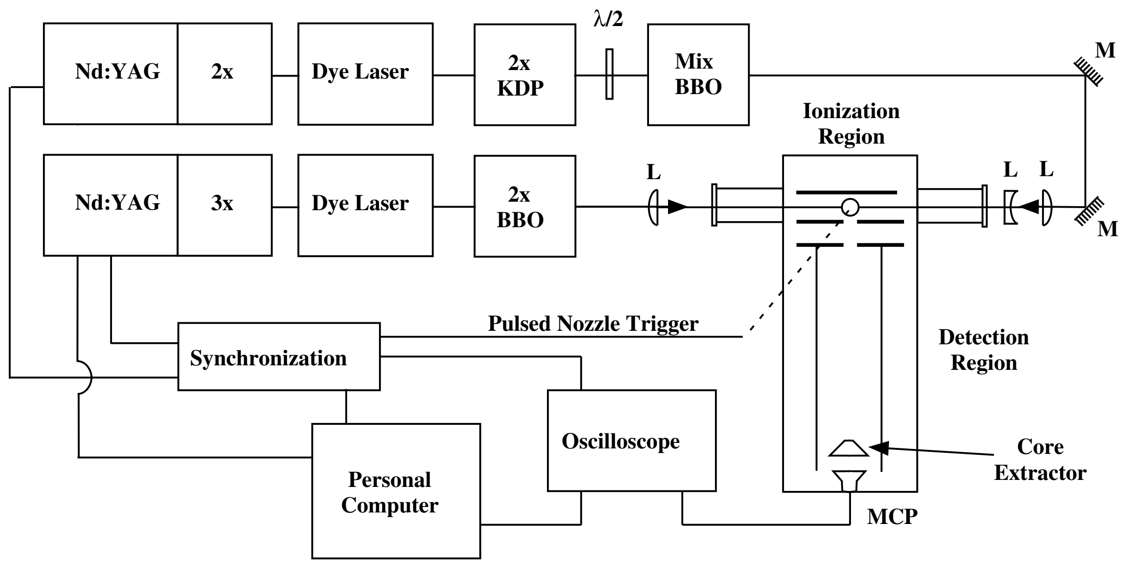


Figure 3.1: Schematic block diagram of the experimental setup (M ≡ dichroic mirror, L ≡ lens). The photolysis and probe laser beams traverse the ionization chamber along an axis perpendicular to both the time-of-flight and nozzle beam axes. For clarity, only one probe laser setup has been shown (See text for details).

as measured by a Bayard-Alpert ionization gauge (Granville Phillips). Under normal operating conditions, i.e., nozzle firing at 10 Hz with 300 Torr stagnation pressures, chamber pressures rise to 1.0-3.0x$10^{-5}$ Torr in the ionization region and 5.0-10.0x$10^{-7}$ Torr in the detection region.

The ionization region is equipped with two baffled, anti-reflection coated, fused silica windows for the entrance of the photolysis and probe laser beams. We use a counterpropagating laser beam geometry perpendicular to the time-of-flight axis. The ionization region also houses the extraction and acceleration stages of the time-of-flight spectrometer described in more detail in Section 3.2. The pulsed nozzle valve (General Valve Corporation, series 900 pulsed solenoid valve, 0.50 mm orifice) is driven by a IOTA ONE (General Valve Corporation) pulse driver. The valve delivers gas pulses of durations ranging from 400 to 600 $\mu$s.

A major concern is the reproducibility of the nozzle pulses over prolonged periods

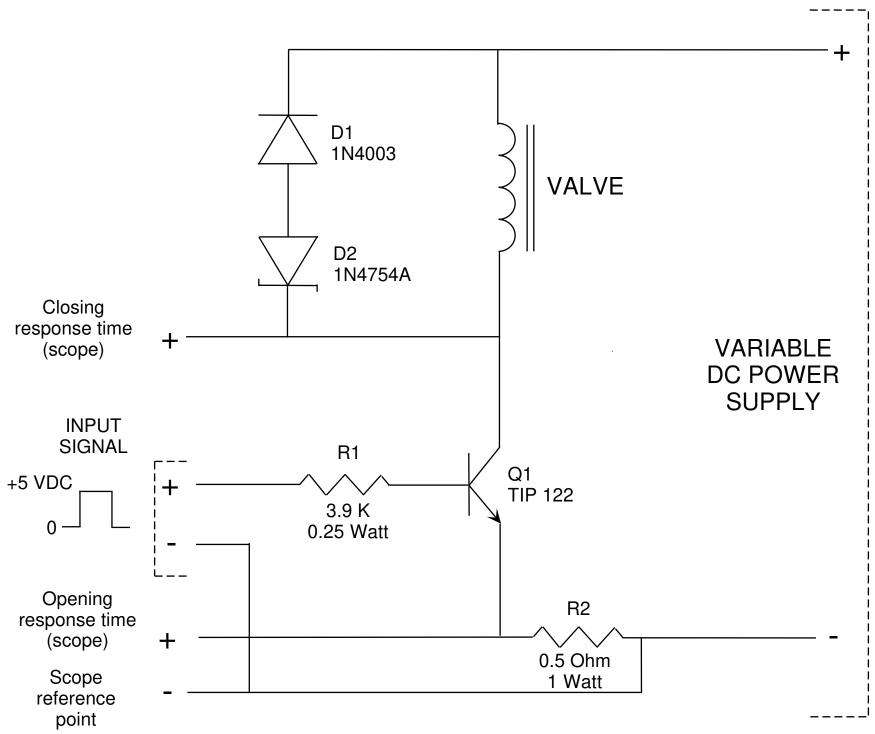


Figure 3.2: Circuit diagram for the adjustment of the pulsed solenoid valve.

of time. To this end, the performance of the solenoid valve is checked periodically by measuring its response to a TTL voltage pulse. Figure 3.2 shows the diagram of the circuit used for this purpose. Its major elements are a 28 V power supply for the valve coils and a transistor that couples the input pulse to the solenoid. The output of this circuit measures directly the time it takes for the nozzle armature to retract. A typical waveform is shown in Fig. 3.3. The additional bumps after the first dip correspond to the armature bouncing back and forth after it opens for the first time. Suitable response times for the series 900 solenoid valve are between 1.8 and 2.2 ms under low-voltage operation, i.e., the valve is not overriden. Taking care to keep the response times between the specified values ensures very reproducible operation from one experimental run to the next.

The nozzle assembly is attached to a XYZ vacuum manipulator (Vacuum Generators), and can be translated as close as 8 mm (16 nozzle diameters) to the center of the extraction region, where reaction takes place. The nozzle axis is perpendicular to

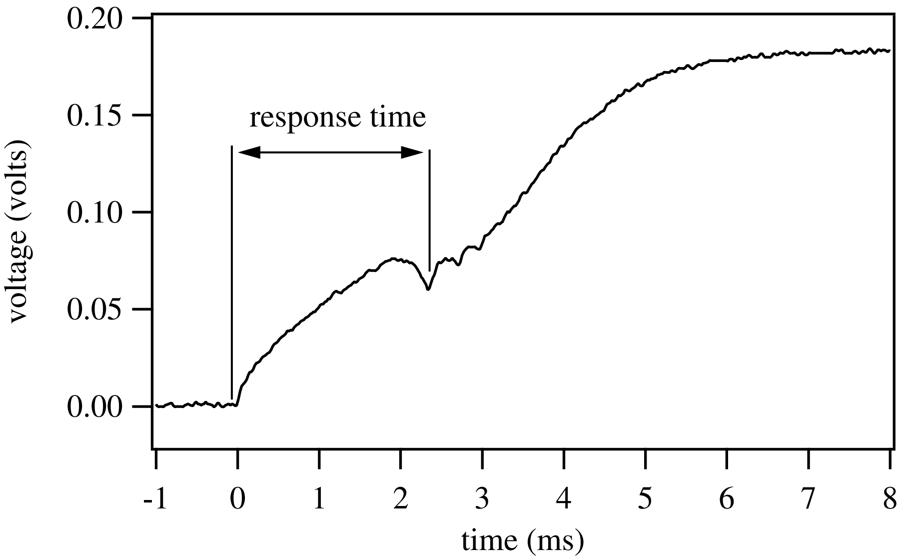


Figure 3.3: Typical waveform of the response of the solenoid valve to a 5 V voltage pulse. The first dip indicates the time it takes the armature to retract.

both the laser beams and the time-of-flight axis. A nude ionization gauge (Granville Phillips 274-025), conveniently located to one side of the nozzle axis, is used to generate $H_2$, HD, and $D_2$ molecules in high vibrational levels by flowing a small amount of gas over the filament at chamber pressures in the order of $10^{-5}$ Torr. Vibrational excitation is thought to proceed by molecular dissociation on the filament surface and subsequent recombination on the chamber walls [125–128]. This vibrationally excited molecular sample is used to find the spectroscopic transitions of the reaction products of interest.

The detection region contains the free-drift tube of the time-of-flight spectrometer. It also houses the multichannel plate (MCP) detector assembly (R. M. Jordan). The detector consists of two, one-inch, impedance-matched microchannel plates (Galileo Corporation) arranged in a Chevron configuration for optimal gain [129–131]. The total voltage drop across the plates is typically $2.0 - 2.4$ kV. A 90% transmission ion grid isolates the detector from the free-drift region and avoids electric field leakage.

HI or HBr (Matheson, 99.8% purity) and $D_2$ (Cambridge Isotope Laboratories, 99.8% purity) are premixed in a vacuum manifold held at base pressures of a few millitorr. The HI or HBr reagents are further purified by repeated freeze-pump-thaw cycles with liquid nitrogen prior to use. The reagent mix usually consists of a 1:4-10 mixture of HI/HBr and $D_2$. The reagent manifold consists of a teflon-lined stainless-steel reservoir and a cold finger for reagent purification. The manifold is periodically passivated by heating it to 150 C. Gases are fed into the chamber via a teflon gas line kept in a cold bath at temperatures ranging from -20 C to 0 C. This avoids accumulation of contaminants in the pulsed solenoid valve during experimental runs. The operating stagnation pressure, typically 200-300 Torr, is regulated by the use of a micrometer valve, and monitored with a diaphragm-type Baratron gauge.

## 3.2 Time-of-Flight Apparatus

Figures 3.4 and 3.5 present detailed diagrams of the time-of-flight spectrometer. The instrument consists of an extraction, acceleration, and free-drift regions. For this particular type of time-of-flight spectrometer, we showed in Section 2.3 that it is possible to attain space-focusing conditions, i.e., the ion arrival time is largely insensitive to the position of the ion at time zero. For the geometry of our instrument, Wiley-McLaren conditions are attained if the voltages of the repeller, extractor and time-of-flight plates are set at +V, −V, and −cV respectively, where c is a constant equal to 7.2. The absolute magnitude of V determines the ion arrival time. This choice of voltages also ensures that the center of the extraction region, where chemical reaction takes place, is at a potential of zero volts. By translating the probe laser beam across the extraction region we ensure that the Wiley-McLaren space focusing conditions are met by checking that the operating voltages yield position-independent time-of-flight profiles.

Figure 3.4 shows an enlarged view of the extraction region, which is equipped with a set of four stainless steel guard electrodes equally separated by 0.46 cm. The guard electrodes run parallel to the extraction and repeller plates and are held at well-defined voltages intermediate between +V and −V. The latter is achieved by using a resistive high-voltage divider to step down the voltage from +V (repeller plate) to −V (extractor plate). Each electrode receives a voltage according to its

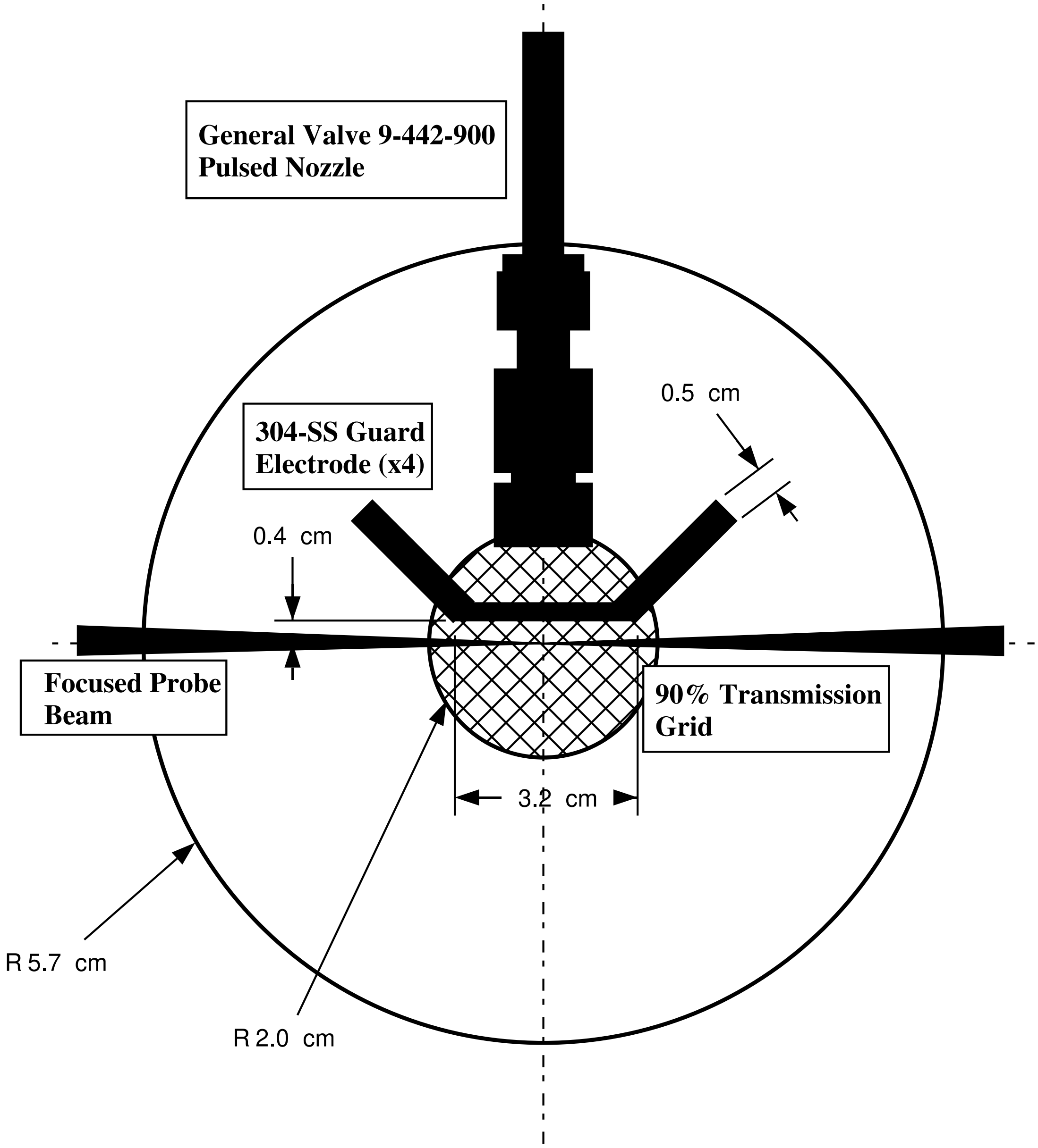


Figure 3.4: Detail of the extraction region showing the nozzle valve, guard electrodes and extraction plate assembly.

position so as to provide a constant electric field strength in the extraction region. The primary function of these guard electrodes is to prevent penetration of stray fields into the probe region. These stray fields and field inhomogeneities arise from the proximity of the stainless steel pulsed nozzle which is kept at ground potential (zero potential). Even though we also keep the center of the extraction region at a potential of zero volts, the physical size of the nozzle body can cause, in the absence of the guard electrodes, distortions of the electric field lines in areas of the extraction region sampled by ions as they are pushed toward the detector. The effect of these distortions on the time-of-flight lineshapes can seriously complicate the analysis of the experimental ion signals. Therefore, it is necessary to minimize these artifacts to the point we are no longer sensitive to changes in the time-of-flight profiles as the pulsed nozzle is translated inside the extraction region. The proper function of the guard electrodes has been tested via computer simulation of the instrument using the ion-optics software SIMION [132]. Simulations of ion trajectories with this program were particularly useful in the early stages of the design of the time-of-flight spectrometer. These simulations provided us with a reasonable set of distances and dimensions for the guard electrodes which showed no significant electric field leakage from the pulsed valve into the probe region. Later, we also checked experimentally the effect of nozzle proximity on flight times and peak shapes and found no distortions of the experimental time-of-flight profiles under normal operating conditions.

The free-drift region (Fig. 3.5) has a set of horizontal and vertical steering plates. Their voltage can be continuously varied about $\pm 10\%$ of the total TOF voltage to aid proper steering of the ion packet onto the detector. A mass gate is also used to avoid detection of the intense, high-mass backgrounds generated by the focused UV laser beams. This suppression is achieved by applying a 10 ns-risetime, 100-300 V pulse to the mass gate plate for a few microseconds, and has proven to be quite efficient at increasing the lifetime and reliability of the MCP detector. In principle, an equivalent approach to the use of a mass gate is to pulse the MCP detector gain for a few hundred nanoseconds so that only ions of a given mass-to-charge ratio are efficiently amplified [133–136]. In practice, attempts to pulse the detector gain using a high voltage pulser (DEI GRX-3.0K-L pulser) were not successful owing the large

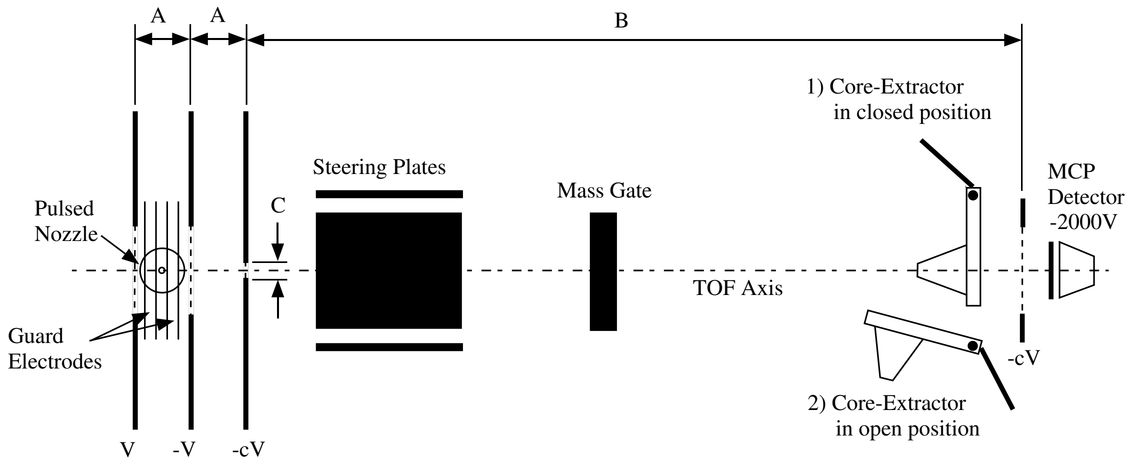


Figure 3.5: Bottom view of the time-of-flight apparatus showing the extraction (Fig. 3.4), acceleration, and free-drift regions of the instrument (A = 2.3 cm, B = 34.3 cm, and C = 0.6 cm).

amounts of electronic noise coupling to the detector anode and interfering with the signal of interest.

A set of two core extractors (Beam Dynamics) with different radii (3 mm and 1 mm) can be placed along the time-of-flight axis with the aid of vacuum manipulators (Vacuum Generators). Time-of-flight profiles can be obtained with and without the core extractor in place, depending on the purpose of the experiment, i.e., integral or differential cross section measurements.

## 3.3 Optical Setup

Linearly polarized photolysis radiation in the range of 200-300 nm and output powers ranging from 5 to 20 mJ/pulse are obtained by frequency doubling (KDP) and mixing (BBO) the output of a pulsed dye laser (Spectra Physics PDL-2) pumped by the second harmonic of a Nd:YAG laser (Spectra-Physics GCR-5). This setup allows the generation of H atoms at collision energies between 0.4 and 2.5 eV by the use of either HBr or HI as photolytic precursors. Most of the results described in this thesis have used HBr as the photolytic precursor. The doubled or tripled output of the photolysis laser is separated from the fundamental beam by the use of dichroic mirrors (CVI Corporation) specifically designed to reflect only the photolysis wavelengths. The beam, originally 7-8 mm diameter, is collimated by a 3:1 Galilean telescope and steered into the vacuum chamber. Collimation ensures that a large fraction of the precursor is photolyzed and also minimizes undesirable light scattering in the time-of-flight region.

Probe laser frequencies ranging from 200 to 700 nm are generated by various means. The EF $^1\Sigma_g^+ \leftarrow$ X $^1\Sigma_g^+$ (2+1) REMPI detection scheme is a well-established technique for the detection of $H_2$ and its isotopomers. The spectroscopic transitions for the $(\mathrm{v}' = 0, \mathrm{v}'' = 0 - 5)$ bands lie in the 200-250 nm region. Probe powers between 1.0 and 10 mJ/pulse are achieved by: (1) frequency tripling the red output of a dye laser (Lambda Physik SCANMATE 2E) pumped by the second harmonic of an injection-seeded Nd:YAG laser (Spectra Physics GCR-4); (2) frequency doubling and 1064 nm mixing the doubled green or yellow output of a dye laser (Lambda Physik LPD 3000) pumped by an injection-seeded Nd:YAG laser (Spectra Physics GCR-3); and (3) frequency doubling the blue output of a dye laser (Lambda Physik LPD 3000) pumped by the third harmonic (355 nm) of an injection-seeded Nd:YAG laser (Spectra Physics GCR-4). The UV output is separated and expanded with a 1:3 Galilean telescope prior to being focused by a 500-800 mm fused silica plano-convex lens. We have found that the use of a telescope prior to focusing the beam enhances the two-photon processes by at least one order of magnitude. The linewidth of each probe laser is around 0.25 $\mathrm{cm}^{-1}$ in the fundamental as measured with an etalon (Larry Wolford).

Half-wave and quarter-wave plates (Optics for Research and CVI Corporation) specifically designed to operate at these wavelengths control the polarization of both the photolysis and probe lasers prior to entering the vacuum chamber.

## 3.4 Data Acquisition

A 10-Hz, homemade master clock is used to trigger the experiment. This clock generates a steady 10-Hz signal by frequency rectification of the 60-Hz line. A set of four digital delay generators (Stanford Research Systems DG 535) control the timing of the photolysis and probe lasers as well as the nozzle pulse driver, oscilloscope, and time-of-flight mass gating. Ion signals arriving at the MCP detector are sent via shielded RG-59 cable to a 500 MHz oscilloscope (Tektronix TDS 620). The time-of-flight profiles are digitized and sent to a personal computer (PC Pentium 133 MHz) via an interface box (Stanford Research Systems SRS 245) and GPIB interfaces (National Instruments). The lasers are controlled from the personal computer via GPIB and RS232 serial interfaces. We use the oscilloscope in two different data acquisition modes. In the first mode we simply acquire the digital oscilloscope traces and average over a given number of laser shots to obtain a time-of-flight profile. This acquisition mode is well-suited to measure ion signals arising from a high-yield process such as a one-photon photodissociation. In the second mode, we use the oscilloscope as an ion counting device by specifying start and stop triggers and a dead time between single ion counts. This data collection scheme is well-suited to detect the low ion signals arising from chemical reactions. In addition, the use of single-ion counting allows us to avoid signal distortion, ringing and overshoot caused by large ion currents and impedance mismatches at the detector.

# Chapter 4

# Spectroscopy of the Hydrogen Molecule

*Faust: But from this house how may we get away*
*Where is thy coach, thy horses, servants, where?*

*Mephistopheles: This Mantle we have only to display,*
*It soon shall waft us thro' the air.*
*For the bold trip we are about to take*
*You must no heavy bundle make.*
*An ounce of gas, if duly rarefied,*
*(Which I at pleasure can provide,)*
*Will soon convey us out of sight*
*Of this dull spot.*

*J. W. von Goethe, "Faust"*

Finding new ways to detect and study the hydrogen molecule remains an active area of study and experimentation. This interest originates from several sources. The $H_2$ molecule is the lightest and simplest neutral molecule. Only two electrons hold the nuclei together in what we generically call a "chemical bond." As such, it becomes a very appropriate testing ground for the approximations that support the building of molecular physics, i.e., Born-Oppenheimer and Born-Huang approximations [137]. From a less puristic point of view, the $H_2$ molecule plays an important role in a variety of physical and chemical phenomena including vacuum-UV laser sources [138], the dynamics of molecular collisions [48], combustion [139], high-temperature plasmas and discharges [140, 141], and astrophysics [142–147].

In this chapter we will concentrate on an account of the current spectroscopic methods available today for the detection of this molecule in the gas phase. As such, its structure follows closely the logic followed when faced with the choice of planning the reactive scattering experiments that constitute the core of this thesis.

Section 4.1 will present a brief summary of the detection schemes one could in principle choose from. In Section 4.2 we will concentrate on (2+1) resonantly enhanced multiphoton ionization (REMPI) through the EF $^1\Sigma_g^+$ state of hydrogen, the technique we have chosen to use in our experimental work. Special attention is given to the nature of the REMPI process as well as the procedures to be followed for the extraction of meaningful physical information such as ground state populations and angular momentum spatial anisotropy. Examples will be drawn from the work we have carried out during the course of the experiments on the hydrogen-atom hydrogen-molecule exchange reaction since these examples and the conclusions from this section directly apply to the various aspects of the detection process. Finally, we devote Section 4.3 to a discussion of alternative multiphoton schemes for the hydrogen molecule, a topic which is currently being investigated to greater lengths in this laboratory.

## 4.1 Spectroscopic Detection Methods: an Overview

The hydrogen molecule has been investigated thoroughly during the last century. As a homonuclear diatomic molecule, the lack of a dipole moment makes conventional infrared spectroscopy useless for the study of the the ground state rovibrational energy

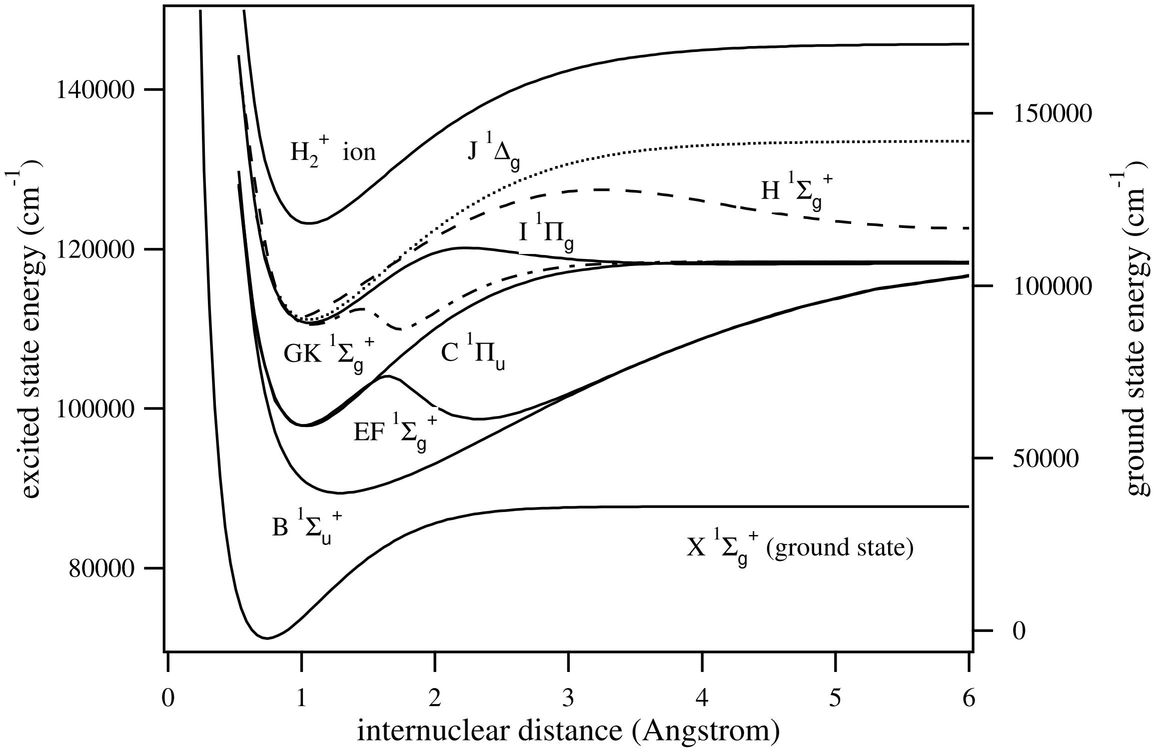


Figure 4.1: Potential energy curves for the ground and several excited electronic states of the $H_2$ molecule.

levels. In the case of the HD isotopomer, the dipole moment is so small ($\sim 10^{-4}$ Debye) that only absorption experiments using long path length and multipass spectrometers have been possible [148]. Given these physical limitations, the only way to carry out spectroscopic studies of the hydrogen molecule has been via electronic or Raman spectroscopies.

Figure 4.1 shows some of the electronic states of the hydrogen molecule. The potential energy curves have been obtained from spline fits of the ab initio points reported by Wolniewicz and co-workers [149–157] in the past three decades. The only extensive compilation of potential energy curves and spectroscopic constants is due to Sharp [158] dating back to 1971 and can be considered mostly outdated by now. Parity rules show that the two lowest electronic states, labelled B $^1\Sigma_u^+$ and C $^1\Pi_u$, can only be accessed by an odd number of photons. The transition frequencies in both cases lie in the vacuum ultraviolet region (VUV) of the electromagnetic spectrum for a one-photon transition. Light sources in this frequency regime are not easy to construct and control. In the past few years, laser sources have been designed to reach these wavelengths via non-linear frequency mixing in rare gases [159–166]. This has fostered numerous studies of the excited states of hydrogen particularly by the use of double resonance techniques. In typical double resonance experiments, the VUV photon is tuned with a particular B $^1\Sigma_u^+ \leftarrow$ X $^1\Sigma_g^+$ or C $^1\Pi_u \leftarrow$ X $^1\Sigma_g^+$ transition. A second, less-energetic photon is used to probe higher excited states. These techniques have provided a wealth of spectroscopic information. Ubachs and co-workers have recently perfomed systematic spectroscopic studies of several high-lying excited states of this molecule including the B $^1\Sigma_u^+$, C $^1\Pi_u$, and EF $^1\Sigma_g^+$ states of the HD molecule [167, 168], the H$\bar{\text{H}}$ $^1\Sigma_g^+$ state in $H_2$ and $D_2$, the B$''$B $^1\Sigma_u^+$ state in HD [169], and the I$'$ $^1\Pi_g$ outer well state in $H_2$ and $D_2$ [170]. In the particular case of the HD molecule, investigation of the H $^1\Sigma_g^+$ and B $^1\Sigma_u^+$ electronic states [171] has assessed the presence of strong adiabatic interactions between energy levels, implying complete gerade-ungerade symmetry breaking over a wide range of molecular quantum states. Tsukiyama and co-workers have also studied high-lying vibrational levels of the EF $^1\Sigma_g^+$ state in $H_2$ [172], and measured fluorescence lifetimes from the EF $^1\Sigma_g^+$, GK $^1\Sigma_g^+$, H $^1\Sigma_g^+$, I $^1\Pi_g$ and J $^1\Delta_g$ states in $H_2$ [173], as well as from the H $^1\Sigma_g^+$ and EF $^1\Sigma_g^+$ states in $D_2$ [174]. The use of one-photon techniques as the one described has its advantages. Their high sensitivities require very modest laser powers, comparable to those obtained via frequency mixing and tripling techniques (usually in the order of a few nanojoules/pulse using nanosecond laser technology). On the other hand, tunability is always a problem especially in the case of the hydride family, characterized by large frequency spacings between successive rotational lines.

A variant of these VUV probing techniques, called molecular Rydberg tagging, has been pioneered in our laboratory for the detection of HD [175, 176]. A VUV photon excites a particular rovibrational state of the ground state into the B $^1\Sigma_u^+$ state. A second photon is used to take the molecule to a high-lying Rydberg state close to the ionization threshold. In analogy to the atomic case, high-lying molecular Rydberg states have very long lifetimes (in the order of $\mu$s) [177–179]. After a given temporal delay, the molecule is field-ionized by a voltage pulse and detected. This approach has been utilized to probe the HD($v' = 4, J' = 3$) from the $H + D_2$ reaction at 2.2 eV [120]. The sensitivity of the technique is very high, comparable to the analogous H-atom Rydberg tagging detection scheme [180]. However, the presence of additional dynamical processes leading to ionization and breakage of the Rydberg HD molecule limits its generality to only a handful of favourable cases where the excited state lifetime is well-behaved. Small changes in the quantum number of the Rydberg state can lead to dramatic changes in the excited state lifetime. These complications need to be characterized if the technique is to find useful application as a quantitative and reliable detection method for molecular hydrogen.

A different approach to the detection of the hydrogen molecule involves the use of multiphoton processes [181–186]. Fig. 4.1 shows some of the gerade states accessible via a two-photon transition. Of all these possible transitions, the only one which has been studied in detail involves the EF $^1\Sigma_g^+$ double-well state. The frequencies required for this two-photon transition lie above 200 nm, wavelengths easily accessible with conventional dye lasers and non-linear optical doubling and mixing in BBO crystals. With typical laser output powers at these wavelenghts, mild focusing of the laser beam can yield sensitivities close to those attained via one-photon transitions. A more complete account of this detection scheme will be given in Section 4.2. All the other gerade states lie higher in transition energy and have not been studied via two-photon spectroscopy. Similarly, there have been some reports of three-photon spectroscopic studies of the ungerade B $^1\Sigma_u^+$ [187], C $^1\Pi_u$ [188], and D $^1\Pi_u$ [189] states. The low cross section for three-photon transitions make these schemes much less sensitive and can only be used for the detection of relatively large number densities of hydrogen.

Another variant of the multiphoton schemes described above is coherent anti-Stokes Raman scattering (CARS) [190]. A CARS transition is driven by use of two optical frequency laser beams for which the difference frequency, $\omega_1 - \omega_2$, is equal to the difference between two rovibrational energy levels of the ground state molecule. This excitation produces a resonance enhancement in the four-wave mixing process that generates a coherent optical beam at frequency $\omega_0 = 2\omega_1 - \omega_2$. This allows the recording of a Raman spectrum by monitoring the intensity of the $\omega_0$ signal beam as the frequency difference $\omega_1 - \omega_2$ is scanned. The commercial availability of high-power tunable pulsed dye lasers makes this technique easy to implement. The Raman basis of CARS is also responsible for its major disadvantage, namely, the modest absolute sensitivity, typically between $10^{+12} - 10^{+13}$ molecules per cm$^3$ per quantum state. This drawback is partially remedied by using high-power lasers, but effects like Stark broadening and, ultimately, optical breakdown of the sample set practical limits to how intense a laser pulse can be used. CARS has been one of the techniques of choice for the detection of hydrogen molecules from the hydrogen exchange reaction by the group of Valentini [42]. The same group has characterized the CARS detection scheme for the hydrogen family [191], thus allowing a reliable extraction of ground state rovibrational populations. It must be noted, however, that the use of CARS has faded away in favor of other spectroscopic techniques with inherent superior sensitivities as is the case of one-photon and multiphoton ionization schemes.

## 4.2 EF $^1\Sigma_g^+ \leftarrow$ X $^1\Sigma_g^+$ (2+1) REMPI

### 4.2.1 Generalities

In resonance-enhanced multiphoton ionization (REMPI), the wavelength is tuned to a particular electronic transition between the ground state and an excited state. In the second step, the atom or molecule is sent above the ionization threshold resulting in the formation of the corresponding ion. In the case of the EF $^1\Sigma_g^+ \leftarrow$ X $^1\Sigma_g^+$ transition, two photons are utilized to promote ground state molecules to a given rovibrational level of the EF $^1\Sigma_g^+$ state and a third photon ionizes the molecule, thereby the name (2+1) REMPI. The observation of two-photon excitation to the EF $^1\Sigma_g^+$ state was first performed by Kligler and Rhodes [192] by detecting the fluorescence between the EF $^1\Sigma_g^+$ and B $^1\Sigma_u^+$ states. It was soon after realized that direct ionization caused by the large laser fluences required for the two-photon transition could be used to enhance the sensitivity of the technique [193, 194]. Marinero, Vasudev, and Zare [160] performed the first detailed characterization of this transition with the objective of using it for quantum-state-specific detection of hydrogen molecules from the hydrogen exchange reaction [41]. Since then, this particular REMPI scheme has been used in subsequent studies of this reaction in our and other laboratories. As a consequence, it has been characterized in detail as evidenced by the large number of studies devoted to this particular transition [195–203].

### 4.2.2 Sensitivity of the Technique

We would like first to gain some insight as to why this two-photon transition followed by ionization stands as the method of choice for the detection of hydrogen molecules. In the time-of-flight instrument described in Chapter 3, it is possible to detect very small concentrations of this molecule. At chamber pressures in the order of $10^{-8}$ Torr at room temperature, it is possible to attain signal-to-noise ratios of $100 - 1000$ when detecting a single quantum state. Taking the number density at room temperature to be ca. $3\text{x}10^{+15}$ $\text{cm}^{-3}$ $\text{Torr}^{-1}$, this signal level translates into a sensitivity of $10^{+5} - 10^{+6}$ molecules per $\text{cm}^3$ per quantum state in contrast, for example, with the detection limits of other non-linear techniques like CARS ($10^{+12} - 10^{+13}$ molecules per $\text{cm}^3$ per quantum state). Taking a confocal parameter of 0.5 cm and a laser beam spot size of 100 $\mu$m, that is, a focal volume of approximately $5\text{x}10^{-5}$ $\text{cm}^{-3}$ we can see that this particular technique has the capability of detecting between $1 - 10$ hydrogen molecules located within the laser detection volume.

This estimate of the sensitivity of the hydrogen (2+1) REMPI scheme compares quite favorably with the value of $10^{+5}$ molecules per $\text{cm}^3$ per quantum state reported by Lykke et al. [204], and obtained by careful calibration of ion signals against two-photon direct absorption.

### 4.2.3 Extraction of Rotational Populations

To make REMPI detection quantitative, the measured ion signal must be related to physically significant observables such as the ground state population. The use of nanosecond pulsed lasers to effect the REMPI process allows for a rate kinetic analysis of the absorption, ionization and other decay processes taking place during the interaction of the molecule with the laser field [205]. In those cases where it is possible to establish coherences between the ground and excited states, more complicated treatments involving a density matrix formalism need to be invoked [206]. Since our laser sources are not perfectly stable, the first correction that needs to be made to the raw ion signals needs to account for the fluctuations in laser power as the laser wavelength is scanned. At first sight, and based on simple kinetic arguments, one may expect that since there are three photons involved in the REMPI process, the power dependence should be cubic. This is rarely the case because the ionization step tends to saturate before the two-photon step and, therefore, photoionization line strengths [207, 208] need not be taken into account. We note that this is characteristic of a (2+1) process but not of (2+2) or (1+1) REMPI schemes. In Fig. 4.2 we show a typical laser power dependence of the laser signal for the detection of ground state $D_2$ molecules. The power exponent is close to 2.5, which indicates that the ionization step is partially saturated. The power dependence of the ion signal is highly dependent on experimental factors such as beam spatial and temporal profile, focusing conditions, etc. As a good rule of thumb, it should be checked regularly so as to avoid an improper treatment of the ion signal. Theoretical predictions based on approximate treatments of the REMPI process show that for experimental arrangements involving a single focusing lens ("dog-bone" geometry) the smallest power exponent should be 3/2, the so-called "spatially saturated regime" [209, 210].

The theory of two-photon line strengths is slightly more complicated than the one-photon case since it involves a coherent sum over intermediate virtual states taking part in the two-photon process. Theoretically, the problem has been worked out for the case of diatomic [211–213], symmetric [214–216] and asymmetric [217] top molecules. Additionally, Girard et al. [218] and Xu et al. [219] have addressed the effects of the ac Stark effect on the line strength and line shape of multiphoton resonances. In our particular case of a $\Sigma - \Sigma$ transition, both the ground and excited state have the same symmetry. Selection rules only allow for O, Q, and S branches of which the Q branch is by far the most intense. The expressions for the rotational line strengths using linearly polarized excitation are given below. More general expressions

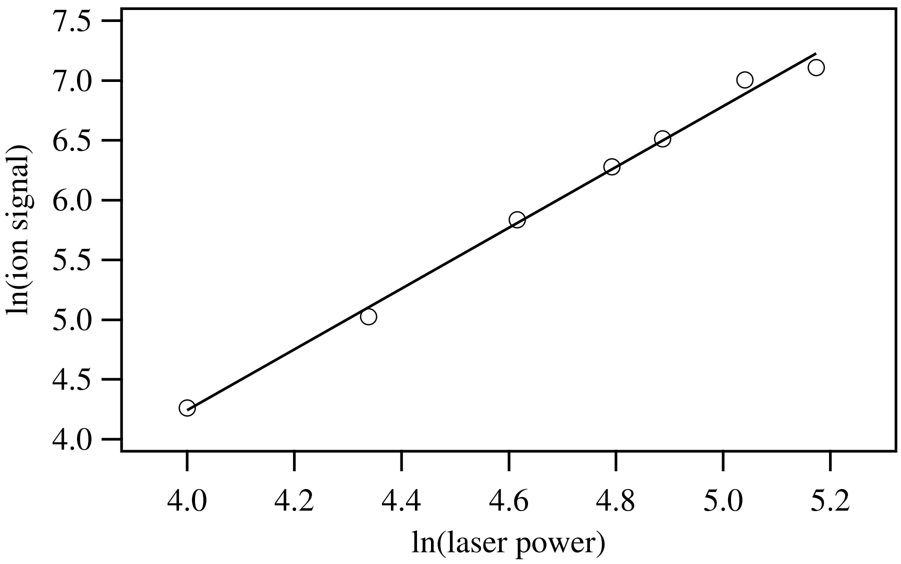


Figure 4.2: Typical power dependence of the ion signal for (2+1) REMPI of $D_2$. The power exponent of $2.54 \pm 0.10$ results from a linear regression of this log-log plot.

may be found in the paper by Chen and Yeung [214]

$$O\ branch: \quad \frac{J^2\,(J-1)^2}{30J\,(J-1)\,(2J-1)\,(2J+1)} \cdot \mu_s^2 \tag{4.1}$$

$$Q\ branch: \quad \frac{1}{9} \cdot \mu_i^2 + \frac{J^2\,(J+1)^2}{45J\,(J+1)\,(2J-1)\,(2J+3)} \cdot \mu_s^2 \tag{4.2}$$

$$S\ branch: \quad \frac{(J+2)^2\,(J+1)^2}{30\,(J+1)\,(J+2)\,(2J+3)\,(2J+1)} \cdot \mu_s^2 \tag{4.3}$$

where J is the rotational quantum number of the ground state and $\mu_\mathrm{i}^2$ and $\mu_\mathrm{s}^2$ are transition dipole moments corresponding to symmetrized linear combinations of the distinct virtual state paths possible for this type of electronic transition. More explicitly,

$$\mu_i^2 = \mid R_{ei}^0 R_{fe}^0 - R_{ei}^{+1} R_{fe}^{-1} - R_{ei}^{-1} R_{fe}^{+1} \mid^2 \tag{4.4}$$

$$\mu_s^2 = \mid 2R_{ei}^0 R_{fe}^0 + R_{ei}^{+1} R_{fe}^{-1} + R_{ei}^{-1} R_{fe}^{+1} \mid^2 \tag{4.5}$$

where $R_{xy}^{\Delta\Lambda}$ is a radial dipole moment integral for a single-photon transition between electronic states x and y which is characterized by a change in the projection of the electronic angular momentum $\Delta\Lambda = 0, \pm 1$. The subscripts i,e, and f correspond to the initial, intermediate and final electronic states respectively.

As shown in Eq. (4.2), the line strengths for Q-branch transitions has both J-dependent and J-independent terms. It is generally the case that the first (and J-independent) term dominates over the second. Therefore, and to a very good approximation, the transition line strength is practically independent of rotational quantum number. This fact implies that power-corrected ion signals should be proportional to the rotational population of the lower level. In Fig. 4.3 we show the Q-branch spectrum of $D_2$ at room temperature. The top spectrum is the raw ion signal whereas the middle spectrum has been corrected for fluctuations in the laser power as the wavelength is scanned using the power dependence shown in Fig. 4.2. The bottom pannel shows the corresponding Boltzmann plot from which a rotational temperature of $290 \pm 10$ K can be derived. Note that to obtain such a temperature one needs to correct for the differences in nuclear spin degeneracy between even and odd rotational levels.

### 4.2.4 Sensitivity to Rotational Polarization

In the previous section we described how the Q-branch of the EF $^1\Sigma_g^+ \leftarrow$ X $^1\Sigma_g^+$ transition may be used to extract rotational populations. We, however, provided a rather ad hoc justification as to why this may be the case by arguing that the dominant term in the expression for the rotational line strength was J-independent (cf. Eq. (4.2)). In general, the (2+1) REMPI ionization probability is not only dependent on rotational quantum number but also on the spatial distribution of angular momenta, which in quantum mechanical terms it implies an implicit dependence on the magnetic sublevels. Kummel, Sitz and Zare [220, 221] have addressed this issue using the spherical tensor formalism [222] and the Hertel-Stoll convention [223]. In the case of a two-photon resonant transition using linearly polarized it is possible to

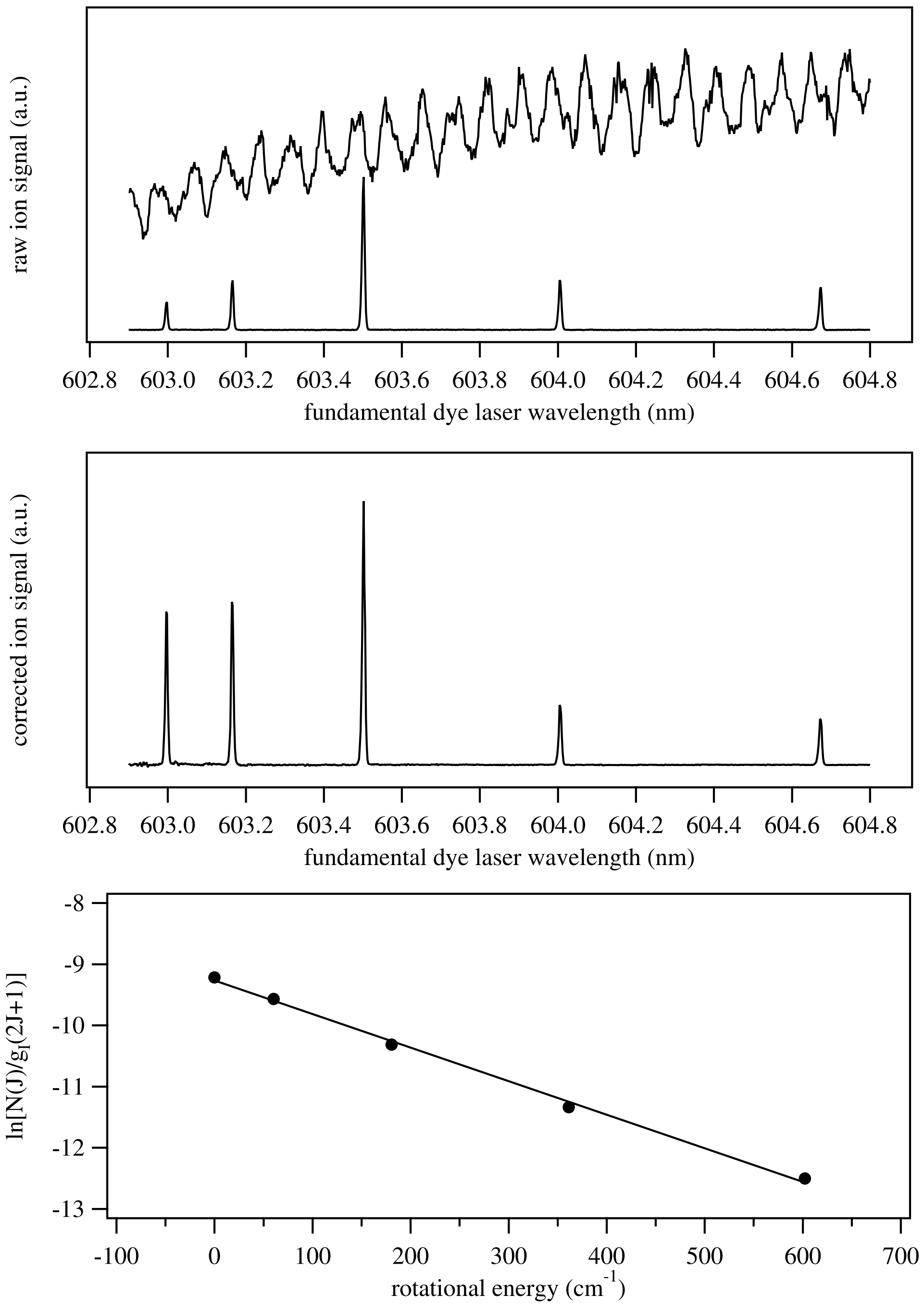


Figure 4.3: (a) (2+1) REMPI spectrum of the $D_2$ molecule at room temperature. (b) Spectrum corrected for power fluctuations. (c) Boltzmann plot yielding a rotational temperature of $290 \pm 10$ K.

write the transition probability as

$$I = C_{det} \cdot \sum_{k,q} P_q^k \left(J_i, \Lambda_i, J_f, \Lambda_f, \Omega\right) A_q^k \left(J_i\right) \tag{4.6}$$

In Eq. (4.6) the $\mathrm{P_q^k}$ 's are the moments of the line strength and the $\mathrm{A_q^k}$ 's are the moments of the ground state distribution. $\mathrm{C_{det}}$ is a detector sensitivity constant. The moments of the line strength are the logical extension of the more common rotational line strengths which are obtained by summing an M-dependent transition probability over all magnetic sublevels. These moments of the line strength $\mathrm{P_q^k}$ are dependent on the quantum numbers for the ground and excited rotational states as well as on the excitation-detection geometry which here we signify by the collective index $\Omega$. The range of index k in Eq. (4.6) depends on the number of photons involved in the resonant step as well as on the type of polarization. For a two-photon transition using identical photons (i.e., same laser) and linear polarization we are only sensitive to the even k moments up to $\mathrm{k = 2n}$ where $\mathrm{n} = 2$. For each k we have $\mathrm{q = -k, -k+1, ..., k+1, k}$ moments of the line strength and ground state angular momentum spatial distribution. The moments of the line strength represent the sensitivity for a given experimental geometry to a particular spherical tensor component $\mathrm{A_q^k}$. Sensitivity to just the ground state population, as we have assumed in the previous section, implies that all the $\mathrm{P_q^k}$ 's are zero except $\mathrm{P_0^0}$.

Kummel, Sitz and Zare [220, 221] have tabulated the complete expressions that allow the calculation of the moments of the line strength for any type of two-photon transition in a diatomic molecule with good quantum labels $\mathrm{J_i}$ and $\Lambda_\mathrm{i}$. The reader is referred to the original papers by these authors for explicit expressions [220, 221] or to the more recent and simpler derivation of two-photon geometrical factors by Mo and Suzuki [224]. In general, calculation of these factors does not involve more than extensive angular momentum algebra. Unfortunately, for our particular case of a Q branch of a $\Sigma - \Sigma$ transition we need to know the relative contributions of the $\Sigma - \Sigma - \Sigma$ and $\Sigma - \Pi - \Sigma$ virtual paths. A hint to the need to know this extra amount of information was already given when we presented the rotational line strengths for the Q-branch which depend on both $\mu_\mathrm{S}$ and $\mu_\mathrm{i}$. In Fig. 4.4 we show a partial (2+1) REMPI spectrum of HD at room temperature showing the Q(3)

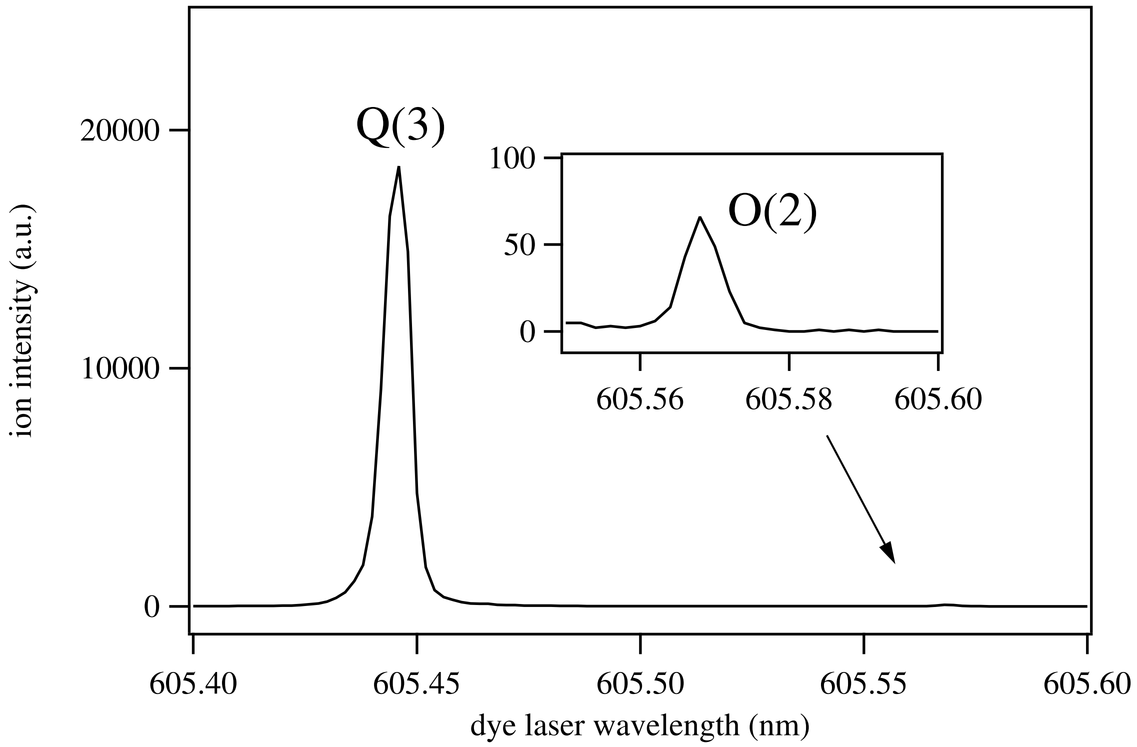


Figure 4.4: (2+1) REMPI spectrum of HD showing O and Q-branch transitions.

and O(2) lines. Using Eqs. (4.1) and (4.2), and accounting for the differences in rotational populations from J = 2 and J = 3, we can arrive at a ratio of transition dipole moments given by

$$\frac{\mu_i^2}{\mu_s^2} \approx 25 \tag{4.7}$$

A similar ratio of $\sim 27$ is obtained if we compare the intensities between Q(6) and O(4) in the same room-temperature spectrum. This value is about five times larger than the one reported previously by Marinero and co-workers [160] and which was obtained by comparison of the intensities of the Q(0) and S(2) lines in the $H_2$ molecule. Inspection of the line strength formulae used by these authors to obtain this ratio reveals the inclusion of an extra (2J+1) factor in the expression for the S-branch line strength which accounts for the observed difference. Correct line strength expressions using the Bray-Hochstrasser formalism have been tabulated by Kummel, Sitz and Zare [220].

From the observed ratio of the squares of the transition dipole moments we can arrive at two possible values for the ratio of transition strengths. Using Eqs. (4.4) and (4.5) we can write

$$\rho = \frac{R^0_{ei} R^0_{fe}}{R^{+1}_{ei} R^{-1}_{fe}} = \frac{1 + \frac{\mu_i}{\mu_s}}{\frac{1}{2} - \frac{\mu_i}{\mu_s}} \tag{4.8}$$

where the fraction $\mu_i/\mu_s$ can be positive or negative since we have only measured the square of this ratio, i.e., we have not measured the relative phases between the two transition amplitudes. For our particular case this leads to a ratio of radial terms of $-1.33$ or $-0.73$. Table 4.1 lists the sensitivities to various spherical tensor moments of the J-distribution by taking explicit account of these two possible virtual path ratios. In this table we have listed "sensitivities" in the following sense. The $P^k_q$ moments of the line strength for the case of an orthogonal excitation-detection geometry can be factored out as follows [225]

$$P^k_q = s^k(J_i, \Lambda_i, J_f, \Lambda_f, \rho) Y^k_q(\Delta, 0) \tag{4.9}$$

where $s^k$ is the k-dependent sensitivity constant which only depends on the quantum numbers of the initial and final states, as well as on the virtual state character of the two-photon transition. $Y^k_q(\Delta, 0)$ is a spherical harmonic of rank k and component q, and $\Delta$ is the angle between the polarization of the laser and the detection axis. Explicit trigonometric expressions for the spherical harmonics up to rank five can be found in the text by Varshalovich et al. [226].

The figures listed on Table 4.1 for the second and fourth $s^k$ moments have been normalized by the zeroth-order value so as to provide an indication of the relative contributions of each term to the overall intensity. We have listed these sensitivities for a few initial rotational quantum numbers since they are slightly J-dependent. Past J = 5 it is clear that the high-J limit has been reached. The sensitivities to the second and fourth moments are much smaller than to the zeroth moment. This is more so for the fourth moment where the contribution to the overall intensity amounts to only a

| J | $s^2/s^0$ | $s^4/s^0$ |
|---|---|---|
| 1 | -0.075 | 0 |
| | 0.068 | 0 |
| 3 | -0.049 | 0.002 |
| | 0.046 | 0.002 |
| 5 | -0.046 | 0.002 |
| | 0.045 | 0.002 |
| 8 | -0.046 | 0.002 |
| | 0.044 | 0.002 |
| 20 | -0.046 | 0.002 |
| | 0.044 | 0.002 |

Table 4.1: Sensitivities to the normalized second and fourth order moments of the ground state distribution using the Q-branch members of the EF $^1\Sigma_g^+ \leftarrow$ X $^1\Sigma_g^+$ two-photon transition. For a given rotational quantum number the first row corresponds to a virtual path ratio of -1.33 and the second row to -0.73.

fraction of a percent. For the second moment, the contribution can be at most seven to eight percent. In the computation of these values we have not taken into account the effects of nuclear spin depolarization and, therefore, they must be regarded as strict upper estimates. Nuclear spin depolarization is expected to be smallest for $H_2$ with a nuclear spin-rotation interaction constant of $-113.9 \pm 0.03$ kHz [227], and largest for $D_2$, which possesses a permanent quadrupole moment in each nucleus with an electric quadrupole coupling constant of $225.044 \pm 0.024$ kHz [228, 229]. The precise value of the nuclear spin depolarization factor depends on the rank k of the distribution moment as well as on the temporal delay between product formation and detection [230–232]. If we ascribe a characteristic timescale to the hyperfine depolarization, denoted $\tau$, which we define by

$$\frac{1}{\tau} \approx hyperfine\ coupling\ constant\ (Hz), \tag{4.10}$$

we immediately see that timescales for depolarization are in the order of 5-10 $\mu$s whereas typical probe delays are tens of nanoseconds. Therefore, the effects of hyperfine depolarization can be neglected.

Additional evidence for the lack of sensitivity to the rotational anisotropy comes from the calculation of the photoelectron angular distributions by Cornaggia et al. [233] and the photoelectron spectra of McCormack et al. [234], both consistent with an unaligned excited state distribution arising from an isotropic ground state. This finding implies that the ionization probability is dominated by an M-independent (isotropic) term. Similar calculations as the ones presented here to ascertain the insensitivity of the Q-branch members of the EF $^1\Sigma_g^+ \leftarrow$ X $^1\Sigma_g^+$ transition to angular momentum polarization have been carried out by Kummel and co-workers in their characterization of the a$''$ $^1\Sigma_g^+ \leftarrow$ X $^1\Sigma_g^+$ (2+1) REMPI in the nitrogen molecule [235, 236]. The two-photon resonant step has a virtual-state path ratio of approximately 12, a factor of two smaller than what we have found for the hydrogen molecule. The smaller path ratio makes this transition more sensitive to the higher moments. These studies, however, have shown that it is possible to obtain information about the second-order moments of the spatial distribution of angular momenta from the Q branch in cases of exceedingly good signal-to-noise ratio, i.e., minute signal intensity changes upon rotation of the laser polarization are above experimental noise.

## 4.3 Other REMPI Transitions

We have established in the previous section that the EF $^1\Sigma_g^+ \leftarrow$ X $^1\Sigma_g^+$ (2+1) REMPI scheme for the hydrogen molecule and isotopomers is mostly sensitive to the rotational population if we restrict its use to the Q-branch members of this two-photon transition. Additional information regarding the spatial distribution of angular momenta could be readily obtained by using the O or S branches. Unfortunately, the intensity of these spectroscopic branches is one or two orders of magnitude smaller than the Q branch and, therefore, can only be used in experiments where the hydrogen number density is sufficiently high. There is a need, therefore, to look for other electronic states in this molecule which are intrinsically sensitive to the rotational

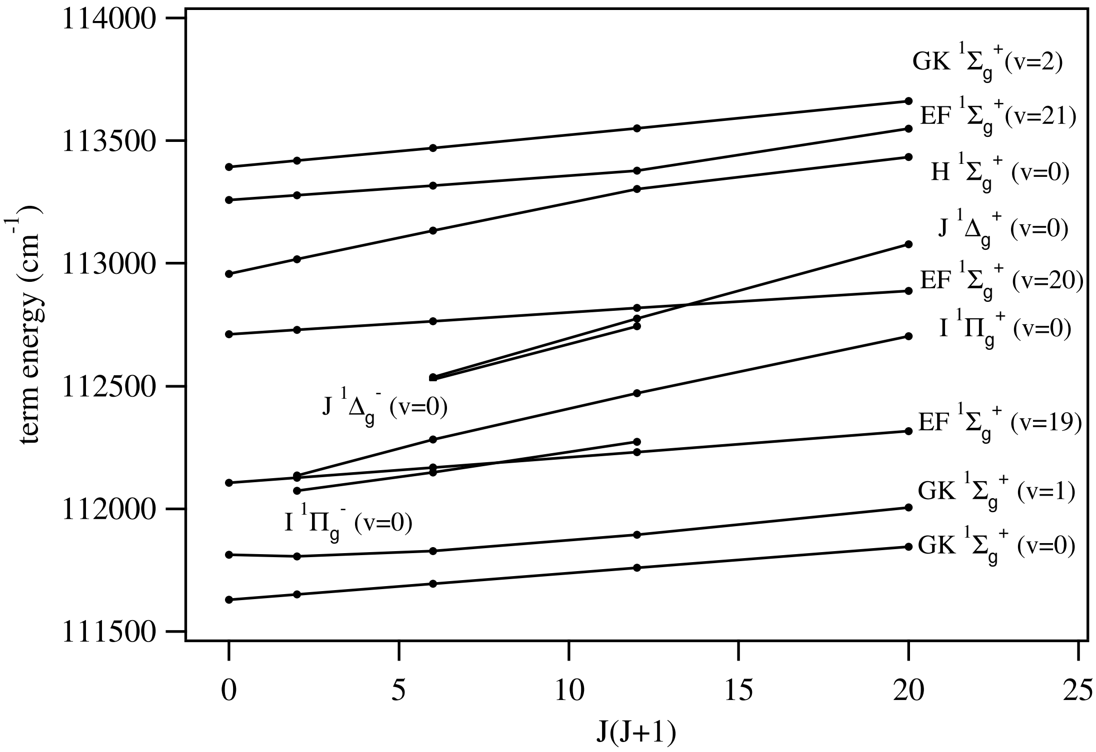


Figure 4.5: Term diagram for some of the excited gerade states of the $H_2$ molecule. Given their gerade symmetry, they may be accessed by two-photon excitation.

anisotropy.

In the case of the hydrogen molecule, there are several electronic states above the EF $^1\Sigma_g^+$ state that meet this requirement. Figure 4.5 shows a term diagram with several electronic states which may be accessed by (2+1) REMPI from the ground state. The laser wavelengths lie below 200 nm. These wavelengths can be generated in most cases by frequency tripling in BBO crystals. The term energies shown in this figure have been taken from the compilation of Jungen, Dabrowski, Herzberg, and Vervloet [237], and they comprise the most accurate experimental and ab initio values known. Of all these states the I $^1\Pi_g$ and J $^1\Delta_g$ are the best candidates since their nonzero electronic angular momentum guarantees the existence of O, P, Q, R, and S branches, all quite sensitive to moments of the angular momentum distribution up to rank four.

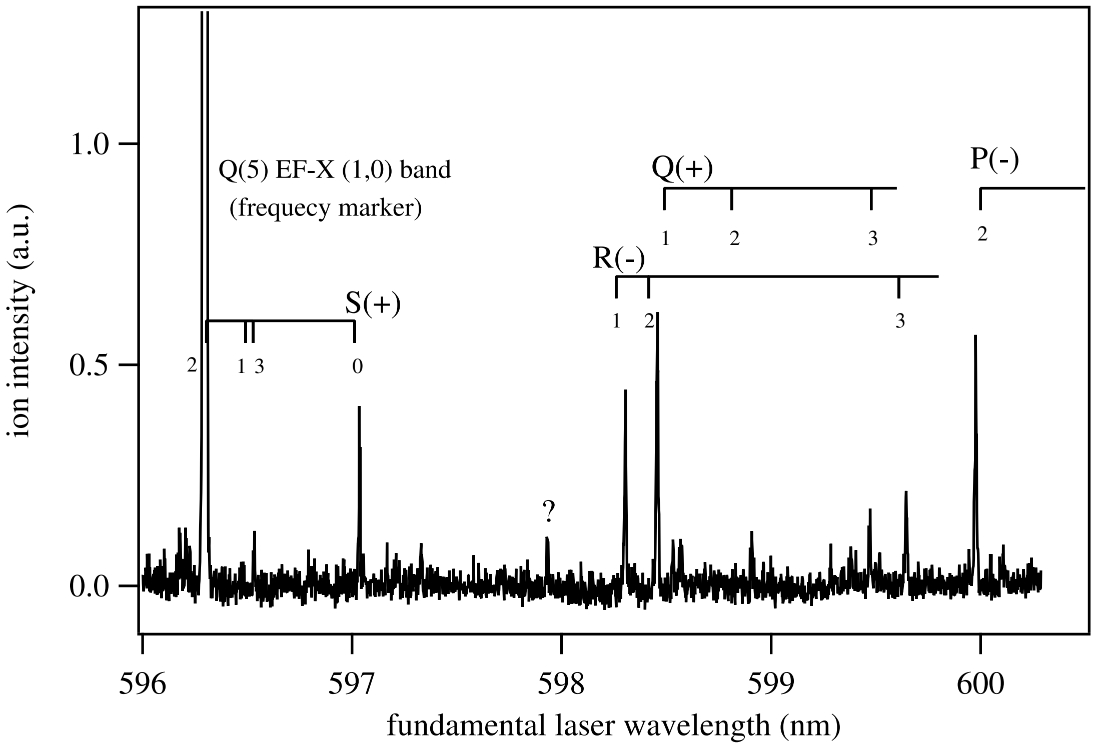


Figure 4.6: $H_2$ (2+1) REMPI spectrum ca. 198-200 nm.

Figure 4.6 shows a (2+1) REMPI spectrum of the hydrogen molecule around 198-200 nm. At these wavelengths it is possible to access the (0,3) band of the I $^1\Pi_g \leftarrow$ X $^1\Sigma_g^+$ transition. The spectrum also shows the Q(5) line from the EF $^1\Sigma_g^+ \leftarrow$ X $^1\Sigma_g^+$ (1,0) band which serves as a convenient frequency marker. The origin of the spectroscopic lines shown in this figure can be easily checked by turning on and off the ion gauge that generates the vibrationally excited $H_2(\mathrm{v} = 3, \mathrm{J})$ sample (see Chapter 3, Section 3.1). By turning off the source of excited hydrogen molecules, only the frequency markers remain in the spectrum. We have also included a preliminary assignment of the ion-gauge-dependent spectroscopic lines, that is, those corresponding to transitions through the I $^1\Pi_g$ state. Parity rules for the two-photon step dictate that the O, Q, and S branches can only correlate with the $\Pi^+$ doublet whereas P and

| | $s^2/s^0$ | | | | | $s^4/s^0$ | | | | |
|---|---|---|---|---|---|---|---|---|---|---|
| J | O | P | Q | R | S | O | P | Q | R | S |
| 1 | 0 | 0 | -0.447 | 0.447 | -0.125 | 0 | 0 | 0 | 0 | 0 |
| 3 | -0.511 | -0.127 | 0.234 | 0.319 | -0.213 | 0.914 | -1.371 | 0.914 | -0.305 | 0.042 |
| 5 | -0.426 | 0.000 | 0.287 | 0.270 | -0.245 | 0.408 | -0.952 | 0.879 | -0.377 | 0.063 |
| 8 | -0.383 | 0.064 | 0.301 | 0.235 | -0.269 | 0.271 | -0.783 | 0.866 | -0.433 | 0.082 |
| 20 | -0.344 | 0.123 | 0.317 | 0.193 | -0.297 | 0.184 | -0.647 | 0.858 | -0.507 | 0.113 |

Table 4.2: Sensitivities to the normalized second and fourth-order moments of the ground state distribution for all possible rotational branches of the I $^1\Pi_g \leftarrow$ X $^1\Sigma_g^+$ two-photon transition.

R branches connect to $\Pi^-$. Of these two possible upper electronic states, the $\Pi^-$ is expected to show the least amount of perturbation from nearby electronic states according to the well-known selection rules $\Delta J = 0$, $\Delta S = 0$, $\Delta\Lambda = 0$ and $+ \not\leftrightarrow -$ [238, 239]. Therefore, P and R branches should be more reliable for the extraction of polarization data. Some of the features in the spectrum remain to be assigned and await a more detailed characterization of these highly excited electronic states. For now we are partially limited by the inability of the ion gauge to produce a large amount of rotational excitation. This problem could be circumvented by the use of alternative sources of "hot" hydrogen molecules as, for example, microwave/arc discharges or chemical reaction.

Finally, we have listed in Table 4.2 the sensitivities to the second and fourth-order moments of the ground state distribution for all five branches of the I $^1\Pi_g \leftarrow$ X $^1\Sigma_g^+$ two-photon transition. Comparison with the Q-branch sensitivities of Table 4.1 shows an increase in the sensitivity by an order of magnitude. Furthermore, the presence of several rotational branches allows for the measurement of a larger number of anisotropy parameters with a single experimental geometry.

# Chapter 5

# Time-of-Flight Calibration

*The greatest obstacle to discovering the shape of the Earth, the continents and the ocean, was not ignorance, but the illusion of knowledge.*

*D. Boorstin, "The Discoveries"*

## 5.1 Core-Extracted Signal Analysis

The goal of core extraction is to obtain the velocity distribution along the time-of-flight axis by rejecting ions with any off-axis speed components. In practice, this task is achieved by placing a conical mask of a given radius at the end of the time-of-flight tube and before the ion detector (see Fig. 3.5). In the limit of ideal core extraction, a single speed component along the measurement axis is given by two delta functions, corresponding to those ions travelling toward and away from the detector at the time of ionization. Our Wiley-McLaren time-of-flight spectrometer ensures that these two peaks are equally spaced in the time-of-flight profile with respect to the arrival of a static sample. In practice, ideal core extraction cannot be realized because of the finite size of the core extractor necessary to attain reasonable signal levels. Thus, we need a compromise between these two factors and, therefore, we must characterize the instrument function with known velocity distributions over a wide range of operating conditions. A calibration gives us the ability to generate a faithful representation of the single-speed basis functions necessary to convert the measured laboratory speed distribution into a center-of-mass angular distribution.

A Monte Carlo simulation [240] of an ion packet propagated through the instrument generates the single-speed basis functions. The input to the simulation includes the speed of the ion packet, its spatial anisotropy, the orientation of the laser polarization with respect to the time-of-flight axis, the instrument voltage settings, the linewidth of the probe laser (assumed to be at the center of the resonance), and two parameterized blurring functions that account for the resolution of the instrument.

Several factors affect resolution in a core-extracted time-of-flight profile. The first and most obvious one is the finite duration of the probe laser pulse, which in our case blurs the time zero in the time-of-flight profile by 4-5 ns. In addition, the core extractor has a finite size causing some ions with a non-maximal speed component along the time-of-flight axis to be detected. Other blurring effects may include imperfections in the instrument and lack of control over the initial conditions such as the thermal spread of the reagents that lead to reaction product. We have chosen, in the same spirit as Simpson et al. [121, 241], to parameterize the instrument blurring by using two arbitrary functional forms that attempt to account for all the factors affecting resolution along the longitudinal and tranverse directions with respect to the time-of-flight axis. Longitudinal blurring has been modeled with a gaussian functional form. Transverse blurring is accounted for by calculating the transmission of an ion through a core extractor subjected to an exponentially decaying transmission probability at each point across the core extractor area. The validity of these parameterizations is only guaranteed if they are capable of modeling satisfactorily single-speed distributions. In the following sections we will present the results of studying both photodissociation and chemical reactions that yield single-speed molecular populations.

With knowledge of the instrument function, we can construct a “basis set” spanning the entire velocity range pertinent to the problem. In general, a time-of-flight profile $S(t)$ is taken to be a linear combination of single-speed basis functions $B_i(t)$

as shown below

$$S(t) = \sum_{i=1}^{N} c_i \cdot B_i(t) \tag{5.1}$$

where the maximum number of basis functions N is given by the speed resolution of the instrument, which varies depending on the extraction conditions. At this point the problem is reduced to finding the coefficients $c_i$ of this expansion via a least-squares fitting procedure [242]. Throughout this work we have used two different fitting approaches: singular-value decomposition [243] and simulated annealing [244] combined with a maximum entropy algorithm [117, 121, 245]. Both approaches generally yield very similar results, provided that the signals are not subjected to excessive noise and the covariance between basis functions is sufficiently small, i.e., the core-extracted basis functions are reasonably close to the limit of being an orthonormal set.

Finally, to obtain the differential cross section we need to convert the coefficients of Eq. (5.1), which describe the contributions of each laboratory speed to the signal, into the corresponding angular coefficients. The Jacobian of the transformation between the laboratory speed distribution $P(v_{AB})$ and the angular distribution $P(\cos\theta_r)$ is given by (cf. Eq. (2.6))

$$P(\cos\theta_r) = 2\pi \cdot \left(\frac{1}{\sigma}\frac{\partial\sigma}{\partial\Omega_r}\right) = \left(\frac{u \cdot u_{AB}}{v_{AB}}\right) \cdot P(v_{AB}) \tag{5.2}$$

## 5.2 HBr Photodissociation

One-photon photolysis of the hydrogen bromide molecule by UV radiation generates monoenergetic fast and slow H atoms correlating with $Br^2\ P_{3/2}$ and $Br^2\ P_{1/2}$ respectively [246, 247]. The slow H-atom branching fraction and anisotropy parameters for each product channel are wavelength-dependent and have been measured for the HBr molecule at 193 nm by Xu, Koplitz, and Wittig [248], at 243 nm by Kinugawa and Arikawa [249], and more recently by Regan et al. [250] over the 201-253 nm wavelength range.

We have carried out experiments to measure the core-extracted HBr velocity distributions at 243 and 217 nm. Detection of the hydrogen atom was achieved by the use to the familiar (2+1) REMPI scheme of hydrogen via the 2s $^2S_{1/2} \leftarrow$ 1s $^2S_{1/2}$ transition [251]. Figure 5.1 shows a representative core-extracted profile from photolysis at 243 nm, using the same laser to photolyze the HBr parent molecule and detect the H photofragment. Most of the undulations in the signal occur after the main ion peaks. They arise from ringing of the microchannel plate detector when subjected to relatively large ion signals. This spurious, and sometimes detrimental, signal distortions can be removed if we count, instead of integrate, the ion signal. In the former case, each individual ion count may cause considerable detector ringing but it is merely counted, i.e., we add a "one" to the temporal bin where the count happened, by judiciously choosing appropriate trigger and stop voltage levels. This figure shows the time-of-flight profiles for two different laser polarization geometries. The solid lines are fits to the experimental data using the procedures described in Section 5.1. Note that the lower trace contains additional signal coming from the faster channel even though the photolysis anisotropy is expected to be maximal. This additional leakage is caused by the finite radius of our core extractor, which naturally translates into imperfect or incomplete core extraction of the signal. Details about these particular features of the core-extracted profiles will be given in connection to our studies of the photodissociation of molecular oxygen in the next section. Nevertheless, from Fig. 5.1, the presence of a perpendicular and a parallel H-atom channel is quite clear, the faster one approaching the limit of $\beta_{\text{phot}} = -1$ and the slower one corresponding to $\beta_{\text{phot}} = +2$. Similar data has been also obtained at 217 nm using an independent photolysis source to carry out the photodissociation step.

Table 5.1 summarizes the results of the fits for signals collected at various extraction voltages. Varying the extraction voltage is equivalent to changing the size of the ion packet being imaged onto the detector. The trends found in the longitudinal and transverse blurrings in this work are similar to those found for the $Cl_2$ photodissociation experiments carried out in this laboratory on a similar instrument [241]. There is a slight absolute increase in the longitudinal and transverse widths as the extraction is diminished, i.e., as the ion packet has more time to expand in the time-of-flight

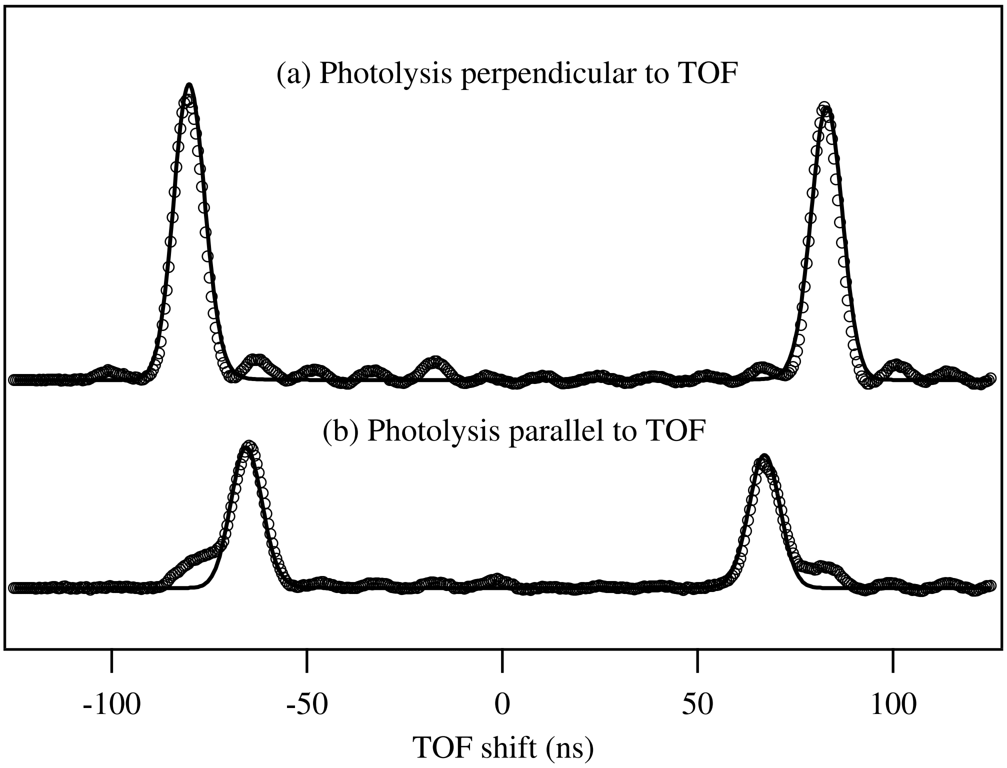


Figure 5.1: Core-extracted H-atom time-of-flight profiles from the photodissociation of HBr at 243 nm at two photolysis polarization geometries. The upper trace corresponds to the fast channel, correlating with ground state Br atoms and with an anisotropy of $\beta = -1$. The lower trace corresponds to the slow photolysis channel with $\beta = +2$. The solid lines are fits to the experimental profiles using the instrumental parameters given in the first row of Table 5.1 (50 V extraction voltage).

region. Nonetheless, a decrease in the extraction voltage enhances the speed resolution of the instrument. The speed resolution quoted on the last column of Table 5.1 corresponds to a mass-to-charge ratio of unity. This resolution needs to be divided by the mass of the ion being detected in order to determine the speed resolution of ions of a different mass under the same time-of-flight conditions. The temporal spread of the H-atom ion signals corresponds roughly to the temporal spread expected for typical HD(v′, J′) products from the hydrogen exchange reaction. This relation holds because the change on the arrival time corresponding to a given initial speed along the detection axis scales linearly with mass, and the speed of the H-atom reagent is

| Extraction Voltage (V) | Longitudinal Resolution (ns) | Transverse Resolution (mm) | Velocity Resolution for m/e = 1 (m/s) |
|---|---|---|---|
| 50 | 9 | 3 | 1700 |
| 100 | 7 | 2 | 2100 |
| 200 | 5.5 | 1 | 4200 |

Table 5.1: Time-of-flight instrumental function parameters obtained from the photodissociation of HBr at 243 nm.

at least three times larger than that of the expected $\mathrm{HD(v', J')}$ product. Moreover, the values shown in Table 5.1 can equally apply to any mass of interest to us provided we first determine, for a given laboratory speed and mass, the spatial size of the ion packet at the time of core extraction.

From the measurements exemplified by Figure 5.1 and also given in Table 5.1 we determined a slow channel branching fraction of $0.16 \pm 0.02$ at 243 nm. This value is in agreement, within experimental uncertainties, with the value of $0.17 \pm 0.02$ most recently reported by Regan et al. [250]. Table 5.2 summarizes the results of the photodissociation studies carried out at 217 and 243 nm. Within our experimental uncertainty, the branching fraction is the same at both wavelengths, also in agreement with the results of Regan et al. [250] who have performed a more systematic study of HBr photolysis over a wide range of photodissociation energies. Examination of the slow channel time-of-flight profile at 217 nm also suggests a deviation of the anisotropy parameter from the maximal value of +2 found at 243 nm. If we take the calibration parameters obtained from the results of the photodissociation of HBr at 243 nm, we find that the best fit to the data at 217 nm is obtained with a $\beta_{\mathrm{slow}} = +1.4 - 1.6$, also in agreement with the work of Xu, Koplitz, and Wittig [248] and Regan et al. [250], whose results show a clear dependence of the anisotropy of the slow product channel over the 193-250 nm wavelength range.

It should be noted that the HBr branching fraction is at least a factor of two smaller than that found for the HI molecule at similar frequencies, thus making HBr

| Photolysis wav. (nm) | $v_{fast}$ (km/s) | $v_{slow}$ (km/s) | $\beta_{fast}$ | $\beta_{slow}$ | Branching fraction $Br^*/(Br + Br^*)$ |
|---|---|---|---|---|---|
| 243 | 16.0 | 13.0 | -1 | +2 | $0.16 \pm 0.02$ |
| 217 | 19.3 | 16.9 | -1 | +1.4-1.6 | $0.14 \pm 0.03$ |

Table 5.2: HBr photodissociation results at 217 and 243 nm.

a cleaner source of fast H atoms. This behavior is advantageous in those cases in which a given HD rovibrational state can be populated by both photolysis channels. The combination of a low yield of H atoms, a smaller rate constant for reaction, and possibly an experimental geometry favoring product detection arising solely from the fast channel can reduce considerably the contribution from the slow H-atom channel to the total detected signal. This point will be further discussed in later sections where one-laser experiments are described in more detail.

## 5.3 $O_2$ Photodissociation

The photodissociation of the oxygen molecule upon irradiation by ultraviolet light from 157 nm to the dissociation threshold at 240 nm has been studied by several groups using Doppler spectroscopy [252–254], translational ion spectroscopy [255], and ion imaging techniques [256–258]. The breaking of the O-O bond is a complicated process involving several excited potential energy curves of different symmetry. Both the multiplet branching ratios and the photofragment spatial anisotropy as a function of photolysis frequency have been used as effective probes of the nature of the photodissociation process.

In this section we use the knowledge already accumulated in the literature for this particular phenomenon to extend our time-of-flight instrument calibration procedures. From these studies it is possible to test our ability to measure the following: (1) total ion signals into a particular quantum state by measurement of the oxygen

| J″ | J′ | Transition frequency $cm^{-1}$ | Line Strength $10^{-36}$ $cm^4$ |
|---|---|---|---|
| 2 | 2 | 88630.8 | 13.2 |
| 2 | 1 | 88630.3 | 3.63 |
| 2 | 0 | 88631.0 | 1.87 |
| 1 | 2 | 88472.4 | 6.98 |
| 1 | 1 | 88471.8 | 11.7 |
| 1 | 0 | 88472.5 | 0.0 |
| 0 | 2 | 88404.4 | 9.01 |
| 0 | 1 | 88400.9 | 0.0 |
| 0 | 0 | 88404.5 | 9.69 |

Table 5.3: Transition frequencies and two-photon line strengths for the oxygen atom (2+1) REMPI scheme ca. 226 nm.

multiplet branching ratio; (2) the spatial anisotropy of the oxygen-atom photofragment (with and without the core extractor) for a particular spin-orbit state; (3) the ratio between ion signals with and without the core extractor which, as explained below, is an independent measurement of the quality of our instrument function parameterizations.

The presence of a convenient (2+1) REMPI scheme ca. 226 nm for oxygen-atom detection make these experiments particularly convenient for our purposes, since at least at one frequency we can use the same laser pulse to photolyze and detect the atomic fragment. Bamford and co-workers [259] have measured using a high-resolution, continuous-wave laser the two-photon line strengths for the three 3p $^3P_{J'} \leftarrow$ 2p $^3P_{J''}$ transitions used in our experiments. For reference purposes we list in Table 5.3 the transition energies and relative two-photon cross sections. Note that the resolution of our laser, which amounts to at least 0.25 $cm^{-1}$ in the dye fundamental, precludes us from resolving the fine-structure of the excited state multiplet for all three ground state J″ levels of the oxygen atom. Therefore, all the transitions originating from a given 2p $^3P_{J''}$ state need to be considered in the comparison of ion signals for different spin-orbit states.

Table 5.4 shows a comparison of the multiplet branching ratios we have observed from the one-photon photolysis of oxygen ca. 226 nm. As in the HBr experiments described in the previous section, we expanded the $O_2$ sample into the vacuum chamber to reduce the averaging produced by both the rotational structure and translational temperature present in a room-temperature molecular sample. The branching ratios we report in this table have been corrected for both power changes with laser wavelength and the line strengths for the two-photon transition given in Table 5.3. The errors quoted in these measurements arise mostly from our inability to maintain the experimental conditions perfectly constant during the wavelength scan. Comparison with previous work, as shown in the same table in columns 2 and 3, is very good. All three independent measurements agree within the experimental uncertainties. The ability to perform these measurements reliably indicates that our instrument can also be used to record internal energy distributions by scanning the probe laser in frequency. This remains true as long as we make sure that the ion collection efficiency can be made independent of the velocity or anisotropy of the species probed, i.e., the extraction voltages can be increased to minimize the spatial spread of the ion packet as it travels toward the detector. A simple calculation involving the speed of the species of interest and the total flight time can provide a conservative upper bound for the spatial size of the ion packet as it is imaged onto the detector. This estimate can be used to tailor the extraction voltages in such a manner that there is no velocity discrimination for the range of speeds of interest.

In Fig. 5.2 we show time-of-flight profiles for oxygen 2p $^3P_2$ for two different photolysis-TOF geometries and under different core-extraction conditions. The present experimental setup allows us to change the size of the core extractor from a 3 mm to a 1 mm radius in situ. These are shown in Figs. 5.2b and 5.2c. In addition we have recorded time-of-flight profiles without the core extractor, as shown in Fig. 5.2a. The solid lines are fits to the experimental profiles using single-speed basis functions accounting for the different core-extraction conditions. The progression from no core extraction (panel a) to complete core extraction (panel c) is very clear.

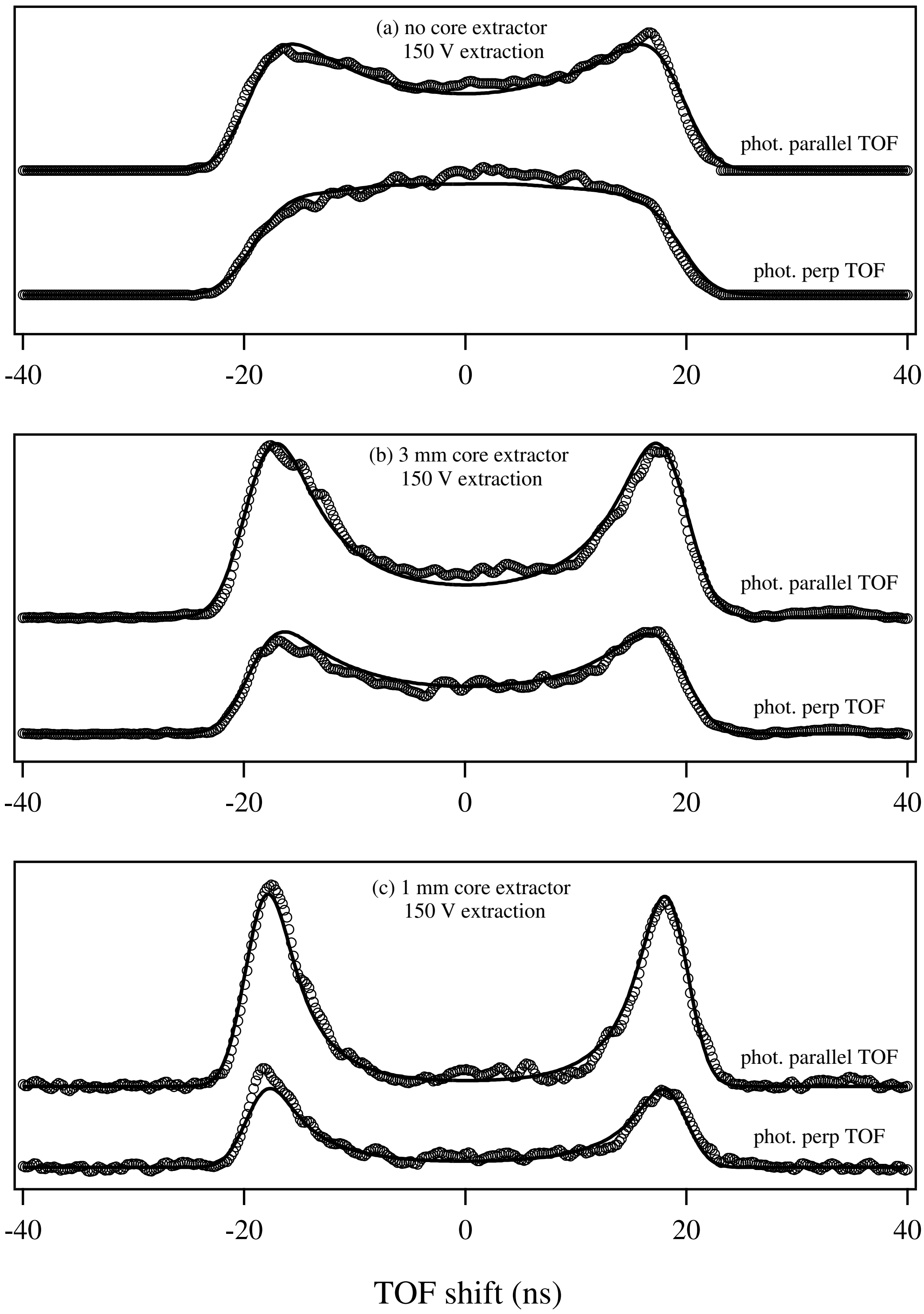


Figure 5.2: Time-of-flight profiles under different experimental conditions for the oxygen 2p $^3P_2$ state arising from the photodissociation of the $O_2$ molecule at 226 nm. See text for further details.

| 2p $^3P_{J''}$ | This work | Buijsee et al. Ref. [258] | Tonokura et al. Ref. [254] |
|---|---|---|---|
| 0 | $1.00 \pm 0.15$ | $1.00 \pm 0.26$ | $1.00 \pm 0.11$ |
| 1 | $3.14 \pm 0.37$ | $3.33 \pm 0.43$ | 3.84 |
| 2 | $9.07 \pm 0.92$ | $9.00 \pm 0.70$ | $9.61 \pm 1.15$ |

Table 5.4: Multiplet branching ratios for the photodissociation of the oxygen molecule at 226 nm. Error bars indicate one standard deviation.

Moreover, the two geometries recorded for each case and shown in this figure allow us to obtain three independent measurements of the anisotropy parameter for this particular photodissociation channel. These measurements, if combined, yield $\beta = 0.55 \pm 0.15$. This value can be readily checked to be reasonable by visual inspection of the figure since the ratio of intensities between the parallel and perpendicular geometries at the rising and falling edges of the time-of-flight profiles is proportional to the photofragment angular anisotropy. This value compares favorably with $\beta = 0.61 \pm 0.09$ reported by Buijsse et al. [258] but is considerably lower than the value of $\beta = 1.6$ of Tonokura et al. [254]. The origin of this discrepancy can be attributed to the inability of Tonokura et al. to perform a direct inversion of their Doppler profiles. The value of $\beta = 1.6$ was obtained by forward convolution of a known anisotropic distribution into a one-dimensional Doppler profile and, therefore, this result should be viewed with caution. On the other hand, Buijsse et al. have directly measured the angular distribution using the photofragment ion imaging technique. Their lower error bars are most likely a consequence of having the ability to obtain a larger number of experimental points in their ion image data and, thus, reduce the statistical error in their measurements. Nevertheless, the agreement between our measurements and those of Buijsse et al. is quite satisfactory. We should note, however, that the error bar of $\pm 0.15$ in our measurements can be regarded as representative for our instrument given the fact that sources of blurring are difficult to assess and quantify to a degree we could distinguish small changes in the spatial

| Core Extractor Radius (mm) | Experimental Ratio | Simulated Ratio |
|---|---|---|
| $\infty$ | 1.000 | 1.000 |
| 3 | 0.239 | 0.213 |
| 1 | 0.024 | 0.025 |

Table 5.5: Experimental and simulated total signal ratios for the time-of-flight profiles of Fig. 5.2.

distribution of velocities.

As an additional check of the validity of our calibration procedures we show in Table 5.5 a comparison between experiment and our Monte Carlo simulation output for the ratio of ion signals expected with and without the core extractors in place. The simulations of the time-of-flight profiles were performed by using the instrumental parameters used in Fig. 5.2 without any further adjustments. In the limit of an "ideal" core extractor, these numbers should reflect the value of the non-core-extracted signal at the edges of the non-core-extracted profile. However, instrumental blurrings wash out this ideal relationship and bring these figures down to lower values. As evidenced by a comparison between columns two and three, the Monte Carlo simulation is capable of reproducing experimental ion intensity ratios over almost two signal decades. This blind match between experiment and the modelling of the instrument is very encouraging.

Finally, we show in Fig. 5.3 core-extracted profiles at a lower extraction voltage. These measurements were necessary in order to obtain a more detailed map of the variation of instrumental parameters with time-of-flight conditions. The first thing to note from these data is the drastic reduction in signal as a consequence of a longer residence time of the ions in the time-of-flight apparatus, which in this case amounts to almost a factor of two with respect to Fig. 5.2. A summary of the blurring parameters at these two extraction voltages and for different core extractor radii is given in Table 5.6. Both the numbers given in this table and those compiled for the

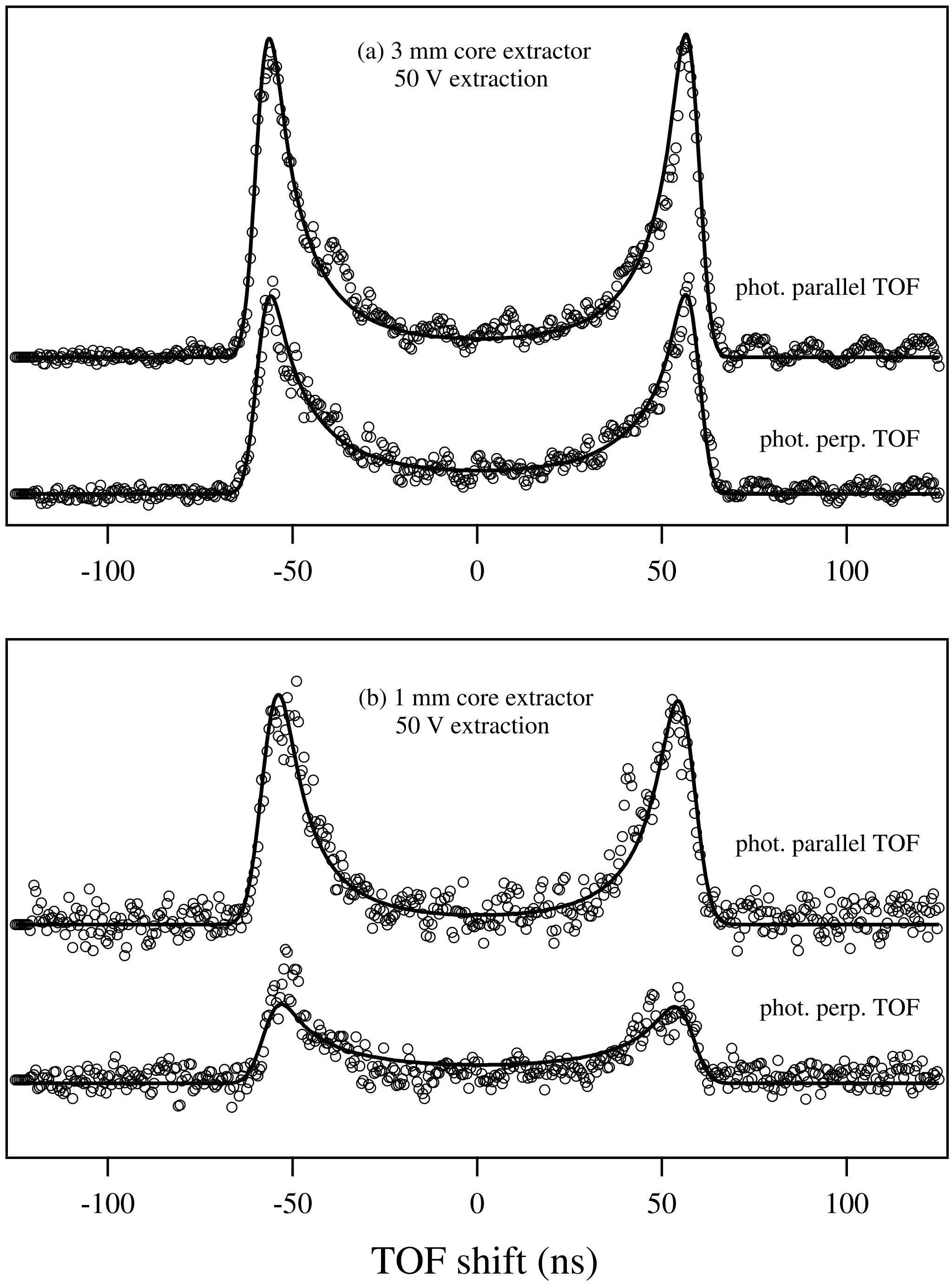


Figure 5.3: Time-of-flight profiles under different experimental conditions for the 2p $^3P_2$ fragment arising from the photodissociation of the $O_2$ molecule at 226 nm. The extraction voltage has been brought down by a factor of three with respect to what is shown in Fig. 5.2.

| Core Extractor Radius (mm) | Extraction Voltage (V) | Longitudinal Resolution (ns) | Transverse Resolution (mm) |
|---|---|---|---|
| 3 | 100 | 7 | 4 |
| | 300 | 4.5 | 2 |
| 1 | 100 | 7 | 3 |
| | 300 | 4.5 | 1 |

Table 5.6: Instrumental blurring parameters derived at various extraction voltages and core extraction conditions.

HBr photolysis show the same overall trends with extraction voltage, i.e., the velocity resolution is enhanced as the extraction voltage is lowered. In this particular case, the decrease in core-extractor radius does not seem to affect the velocity resolution as much as the extraction voltage. On the contrary, inspection of the time-of-flight profiles of Fig. 5.3 suggests that core-extraction hurts the overall quality of the signal as opposed to enhancing the velocity resolution. In this particular case, it is difficult to judge whether it is better, for practical purposes, to sacrifice resolution for the sake of signal-to-noise ratio. This weak dependence of the velocity resolution on core-extractor radius can be attributed to the fact that for a such small core extractor radii other instrumental effects such as, for example, laser pulse width, energy spread, and imperfections in the apparatus, start dominating the profile lineshape. Such an unexpected result would not have been possible to detect without the extensive calibrations of the instrument that we have carried out.

## 5.4 $\mathbf{H_2(v', J')}$ from the H + HBr reaction

Both the H + HI and the H + HBr reactions are known to produce $H_2$ molecules with a large amount of vibrational and rotational excitation. This property has been exploted by Heck et al. [203] to perform the spectroscopy on the E,F $^1\Sigma_g^+ \leftarrow$ X $^1\Sigma_g^+$ transition of $D_2$ for high rotational and vibrational quantum numbers arising from the

D + DI reaction. Similarly, Kliner et al. [260, 261] have studied the H + HI reaction in this laboratory prior to the measurement of integral cross sections for the hydrogen exchange reaction. In our particular case, the H + HBr reaction is useful because the kinematics of this reaction allow it to be used as a prototype of a chemical reaction resulting in a single laboratory single-speed distribution.

Chemical reactions studied by the photoloc technique have, in general, uncertainties associated with thermal motion between reagents. These uncertainties translate into a collision energy spread which is dependent on the gas temperature. For this reason, we choose carry out experiments in a free-jet expansion. The estimation of these uncertainties will be discussed in the next chapter. Suffice it to say, however, that these effects can translate into additional blurrings in the instrument function that may not be present in the photolysis studies previously discussed. For this reason, we decided to examine the $H_2$ product from the H + HBr reaction to ensure that the calibration parameters obtained from the HBr photodissociation studies could be used reliably for the continuous distribution of laboratory speeds that characterize the HD product from the H + $D_2$ reaction.

Figure 5.4 shows the velocity distribution of the $H_2(v' = 4, J' = 1)$ product at a collision energy of 1.9 eV (photolysis wavelength of 217 nm). For this particular $H_2$ product state, there is a possibility of both photolysis channels leading to this rovibrational level. As the core-extracted time-of-flight profiles in Fig. 5.4 show, however, we only find evidence for one speed, that belonging to the fast photodissociation channel. All three time-of-flight profiles are satisfactorily fit by a product speed of ca. 9000 m/s, as expected from the reaction kinematics and energetics. Furthermore, the instrumental function parameters are very similar to those of the HBr photolysis studied at the same voltage conditions. In general, we have found that the reactive product tends to require a slightly larger transverse blurring parameter caused by factors not present in simple photolysis experiments.

The core-extracted time-of-flight profiles shown in Fig. 5.4 have been measured at two different photolysis-probe geometries. The anisotropy of this velocity distribution is zero, i.e., the profile intensity and shape is independent of laser polarization. This measurement therefore implies a vanishing second-order moment of the angular

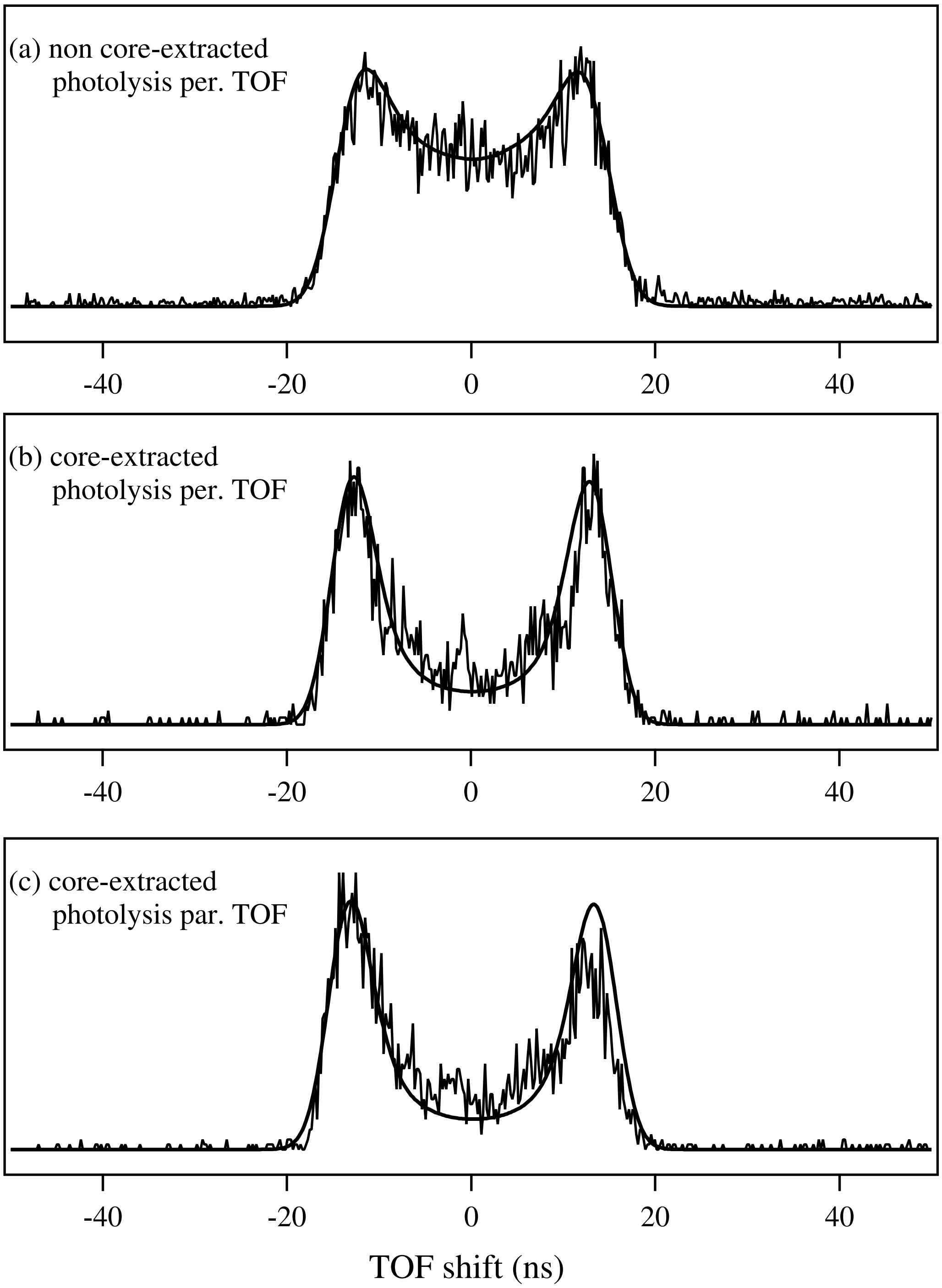


Figure 5.4: Time-of-flight profiles of the $H_2(v' = 4, J' = 1)$ product from the H+HBr reaction at a collision energy of 1.9 eV. The $H_2$ product displays a single laboratory speed ca. 9000 m/s. Solid lines are fits to the experimental profiles using a single-speed basis function.

distribution, that is, $< P_2(\cos\theta_r) >= 0$. While the kinematics of this reaction prevent us from obtaining complete angular information, this result implies that the $H_2$ product is not exclusively back-scattered or forward-scattered. If this were the case, the anisotropy inferred from the polarization measurements would approach the photolysis anisotropy, in this case $\beta = -1$. This result is consistent with the experimental work and semiclassical calculations on the $H + HX$ reaction family by Valentini and co-workers [262–265].

In addition, the non-core-extracted profile shown in Fig. 5.4 contains additional information regarding the Doppler selectivity of the probe laser. For a $\beta = 0$ velocity distribution, this profile should not display a minimum in the center. Rather, it should be flat. The dip in the profile arises from the Doppler selection of the probe laser, which discriminates against those ions with large speed projections along the laser axis. A lorentzian lineshape with a FWHM of 2000 m/s was necessary to properly fit the non-core-extracted signal satisfactorily. This Doppler selectivity agrees closely with previous measurements of the laser linewidth which include: (1) measurement of the fundamental laser linewidth with an etalon, (2) deconvolution of peak lineshapes [266] arising from $H_2$, $D_2$, and HD (2+1) REMPI resonances, and (3) peak lineshape analysis of the Kr (2+1) REMPI resonance at 222.6 nm [267], in which the effect of Doppler broadening can be neglected owing to the large mass of this atom.

# Chapter 6

# Characterization of Reaction Conditions

*Reason's last step is the recognition that there are an infinite number of things which are beyond it.*

*B. Pascal, "Pensees"*

## 6.1 General Considerations

Paramount to the use of the photoloc technique is the experimental realization of the assumptions presented in Section 2.1. It is necessary, for example, to have a knowledge of the initial internal energy distributions of the reagents in order to evaluate all possible sources resulting in a degradation of resolution. Furthermore, a close comparison with theory requires that we know the collision energy resolution of the experiment as well as the number of rotational levels populated in the diatomic reagent. For this purpose, we have carried out an extensive characterization of the HBr and $D_2$ rotational and translational distributions under the experimental conditions used for the $H + D_2$ reactive scattering experiments.

In an attempt to optimize the reaction conditions we have measured these distributions at several nozzle delays, stagnation pressures, and distances of the nozzle from the photolysis-probe region in the time-of-flight apparatus. The results described below correspond to the best overall conditions that are compatible with reasonable signal levels. In general, we have found that the optimum time to probe for reactive product is located near the front of the free-jet expansion. This is about 150-200 $\mu$s after the first appearance of ion signal from either reagent for a typical gas pulse of 500-600 $\mu$s. Probing the temporal center of the nozzle expansion, where the largest signal levels are expected, tends to produce distortions in the time-of-flight profiles. We attribute this behavior to ion-neutral collisions as the ions are extracted into the free-drift region and/or the formation of clusters in the beam. In spite the low stagnation pressures used, usually 300 Torr or less, the latter is possible owing to the large dipole moment of the hydrogen halide photolytic precursor. In the following sections we discuss these and other issues in more detail.

## 6.2 Single-Collision Conditions and Product Yield

In our reactive experiments we have to ensure we are in such a regime that products are detected under single-collision conditions. Since measurements are carried out in a single molecular beam expansion there is a possibility for too high number densities of the reagents leading to secondary collisions and thermalization of the reaction product prior to its detection.

Experimentally, there are several ways of ensuring single-collision conditions. One of them is to simply record the data as a function of expansion stagnation pressure and ensure that the time-of-flight profiles do not change as the number densities in the beam are lowered. Even though we carry out these experimental checks, it is also useful to have a rough idea of the mean free paths and reagent number densities typical of our experiments.

In Figure 6.1 we show a D-atom time-of-flight profile using a 1:10 HI : $D_2$ mixture and a photolysis-probe laser arrangement. Photolysis of HI is effected at 210 nm giving a collision energy of 2.25 eV. D-atom detection is accomplished via the 3s $^2$S,

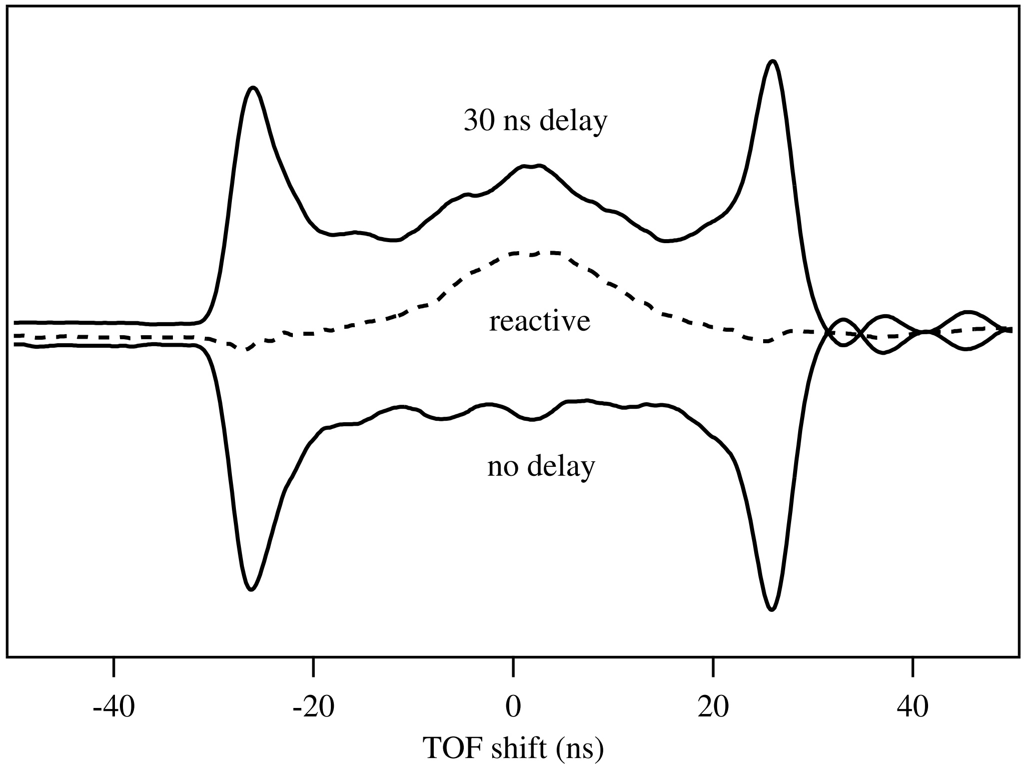


Figure 6.1: Time-of-flight spectrum showing D-atom signal arising from DI photolysis (impurity) and chemical reaction.

3pd $^2$D $\leftarrow$ 1s $^2$S (2+1) REMPI transition circa 205 nm [268, 269]. The ion signal was collected at two photolysis-probe delays, the difference between the late and early profiles being solely due to reactive product from the $H + D_2$ reaction building up during this period of time. The two sharp peaks correspond to the photodissociation of the DI impurity in our sample. This impurity arises from the natural abundance of the deuterated isotope in the HI cylinder, the isotopic ratio being 1/6665.7 [270]. The peak in the middle of the time-of-flight profile corresponds to reactive product. Since we have the ability to measure the relative D-atom populations from both the photolysis of DI and from the $H + D_2$ reaction, we can arrive at a reliable estimate of the number densities in the region of the expansion where we generally look for reaction products.

The product number density per unit time arising from the reaction is given by

$$\frac{\Delta N_D}{\Delta t} = \sigma_{rxn} v_{rel} N_H N_{D_2} \tag{6.1}$$

where $N_D$, $N_H$, and $N_{D_2}$ are the number densities of the products and reagents respectively, $\sigma_{rxn}$ is the reaction cross section, $v_{rel}$ the relative velocity of the collision, and $\Delta$t the time elapsed between laser photolysis and product detection. The number densities of the products and reagents can be related to each other by the following relations

$$\Delta N_D = \alpha N_{D,phot} \tag{6.2}$$

where $\alpha$ is a constant relating the amount of D-atom signal from photolysis and reaction. This constant is obtained from Fig. 6.1 by straightforward integration of the photolysis and product peaks.

$$\Delta N_D = \alpha \beta N_H \tag{6.3}$$

where $\beta$ is the D:H natural isotopic abundance.

$$N_H = \gamma N_{HBr} \tag{6.4}$$

where $\gamma$ is the efficiency of the photodissociation step, i.e. fraction of the HBr molecules photodissociated.

$$N_{HBr} = \delta N_{D_2} \tag{6.5}$$

where $\delta$ is the ratio of HBr to $D_2$ reagent in the expansion which we may assume, if necessary, to be equal to the ratio of pressures in the reaction mixture.

Combining Eqs. (6.1) through (6.5) we can arrive at a value for the number density of $D_2$ molecules in the expansion which is given by

$$N_{D_2} = \frac{\alpha \beta}{\sigma_{rxn} v_{rel} \Delta t} \tag{6.6}$$

We note that Eq. (6.6) is independent of the photolysis efficiency $\gamma$ and the ratio of reagent concentrations $\delta$, figures not easy to measure experimentally. For $\alpha = 0.4$ and

$\sigma_{\rm rxn} = 2$ Å$^2$, the $D_2$ number density is roughly 5x10$^{+12}$ per cm$^3$. The corresponding mean free path is then given by

$$\lambda = \frac{1}{\sigma_{rxn} N_{D_2}} \approx 10\ m \tag{6.7}$$

This estimate of the reagent number densities indicates that our measurements in a single beam are likely not to be affected considerably by secondary reactive collisions. It may be the case, however, that other processes with larger cross sections such as, for example, ion-molecule and ion-ion collisions may complicate the situation once the photolysis or detection steps generate a sufficiently large number of charged species. Methods and checks we have used to avoid these additional complications will be discussed in future sections.

We can use this estimate of the reagent number density to illustrate the difficulties involved in the state-resolved differential cross section measurements we intend to carry out. Taking the "typical" H and $D_2$ number densities to be $\sim$ 5x10$^{+12}$ cm$^{-3}$ we can arrive at the following approximate product yields

total D product (2 Å$^2$):
$\sim$ 5x10$^{+6}$ cm$^{-3}$,

total HD(v$'$, J$'$) product (0.01 Å$^2$):
$\sim$ 30000 cm$^{-3}$,

HD(v$'$, J$'$) in a $5 - 10^{\rm o}$ angular bin:
$\sim$ 2500 cm$^{-3}$ or
$\sim$ 5x10$^{-3}$ in detection volume!!!

A product yield of $\sim$ 5x10$^{-3}$ per angular bin in the laser detection volume implies that an average of 200 laser shots are necessary to detect a *single* product ion. To obtain a reasonable signal-to-noise ratio of, say, 10 we therefore need to collect a total of 100 ions, that is, 20000 laser shots. With our 10-Hz photolysis and probe lasers it takes approximately 30-40 minutes of data collection during which experimental

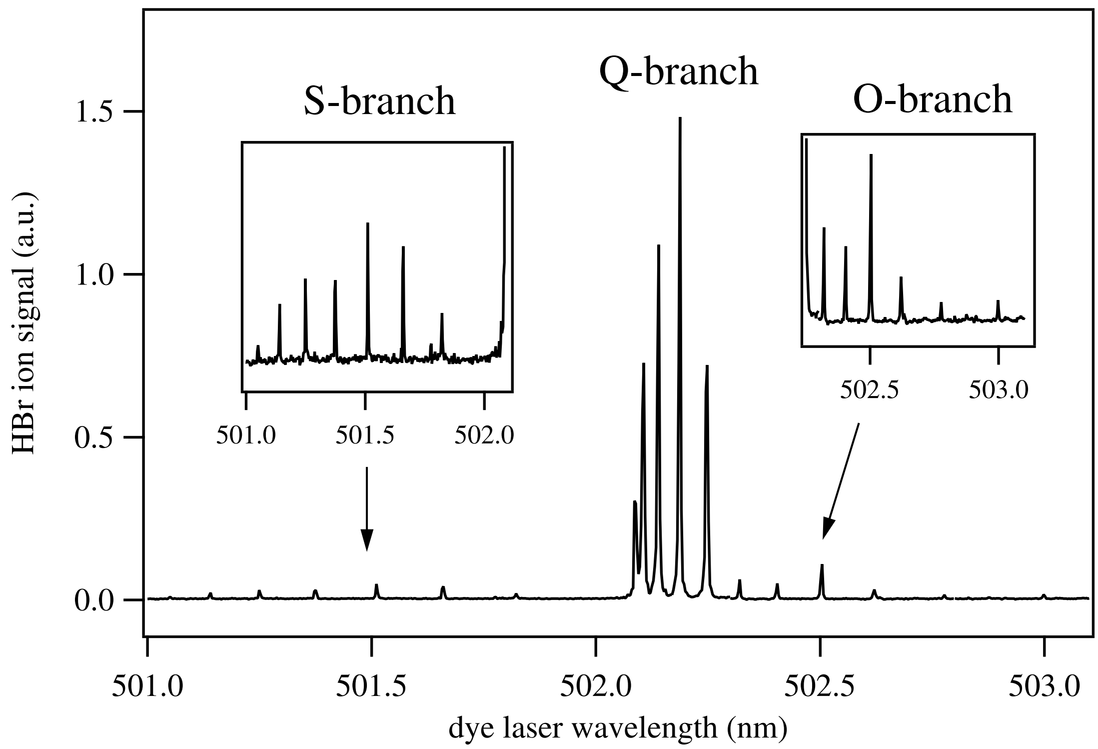


Figure 6.2: (2+1) REMPI spectrum of the H $^1\Sigma_g^+ \leftarrow$ X $^1\Sigma_g^+$ (0,0) band of HBr at room temperature. The spectrum shows O, Q and S-branch progressions.

conditions (i.e., laser powers, pulsed molecular beam performance) must be kept as constant as possible.

## 6.3 Reagent Internal Energy Distributions

Figure 6.2 shows the (2+1) REMPI spectrum of the first members of the O, Q and S branches of the H $^1\Sigma_g^+ \leftarrow$ X $^1\Sigma_g^+$ (0,0) band of the HBr molecule near 250 nm. Callaghan and Gordon [271], and Kvaran, Logadóttir, and Wang [272] have used this REMPI scheme in systematic investigations of the Rydberg states of the HBr molecule. As the spectrum shows, the Q-branch dominates over the other two branches as it is typical in two-photon $\Sigma - \Sigma$ transitions (See discussion in Section 4.2). Q-branch intensities are ten to thirty times stronger than O or S-branch

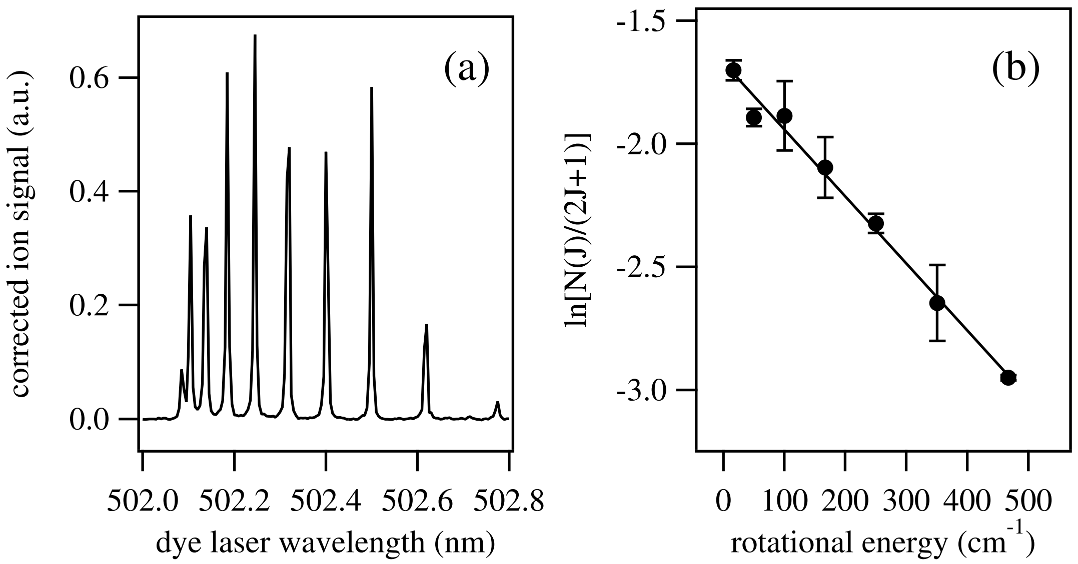


Figure 6.3: (a) (2+1) REMPI spectrum of room-temperature HBr through the Q-branch members of the H $^1\Sigma_g^+ \leftarrow$ X $^1\Sigma_g^+$ (0,0) transition, and (b) Boltzmann plot of the rotational population derived from the analysis of spectral intensities. The rotational temperature is $306 \pm 20$ K

intensities and, therefore, the corresponding rotational line strengths should show a very weak dependence with rotational quantum number. Such is also the case, for example, of two-photon $\Sigma - \Sigma$ transitions in other hydrogen halides like HCl [273–275] and HI [276, 277].

We have calibrated the Q-branch line strength factors by measuring the rotational distribution of a room temperature HBr sample fed into the vacuum chamber. The spectrum and corresponding Boltzmann plot is shown in Figure 6.3. The derived rotational population is $306 \pm 20$ K, confirming the validity of our analysis of the rotational distribution as well as our ability to use this spectroscopic transition as an "HBr thermometer."

Next, we present the measurement of the HBr rotational distribution in the free-jet expansion. The number of rotational levels populated in this case is considerably lower than at room temperature. For the spectrum shown in Figure 6.4a, a temperature of around 80 K can be assigned to the first four states of the rotational distribution

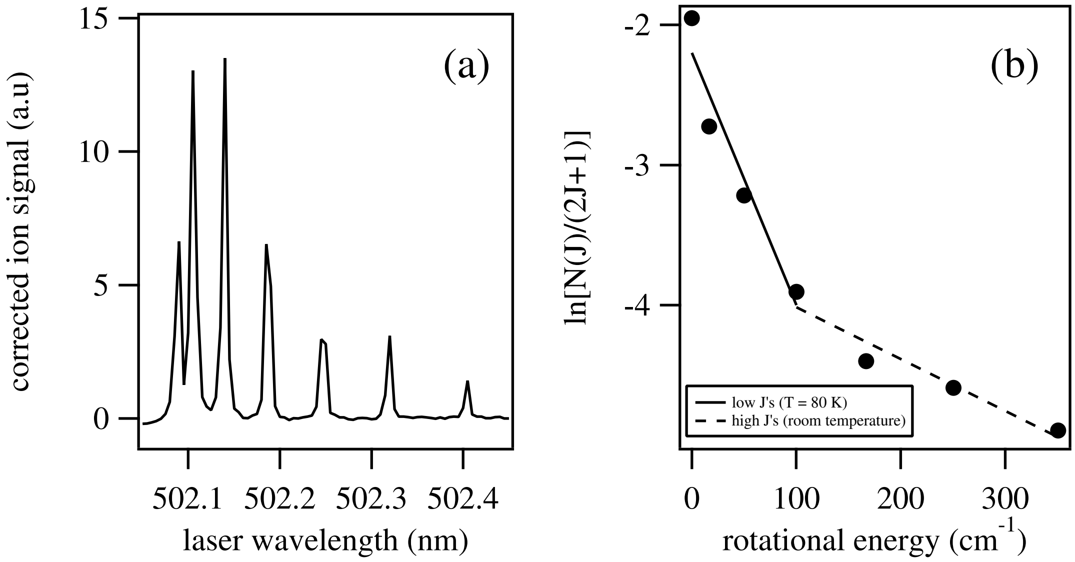


Figure 6.4: (a) (2+1) REMPI spectrum of HBr, and (b) Boltzmann plot of the rotational population in the jet expansion used for the photolysis and reaction studies.

shown in Figure 6.4b, and a room temperature distribution for the higher ones. This initial rotational energy distribution in the photolytic precursor results in a collision energy spread of at most 0.01 eV.

Figure 6.5a shows the (2+1) REMPI spectrum and the corresponding rotational populations for $D_2(v = 0, J)$ from the gas expansion at the same nozzle delay as that for HBr in Figure 6.4. The rotational distribution and line strength factors for $D_2$ were similarly determined from a room-temperature sample as shown in Section 4.2.

In the case of $D_2$, the cooling of the rotational degree of freedom is harder to achieve than for HBr because of the larger rotational constant for this molecule, and because inelastic collisions can only induce odd-to-odd and even-to-even rotational transitions, thereby increasing even further the energy separation between connected rotational energy levels. A multitude of rotational relaxation experiments [278–283] as well as theoretical calculations [284–286] show that typical rotational collision numbers $Z_R$ (the number of collisions its takes to effect a rotational transition) for hydrogen mixtures at temperatures ranging from 70 to 300 K are ca. 200-700, with the notable exception of HD with $Z_R \sim 10 - 30$. Addition of a noble gas tends to

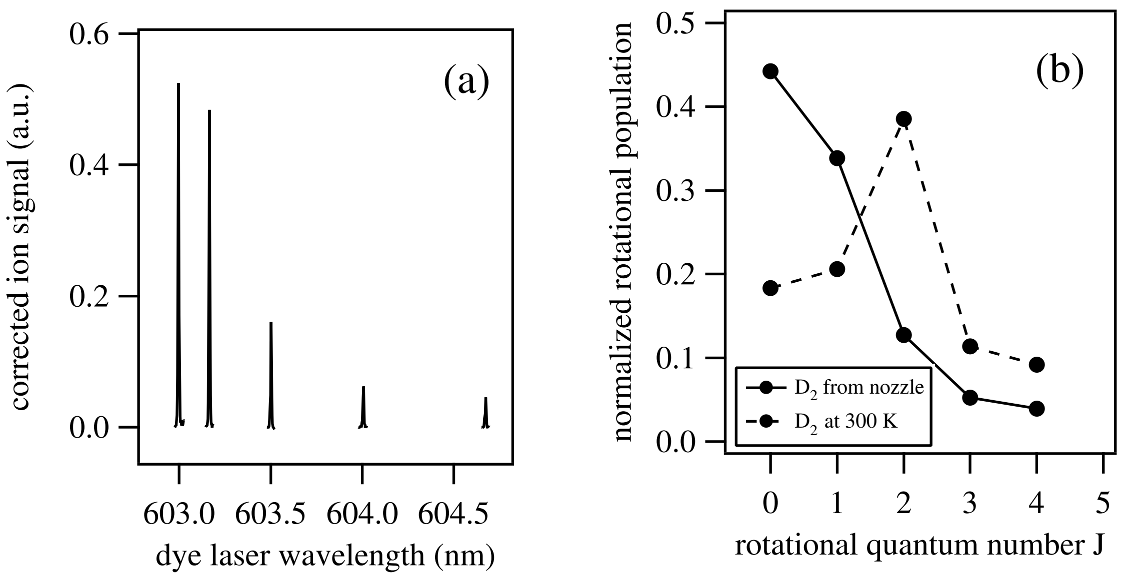


Figure 6.5: (a) (2+1) REMPI spectrum of $D_2$ from the nozzle expansion at the same conditions as those of Fig. 6.4. (b) Comparison of the rotational populations in the beam and at room temperature (taking into account the effect of nuclear spin statistics).

decrease the collision number by at most a factor of ten, argon being the most effective one. These figures compare quite unfavourably with the typical $Z_R < 5$ found in most heavier diatomic gases [287]. As shown in Fig. 6.5b, most of the rotational population in our beam expansion resides in levels 0, 1, and 2 with ratios approximately 0.45:0.35:0.10. A "temperature" of 90 K can be assigned to this distribution, if desired, even though we note that the even and odd levels cannot thermalize with each other during the expansion process. Taking into account this fact, the coldest sample one can ever attain with n-$D_2$ is comprised by a ratio of 0.7:0.30 in $J = 0$ and $J = 1$ respectively, which corresponds to a "temperature" of 65-70 K, limit from which our beam conditions are not too far away from. An alternative way of going beyond the 70 K limit would be to use a source of o-$D_2$ which may be achieved via the exposure of a mixture of n-$D_2$ to a catalyst such as ferric hydroxide or chromic oxide at low temperatures [288–291]. The measured $D_2$ rotational distribution should be taken into account when comparing our experimental results with theoretical predictions.

## 6.4 Collision Energy Spread

The most important source of uncertainty in our experiments comes from the initial thermal motion of the photolytic precursor and $D_2$ reagent. This problem has already been addressed by van der Zande et al. [292, 293], and Aoiz et al. [294] in the context of photoinitiated chemical reactions. The average collision energy in a hot atom experiment is readily calculated and is only slightly affected by the thermal motion of the reagents. However, the width of such a distribution of collision energies depends on both the width of the corresponding velocity distribution and the absolute average velocity. The rigurous expression for the distribution of collision energies after convolution of the thermal distributions is complicated, involving the sum of two gausssians. Let's define the total excess energy in the HX photolysis step as

$$E_{exc} = \left(\frac{m_H m_X}{2m_X}\right) u_H^2 \tag{6.8}$$

where $m_H$ and $m_X$ are the masses of H and X respectively, and $u_H$ is the recoil velocity of H relative to the center of mass of HX. In the limit of

$$E_{exc} \gg \left(\frac{m_{HX}\left(m_H + m_{D_2}\right)}{m_X m_{D_2}}\right) kT \tag{6.9}$$

where T is the initial temperature of the precursor and diatomic reagent, we can write the distribution of collision energies as a gaussian of the form

$$P\left(E_{coll}\right) = Ae^{-B(E_{coll} - CE_{exc})^2} \tag{6.10}$$

where the constants A, B, and C are given by

$$A = \left(\frac{m_{HX}^2\left(m_H + m_{D_2}\right)^2}{4\pi kT E_{exc} m_H m_X m_{D_2}\left(m_H + m_X + m_{D_2}\right)}\right)^{\frac{1}{2}} \tag{6.11}$$

$$B = \left(\frac{m_{HX}^2\left(m_H + m_{D_2}\right)^2}{4kT E_{exc} m_H m_X m_{D_2}\left(m_H + m_X + m_{D_2}\right)}\right) \tag{6.12}$$

$$C = \left(\frac{m_X m_{D_2}}{m_{HX}\left(m_H + m_{D_2}\right)}\right) \tag{6.13}$$

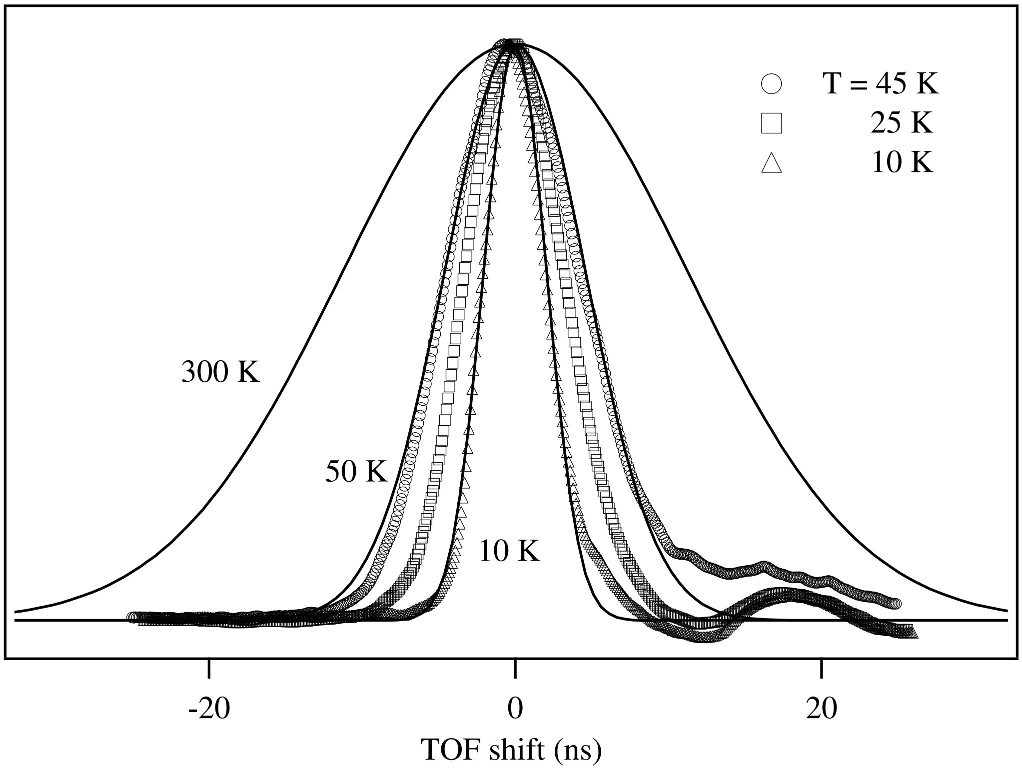


Figure 6.6: HBr time-of-flight profiles at different nozzle delays are represented by symbols. Note the increase in the peak width as the nozzle delay is increased and one moves into the peak of the gas pulse (from diamonds to circles). The solid lines show the expected time-of-flight profiles at 10, 50, and 300 K taking into account the effects of instrumental resolution.

From Eq. (6.10) we see that the spread of collision energies scales as $T^{\frac{1}{2}}$ and that only in the limit of zero translational temperatures the width of this distribution goes to zero. Although we co-expand these two molecules in a vacuum, no guarantee exists that they will reach the limit of zero translational temperature desired to obtain a perfectly defined collision energy, solely dictated by the photolysis step. The rotational distributions already presented in the previous section already provide a conservative upper limit to the translational temperature of circa 80 K, which corresponds to a collision energy resolution of 0.08 eV. This estimate is strictly an upper one only if the rotational degree of freedom cools less efficiently than the translational one, as it is generally the case.

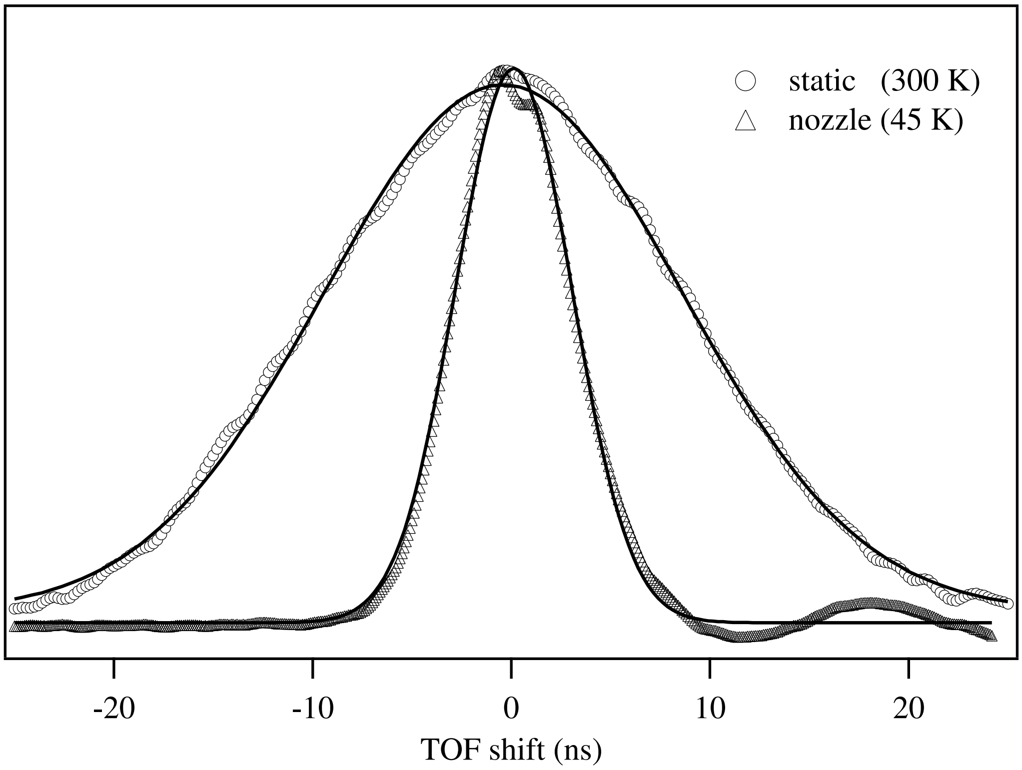


Figure 6.7: Time-of-flight profiles of $D_2$ from the expansion and from a room-temperature sample. From these profiles the beam translational temperature is estimated to be ca. 45 K.

Fortunately, our time-of-flight instrument is capable of providing a better estimate of the translational cooling achieved during the expansion process. We have accomplished this task by comparing the time-of-flight temporal widths of HBr and $D_2$ in the beam and at room temperature. Figure 6.6 shows the time-of-profile of HBr from the expansion at different regions of the nozzle pulse. The different widths in these profiles illustrate the sensitivity of this measurement to the local translational energy spread at different points in the expansion. Figure 6.6 also shows the width of the TOF profile expected from a thermal $H^{79}Br$ sample. The close proximity of $^{79}Br$ and $^{81}Br$ peaks in the time-of-flight profile precuded a direct measurement of the thermal HBr width. The solid lines in Figure 6.6 correspond to fits of these signals taking into account the effects of instrumental resolution. The temperature inferred from these measurements varies from 10 K at the front edge of the nozzle pulse to 45 K at the region where the rotational temperatures were measured. Figure 6.7 shows the $D_2$ time-of-flight profiles at room temperature and at a nozzle delay corresponding to the an HBr translational temperature of 45 K. Within our experimental uncertainty, we find that $D_2$ has the same temperature as the HBr precursor.

From these measurements of the translational temperatures in the beam expansion and by use of Eq. (6.10), we conclude that reagent thermal motion does not contribute more than 40 meV to the spread in collision energy. This spread, combined with the previous value of 10 meV from the rotational energy distribution of the HBr precursor, yields an upper limit to the collision energy resolution of 50 meV FWHM. This value is about a factor of three better than previous experiments in this laboratory using milder expansion conditions [120]. Most recently, Shafer-Ray and co-workers [295] have used a different experimental arrangement to obtain a collision energy resolution of 18 meV (FWHM) for the forward-scattered products ($\theta_{\text{prod}} < 80^{\circ}$). Such a decrease in collision energy is a direct consequence of using both a well-defined and collimated molecular beam with no transverse thermal motion and detecting only the forward-scattered product. In either case, the collision energy resolution currently attainable in photoinitiated experiments in a single molecular beam or free-jet expansion is comparable, if not better, than those attained with the technique of crossed molecular beams.

## 6.5 Reagent Velocity Slip

The disparity between the masses of the HBr and $D_2$ reagents raises another concern, namely, a plausible velocity "slip" between these two species as they co-expand into the vacuum chamber. The presence of this effect would, among other things, complicate the analysis of the velocity distributions and therefore it should be avoided. As McClelland et al. [296], and DePaul, Pullman, and Friedrich [297] have discussed at greater lengths in their studies of supersonic expansions, velocity slip is important when the beam species have not had sufficient time to cool their translational degrees of freedom to the same extent before they reach the "zone of silence" (collisionless regime). In other words, velocity slip arises from differences in the thermal distributions of the coexpanding species.

More quantitatively, the terminal flow velocities reached in a supersonic (isentropic) expansion by the carrier C and seed S species are given by

$$u_C = u_\infty \left(1 - \frac{T_C}{T_0}\right)^{\frac{1}{2}} \tag{6.14}$$

$$u_S = u_\infty \left(1 - \frac{T_S}{T_0}\right)^{\frac{1}{2}} \tag{6.15}$$

where $\mathrm{T_0}$ is the stagnation temperature and $\mathrm{T_C}$ and $\mathrm{T_S}$ are the terminal translational temperatures of the carrier and seed gases respectively. $\mathrm{u_\infty}$ is the flow velocity for a perfect expansion from a stagnation temperature $\mathrm{T_0}$ and can be written as [298]

$$u_\infty = \left(\frac{2\gamma k T_0}{(\gamma - 1)\, m}\right)^{\frac{1}{2}} \tag{6.16}$$

where $\gamma$ is the average Poisson coefficient, $\mathrm{C_P/C_V}$, and m is the average mass of the mixture. According to these expressions, at an infinite Mach number or at a zero local temperature, both components will move at the same hydrodynamic velocity. The most probable velocities for the carrier and seed distributions are given by

$$u_{mp,C} = \frac{1}{2}\left(u_C + \left(u_C^2 + \frac{8kT_C}{m_C}\right)^{\frac{1}{2}}\right) \tag{6.17}$$

$$u_{mp,S} = \frac{1}{2}\left(u_S + \left(u_S^2 + \frac{8kT_S}{m_S}\right)^{\frac{1}{2}}\right) \tag{6.18}$$

Equations (6.17) and (6.18) allow for the determination of the extent of velocity slip in the beam expansion. Under our current experimental conditions our translational temperature measurements described in the previous section show that the expansion has reached about 90 % of the terminal expansion speed so that the maximum slip should be at most 50-100 m/s for terminal beam speeds ca. 1000-1200 m/s.

## 6.6 Reagent Prealignment

Alignment of molecules in supersonic beams is a well-documented phenomenon [299–306]. Expansion into a vacuum through a slit is inherently anisotropic in nature because the internal energy of the participating molecules is progressively being converted into translational energy along the beam axis. Moreover, molecular collisions will tend to "steer" these molecules so as to offer a smaller cross section along the velocity axis. The magnitude of this process is very much dependent on the nature of the intermolecular forces governing the collisions in the expansion. Thus it is expected that molecules with permanent electric moments and strong intermolecular potentials, as for example HBr, may tend to prealign during the expansion process.

Recall that the photogragment velocity distribution shown by Eq. (2.7) assumed both a linearly polarized photon for the photodissociation step, and a randomly oriented initial distribution of bond axes [90]. The first prerequisite is easily fulfilled by careful control of the state of polarization of the photolysis radiation, as described in Section 3.3. Even though we use mild expansion conditions, the second prerequisite had to be checked experimentally. Prealignment of the HBr molecule before photolysis would necessarily require the inclusion of other Legendre moments in the derivation of the product laboratory speed distribution for a photoinitiated chemical reaction. The HBr photodissociation data presented in Section 5.2 already shows that the anisotropy parameter for the fast channel is maximal ($\beta = -1$), in agreement with measurements from other laboratories using higher stagnation pressures [250] and static-gas conditions [248]. We also performed magic-angle ($\theta = 54.7^{o}, \mathrm{P}_2 = 0$) time-of-flight measurements. These measurements served as a further check for the Monte-Carlo simulation of the ion profiles, and showed that only up to a second-order Legendre moment was necessary for a description of all the experimental velocity distributions taken at different photolysis polarization angles. Therefore, we conclude that the prealignment of HBr molecules in the expansion is minimal and the expressions of Chapter 2 can be used safely for the analysis of the velocity distributions arising from reaction products.

For the $D_2$ molecule, which only has a permanent quadrupole moment, prealignment effects are expected to be orders of magnitude smaller than for HBr.

# Chapter 7

# State-to-State Integral Cross Sections

*There is no art so difficult as the art of observation: it requires a trained, sober spirit and highly requires disciplined experience, available only through practice; for the observer is not the one who sees of what components a thing consists, and the relationships between the components and the whole ... A natural scientist conducts experiments in order to verify the truth of his understanding; he conducts experiments to demonstrate a phenomenon in all its many aspects.*

*J. Liebig, "Introduction to Lectures on Experimental Chemistry"(1852)*

## 7.1 Background

The measurement of rotational distributions from the hydrogen exchange reaction was pioneered about fifteen years ago by our group [41, 307] using REMPI detection coupled to time-of-flight spectrometry, and by Valentini and co-workers [42] using CARS detection. These experiments were very similar to the ones presented here. A suitable photolytic precursor, generally HI, was used to provide the H-atom reagent via laser photolysis. Subsequent detection of the reaction product allowed the accurate measurement of the integral cross section for reaction into a particular ro-vibrational state of the product. These measurements represented the first quantum-state-resolved experimental data that could be compared with scattering calculations [308, 309].

These early measurements have been greatly complemented over the years with integral cross section measurements over a wide range of collision energies. In particular, Valentini and coworkers have performed measurements at 0.55 eV and 1.30 eV [310], 0.98-1.3 eV [311] for the $H + D_2$ reaction, and at 1.0 eV [312] for $D + H_2$, the latter including the determination of absolute reaction cross sections [313]. Nieh and Valentini [76, 77] scanned the photolysis wavelength to cover twenty-two collision energies from 0.95 to 1.37 eV and observed peaks in the reaction excitation function that were attributed to dynamical resonances before accurate scattering calculations [47] and further experimental work by the group of Zare and co-workers [78] showed that the observed resonance behavior was an experimental artifact.

Work in the Zare group has provided additional experimental data at collision energies ranging from 1.0 eV to 2.4 eV [200, 314–317]. Furthermore, the use of stimulated Raman pumping (SRP) of the diatomic reagent has made it possible to determine the effect of reagent vibrational excitation on the reactivity and the details of product state distributions [78, 318, 319]. In particular, experiments by Zare and co-workers [320] involving vibrationally excited reagents remain as the only experimental evidence for the presence of Geometric Phase effects in this reaction system. Comparison of experimental rotational distributions with calculations by Wu and Kuppermann [321] including and neglecting the geometric phase show a difference in the peak of the distributions by one rotational quantum in favor of the experimental data and the calculations including this phenomenon.

In this chapter we will forget momentarily about our ability to perform velocity-sensitive measurements on the $HD(v', J')$ product. The time-of-flight spectrometer will be used as a mass-selective ion detector in order to measure total integral cross sections. We have already seen in the time-of-flight calibration work presented in

Chapter 5 that it is possible to tailor the ion extraction conditions such that ion collection efficiencies are independent of ion speed. For a chemical reaction, this means that we will be able to complement the desired angular distributions with state-resolved integral cross section measurements.

## 7.2 Experimental Protocol

We have described the experimental setup in great detail in Chapter 3. Here we will describe only the experimental details pertaining the integral cross measurements.

Up to 2 mJ/pulse of deep ultraviolet light in the range between 209 and 220 nm are generated in these experiments. The output of an injection-seeded Nd:YAG (Spectra-Physics GCR-4) is used to pump a dye laser (Lambda-Physik SCANMATE 2E). The output of this dye laser is doubled (Lambda Physik SFG-1) and then tripled (INRAD Autotracker II). The linewidth of the dye laser in the fundamental is 0.25 $cm^{-1}$ and the pulse duration is 5 ns. HD molecules are detected via (2+1) REMPI through the (0,1) and (0,2) bands of the E,F $^1\Sigma_g^+ \leftarrow$ X $^1\Sigma_g^+$ transition. As the laser pulse exits the chamber it is absorbed by a pyroelectric energy meter (Molectron J-25/EPM 1000) and the reading is recorded via GPIB on a PC. Power measurements are necessary in this case because of the laser intensity shot-to-shot fluctuations and the unavoidable changes in overall laser power as we scan over the rotational lines of the HD product. The power dependence of the ion signal was recorded for each experimental run by sitting at a given rotational line and changing the laser power with a crossed-polarizer setup to minimize the effects of laser temporal and spatial mode variations on the total ion signals. The gas expansion, laser propagation, and time-of-flight axes in this experimental arrangement are mutually perpendicular.

The $H + D_2$ reaction and HD product detection take place in the extraction region of the Wiley-McLaren time-of-flight spectrometer described in Section 3.2. The steering plates in the free-drift region allows us to adjust the trajectory of the HD ions so that they strike the center of the 25 mm-diameter multichannel plate detector. Unlike the velocity-sensitive experiments, where we are interested in the distribution of HD($v', J'$) product velocities, we simply want to measure the amount of product into a particular rovibrational state. In order to do this, we remove the core extractor and increase the extraction and acceleration voltages so that all ions make it through the 6-mm hole that defines the two differentially pumped regions of the vacuum chamber. We have verified this ion collection setup by simulation with SIMION 6.0 [132] and by rotating the polarization of the laser with respect to the time-of-flight axis. At lower voltages, we have observed polarization-dependent signal areas due to the spatial anisotropy of the HBr photolysis and subsequent reaction product. These dependencies were not observed at the voltages used in the present experiment. We also scanned over the spectroscopic lines of interest to remove any Doppler rejection of our laser to products with large speed components perpendicular to the laser axis.

The product signal is collected by an oscilloscope (Tektronix TDS 620) and transferred to a PC where it is integrated as a function of dye laser wavelength. Typically, we averaged 30-60 laser shots per point. We measured HD product in states $\mathrm{v}' = 1$, $\mathrm{J}' = 0 - 13$ and $\mathrm{v}' = 2$, $\mathrm{J}' = 0 - 8$. Each scan consists of forty-two points in wavelength taken in 2 pm steps. In order to accurately measure the relative populations, the raw ion signal had to be adjusted for power fluctuations due to crystal tracking and the changes in laser gain across the dye curve. Using a thin-film polarizer (CVI Laser Corporation) in a rotational mount, we were able to reduce the power of the photolysis/probe beam without affecting its spatial mode. The integrated area of the signal at the center of the transition was recorded as a function of power for $\mathrm{HD}(\mathrm{v}' = 1, \mathrm{J}' = 5)$, $\mathrm{HD}(\mathrm{v}' = 1, \mathrm{J}' = 8)$, and $\mathrm{HD}(\mathrm{v}' = 2, \mathrm{J}' = 3)$ while complete wavelength scans over the line profile were recorded for $\mathrm{HD}(\mathrm{v}' = 2, \mathrm{J}' = 1)$ as a function of laser power. In all cases the power dependence of the ion signal was quadratic ($2.0 \pm 0.2$), implying that the ionization step in the (2+1) REMPI scheme and the photolysis of HBr were saturated. For the $\mathrm{HD}(\mathrm{v}' = 2)$ data, we scanned over each peak at least three times over the course of two days, and for the $\mathrm{HD}(\mathrm{v}' = 1)$ data we scanned over each peak at least six times over the course of three days. On a separate day we took consecutive measurements of the $\mathrm{HD}(\mathrm{v}' = 1, \mathrm{J}' = 6)$ and $\mathrm{HD}(\mathrm{v}' = 2, \mathrm{J}' = 1)$ products in order to determine the $\mathrm{v}' = 1 : \mathrm{v}' = 2$ product ratio.

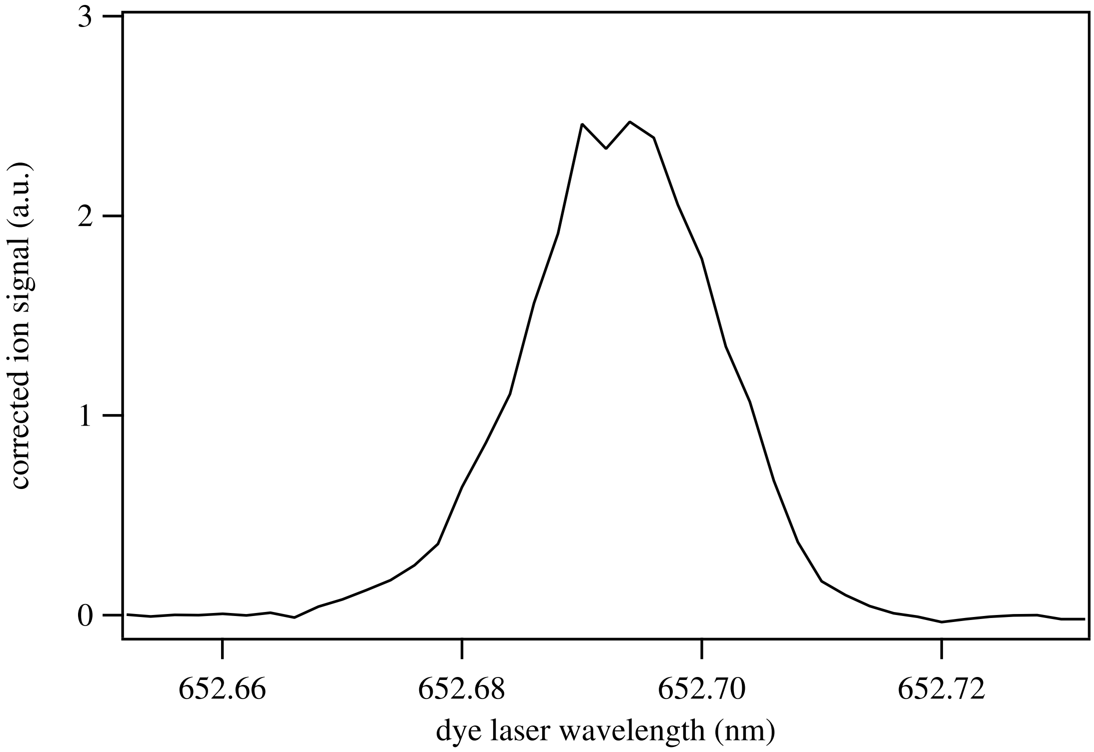


Figure 7.1: Reaction product ion signal for HD($v' = 2, J' = 1$) near 1.5 eV. The wavelength scan consists of forty-two points in 2 pm steps. Signals were corrected for power fluctuations and the results of several independent measurements averaged for each rovibrational product state to produce Table 7.1.

## 7.3 Rotational Distributions

Fig. 7.1 shows a typical wavelength scan for a single HD($v', J'$) state. The area of each peak has been adjusted to account for fluctuactions in power by taking into account the power dependence of the ion signal. It was not necessary to adjust the peaks for the rotational line strengths since these have been shown by Rinnen et al. [200, 202] to be unity within a few percent. It may be thought that a peak lineshape as shown in Fig. 7.1 may be analyzed to extract velocity information. However, our laser linewidth in the fundamental is already 0.25 $cm^{-1}$. After the doubling and tripling stages, this linewidth is increased to a value of at least 0.50 $cm^{-1}$ (for a gaussian lineshape) or 1.5 $cm^{-1}$ (for a Lorentzian lineshape). These values are of a similar magnitude as

| HD($v' = 1, J'$) product state | Average ion signal (a.u.) | HD($v' = 2, J'$) product state | Average ion signal (a.u.) |
|---|---|---|---|
| 0 | 0.033(19) | 0 | 0.009(01) |
| 1 | 0.042(09) | 1 | 0.024(05) |
| 2 | 0.071(07) | 2 | 0.043(02) |
| 3 | 0.078(09) | 3 | 0.042(02) |
| 4 | 0.097(14) | 4 | 0.044(01) |
| 5 | 0.135(22) | 5 | 0.041(03) |
| 6 | 0.153(13) | 6 | 0.028(03) |
| 7 | 0.143(15) | 7 | 0.013(01) |
| 8 | 0.121(20) | 8 | 0.010(02) |
| 9 | 0.082(24) | | |
| 10 | 0.023(23) | | |
| 11 | 0.024(09) | | |
| 12 | 0.007(03) | | |
| 13 | 0.013(05) | | |

Table 7.1: HD($v' = 1, 2$) rotational distributions ca. 1.6 eV. Numbers in parenthesis represent $1\sigma$ error in the last two digits.

the maximum Doppler shift of around 1.50 cm$^{-1}$ corresponding to an ion travelling at a speed of ±10000 m/s along the laser propagation axis. Therefore, the lineshape of our wavelength scans is dominated by instrumental parameters which preclude us from learning about the angular distribution from the Doppler profiles. To attain a velocity resolution similar to the one provided by the Wiley-McLaren spectrometer one would need a laser source with a resolution five to ten times better than ours.

The average power-corrected ion signals are shown in Table 7.1. The uncertainty in these measurements is shown in parenthesis and represents one standard deviation. For HD($v' = 1, J' = 10$) the large error is due to the doubling BBO crystal having its crystal face normal to the laser beam when achieving phase-matching conditions. The numbers reported in Table 7.1 are the result of normalizing the total area of the $v' = 1$ integral cross section to unity, and then adjusting the $v' = 2$ distribution such that the ratio of HD($v' = 1, J' = 6$) to HD($v' = 2, J' = 1$) corresponds to the measured value.

## 7.4 Discussion

### 7.4.1 Experimental Uncertainties

#### Variation in Collision Energy

Because the probe laser is also responsible for the photolytic initiation of the reaction there is a steady decrease in the center-of-mass collision energy as we tune the laser to detect higher rotational product states within a particular rotational manifold, i.e., the Q-branch progression shifts to the red from the bandhead toward higher rotational levels.

In Chapter 6 we gave upper estimates for the rotational (80-90 K) and translational (45 K) temperatures of the HBr photolytic precursor and $D_2$. From these measurements we determined an upper estimate of the collision energy resolution of $\pm50$ meV. For the HD($v' = 1, J'$) rotational distribution, the collision energy ranges from 1.72 eV for HD($v' = 1, J' = 0$) to 1.57 eV for HD($v' = 1, J' = 13$). Similarly, for the HD($v' = 2, J'$) distribution the collision energy varies from 1.55 eV for HD($v' = 2, J' = 0$) to 1.49 eV for HD($v' = 2, J' = 8'$). In the HD($v' = 1, J'$) case the change in collision energy caused by the change in photolysis/detection laser frequency is greater than our experimental collision energy resolution. Therefore, we expect that this will be the largest source of error when the experimental distributions are compared to theoretical predictions.

#### Photolysis Branching Ratio

In addition to the variation of collision energy with laser wavelength, there are two possible speeds for the H-atom photofragments arising from the photodissociation of HBr (cf. Section 5.2). Because the "fast" channel represents the majority of the H-atoms, as evidenced by our measurements of the photolysis branching fraction, and the reaction rates are higher for this channel, the "slow" channel does not have a measurable effect in the reaction. Taking into account these two factors we estimate

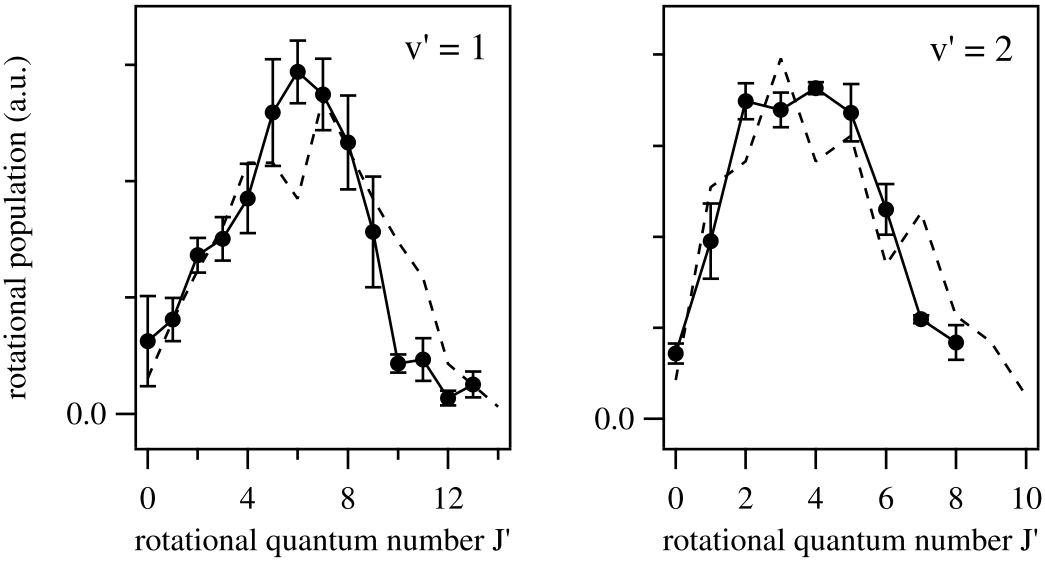


Figure 7.2: (a) HD($v' = 1, J'$) rotational distribution at 1.70 eV. The dashed lines have been taken from the QCT calculations of Truhlar et al. (b) Same as (a) but for HD($v' = 2, J'$) at 1.55 eV.

that the slow channel does not contribute more than a few percent to the measured ion signals.

### 7.4.2 Comparison with Theory

Blais and Truhlar [322] have reported integral cross sections for the $H + D_2$ reaction at collision energies of 1.5, 1.6, 2.25, and 2.4 eV on the DMBE potential energy surface. These calculations were meant for comparison with the "prompt" product distribution measurements of Rinnen et al. [315] using HI as photolytic precursor. For these trajectory calculations, $D_2$ was assigned a temperature of 300 K for the vibrational and rotational degrees of freedom to simulate the experimental conditions. A total of 12000 trajectories were run at 1.5 eV, 5000 at 1.6 eV, 30000 at 2.24 eV, and 18197 at 2.4 eV. We are fortunate that the collision energies of the slow HI channel, for which these calculations were intended, correspond with those for the fast channel of HBr at our photolysis wavelengths.

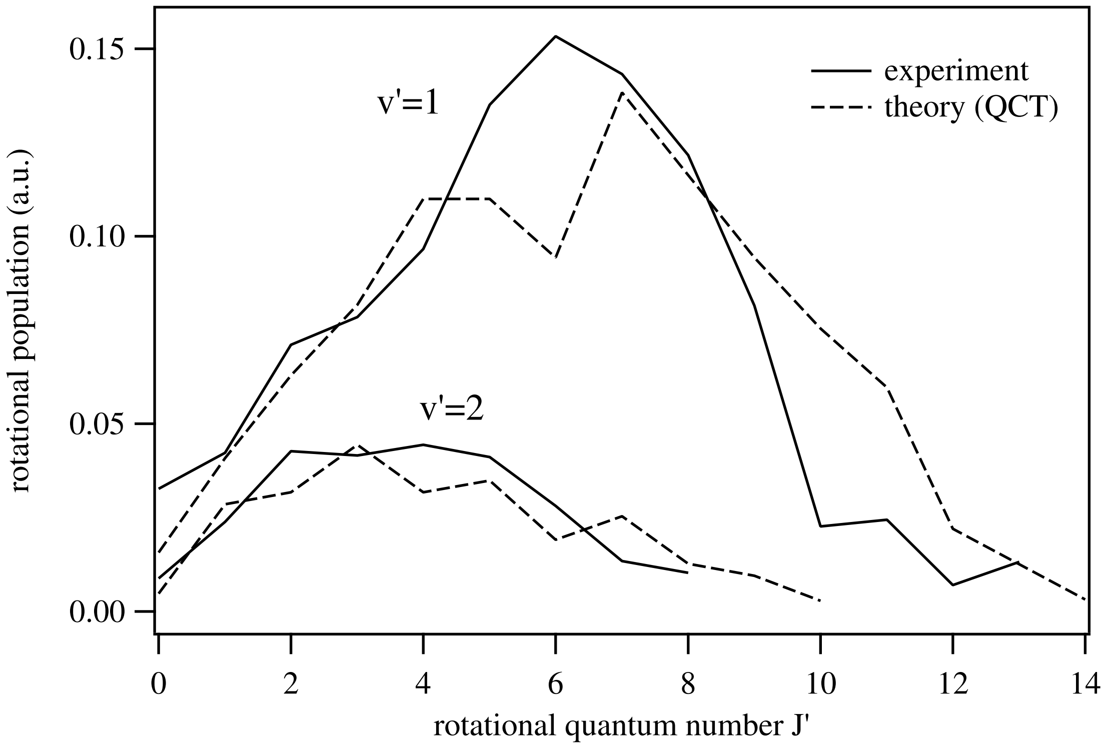


Figure 7.3: Comparison of experimental rotational distributions with theory including the measured product vibrational branching ratio. Error bars in the experimental points have been omitted for clarity.

Our results for $\mathrm{HD}(\mathrm{v}' = 1, \mathrm{J}')$ and $\mathrm{HD}(\mathrm{v}' = 2, \mathrm{J}')$ are compared to the results of Blais and Truhlar in Fig. 7.2. The area of the Blais-Truhlar $\mathrm{HD}(\mathrm{v}' = 1, \mathrm{J}')$ distribution was adjusted such that it had the same area from $\mathrm{J}' = 0$ to $\mathrm{J}' = 13$ as our $\mathrm{HD}(\mathrm{v}' = 1, \mathrm{J}')$ results. Similarly, the Blais-Truhlar $\mathrm{HD}(\mathrm{v}' = 2, \mathrm{J}')$ was adjusted to have the same area from $\mathrm{J}' = 0$ to $\mathrm{J}' = 8$ as our $\mathrm{HD}(\mathrm{v}' = 2, \mathrm{J}')$ experimental data. Additionally, Fig. 7.3 compares our measurement of the vibrational branching ratio for $\mathrm{v}' = 1$ and $\mathrm{v}' = 2$ product with that from the same quasiclassical calculations.

The agreement between the quasiclassical trajectory calculations and our experiments as shown in Figs. 7.2 and 7.3 is quite good. One possible exception to this overall agreement may be $\mathrm{HD}(\mathrm{v}' = 1, \mathrm{J}' = 6)$. We are confident, however, that our reported value for this rovibrational state is correct within the error bars. The disagreement may be caused by the variation in the collision energy across the rotational distribution. Additional causes may be the different temperatures between the calculations (300 K) and experiment (80 K). Upon close inspection of Fig. 7.2 it can be seen that both experimental distributions are slightly colder than the quasiclassical calculations. The same behavior was observed when these calculations were originally compared to the results of Rinnen et al. [322]. We are not aware of more recent quasiclassical calculations on more accurate potential energy surfaces such as the BKMP2 [66] or EQMC [67] surfaces. In light of the agreement between the LSTH, DMBE and BKMP2 [323] surfaces at nearby energies, we would be surprised to see large differences between the results used to contrast against experiment and more accurate calculations.

### 7.4.3 Surprisal Analysis

It has been customary for this reaction system to analyze product rotational distributions in terms of linear surprisal parameters. This type of analysis was first suggested by Levine and Bernstein [324–326] as a means of describing energy disposal from chemical reactions. Wyatt [327] was the first one to apply it to the $H + H_2$ reaction.

Surprisal analysis involves the definition of a standard or "prior" internal energy distribution. In the case of a chemical reaction, the shape of the prior distribution of rotational levels is dictated by conservation of energy and the density of states. In this sense, the prior distribution corresponds to a statistical limit for a given total energy. For the atom-diatom case one can show that such as distribution is given by [328]

$$P^0\left(v', J'; E\right) \propto (2J+1) \cdot \left(E - E_{V'} - E_{R'}\right)^{\frac{1}{2}} \tag{7.1}$$

where E is the total energy, and $\mathrm{E_{V'}}$ and $\mathrm{E_{R'}}$ are the product vibrational and rotational energies respectively. For the analysis of rotational rotational distributions within a given vibrational manifold, the prior distribution is only a function of the rotational quantum number and internal energy associated with this level.

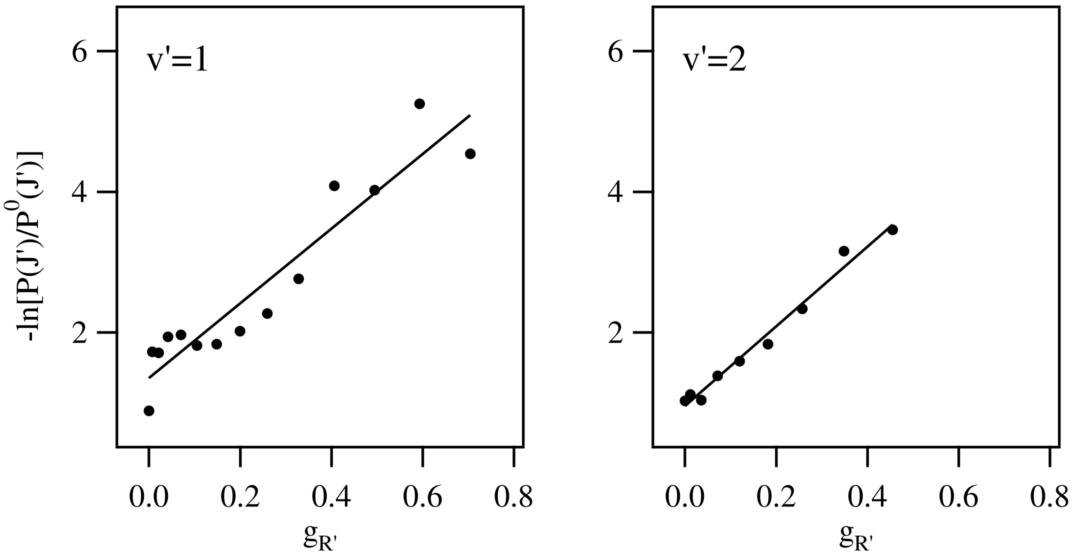


Figure 7.4: Surprisal plots for the rotational distributions. The results of the linear fits in terms of surprisal parameters are $\theta_{\mathrm{R}'} = 5.3 \pm 0.5$ for $\mathrm{v}' = 1$ and $\theta_{\mathrm{R}'} = 5.7 \pm 0.3$ for $\mathrm{v}' = 2$

To obtain a measure of how far from statistical behavior our particular internal energy distribution is, we introduce a linear surprisal parameter $\theta_{\mathrm{R}'}$ defined as

$$-ln\left(\frac{P(J')}{P^0(J')}\right) = \lambda + \theta_{R'} g_{R'} \tag{7.2}$$

where $\mathrm{g}_{\mathrm{R}'}$ is the reduced rotational energy given by

$$g_{R'} = \frac{E_{R'}}{E - E_{V'}} \tag{7.3}$$

Defined in this manner, positive values of $\theta_{\mathrm{R}'}$ correspond to distributions "colder" than the prior limit. Surprisal plots for the measured $\mathrm{HD}(\mathrm{v}' = 1, \mathrm{J}')$ and $\mathrm{HD}(\mathrm{v}' = 2, \mathrm{J}')$ are shown in Fig. 7.4.

A linear surprisal fit to the experimental points yield $\theta_{\mathrm{R}'} = 5.3 \pm 0.5$ for $\mathrm{v}' = 1$ and $\theta_{\mathrm{R}'} = 5.7 \pm 0.3$ for $\mathrm{v}' = 2$. These figures indicate that in both cases the rotational distributions peak at a lower rotational level than what it would be expected in the prior limit. That is, there are constraints more important than energy conservation and density of states which are determining internal energy disposal in this reaction system. The values for the linear surprisal fits here reported are also consistent with previous rotational distribution measurements ($\theta_{\mathrm{R}'} = 2.1 - 5.9$) [41, 310, 311] as well as with quasiclassical and quantum scattering calculations ($\theta_{\mathrm{R}'} = 2.5 - 8.9$) [327, 329].

A surprisal analysis as the one presented here has limited value. Whereas it provides a quantitative measure of the deviation from complete statistical behavior it does not provide information about what may be the cause of the observed trends. In the next two chapters we will see how the measurement of angular distributions will provide us with a means for explaining in a semiquantitative fashion the location of the peak as well as the overall shape of the rotational distributions.

# Chapter 8

# State-to-State Differential Cross Sections

*A molecule swims, dispersing its functionality, scattering its reactive centers. Not every collision, not every punctilious trajectory by which billiard-ball complexes arrive at their calculable meeting places leads to reaction. Most encounters end in a harmless sideways swipe. An exchange of momentum, a mere deflection. And so it is for us.*

*R. Hoffmann, "The Metamict State" (1987)*

## 8.1 Background

The measurement of product angular distributions from chemical reactions constitutes one of the most sensitive ways of probing the dynamics of elementary chemical events [5, 330–334]. This measurement is more powerful if, in addition, it is possible to attain quantum-state resolution of the scattered product. When possible, the study of angular distributions as a function of both the collision energy and the internal state of the products can be used very efficiently to reach a better understanding of the forces leading to the making and breaking of chemical bonds.

For almost three decades several groups have attempted the measurement of state-resolved angular distributions for the hydrogen exchange reaction. Even though this system is the simplest neutral bimolecular reaction and also the most thoroughly studied one from a theoretical point of view, a large body of experimental data to contrast against the most accurate scattering calculations is still lacking. Reasons include: a small total reaction cross section ($1-2$ Å$^2$) [335–338]; a large number ($> 25$) of rovibrational product states populated with cross sections in the order of $10^{-2}$ to $10^{-3}$ Å$^2$; the need for UV, VUV or Raman detection techniques to probe the reaction products; and the difficulty to measure not only the product yield into a particular state but also to obtain angular information of sufficient resolution from such data.

The first measurement of the total product differential cross section from the isotopically substituted $D+H_2$ reaction at a mean collision energy of 0.48 eV was performed by Geddes, Krause, and Fite [39] in 1972. The experimental setup consisted of a crossed molecular beam chamber equipped with a high-temperature effusive furnace for hot-atom generation and an electron-impact ionizer/quadrupole mass spectrometer for HD product detection. The angular distribution was found to be preferentially backward scattered, a finding consistent with available theoretical calculations at the time. Work along these lines was followed by Kwei and Lo [43] who studied the reaction of H and D atoms with $T_2$ molecules at 0.7 eV using an effusive hot-atom source and a $MnO_3$ detector for tritium atom detection. The HT/DT angular distributions were also found to be backward scattered. Götting, Mayne and Toennies carried out further experiments for the $D+H_2$ reaction at collision energies of 1.0 eV [339] and 1.5 eV [44]. Hot-atom generation at these high center-of-mass collision energies was achieved by the use of an arc discharge capable of creating D-atom velocity distributions with mean energies as high as 3.0 eV. In these studies the product angular distributions were observed to shift to smaller angles with increased collision energy, in agreement with quasiclassical trajectory calculations on the Liu, Siegbahn, Truhlar, Horowitz (LSTH) [61, 62] potential energy surface. By the end of the 1980's, the marriage of the crossed-beam technique with laser photolysis for hot-atom generation, and laser spectroscopy for quantum-state-specific product detection made it possible to refine the experimental conditions to an unprecedented level of detail. The work of Buntin. Giese, and Gentry [45] using $D_2S$ photolysis at 248 nm for D-atom generation, and Continetti, Balko, and Lee [46] employing DI photolysis at 248 nm provided the first angular distributions with some internal energy resolution of the diatomic product.

From these initial attempts, the difficulties associated with state-resolved measurements using conventional crossed-beam techniques became apparent. As a result, laser spectroscopy became the method of choice for product detection. Most recently, Schnieder and co-workers [98, 340–342] have combined the crossed-beam technique with laser photolysis of HI and the ultrasensitive detection scheme of D-atom Rydberg tagging time-of-flight spectroscopy to perform the first fully state-resolved study of the $H + D_2$ reaction at 1.28 and 0.55 eV. The availability of this experimental data has fostered recent calculations of state-resolved angular distributions [85, 86, 98, 340–344] and product rotational polarization [345, 346] using quantum mechanical and quasiclassical methods.

In contrast with the difficulties associated with the experimental efforts listed above, the photoloc technique [88, 89, 347] allows conducting the experiments in a single molecular beam expansion thereby greatly reducing the complexity of the experimental setup. Reaction is initiated by photolysis of a suitable molecular precursor and angular measurements are performed by inversion of the product laboratory speed distribution into a center-of-mass differential cross section. The major prerequisities for the successful application of this technique are a knowledge of the spatial anisotropy of the photolysis step as well as velocity-sensitive, quantum-state specific detection of the reaction product. The inversion of the laboratory speed distribution is then possible by straightforward application of energy and momentum conservation along with the law of cosines which maps a single product laboratory speed onto a unique center-of-mass scattering angle. Implementation of this or similar techniques has already been proven very useful for the study of several reaction systems in our and other laboratories in the past few years. These include, for example: $Cl + CH_4$ [348, 349], $Cl + C_2H_6$ [350–352], $H + O_2$ [117], $O + H_2$ [115], and $H + CO_2$ [116]. Some of these experiments have been successful at measuring not only state-to-state differential cross sections but also product rotational polarization [89, 353, 354], and the effect of reagent vibrational excitation [355], and alignment [356] on product angular distributions. These measurements have opened up a new and unexplored area in the field of experimental reaction dynamics devoted to the investigation of vector correlations [357–365].

In regard to the hydrogen exchange reaction, the photoloc technique has made it possible to attain sufficient product number densities under single-collision conditions to make the measurement of state-resolved differential cross sections possible. Prior to the work described in this chapter, Shafer et al. [119] measured total D-atom angular distributions using 2D-REMPI-TOF spectrometry. Similarly, the use of HD Rydberg tagging in conjunction with impulse-extraction time-of-flight spectroscopy allowed Xu et al. [120] to measure the differential cross section for $HD(v' = 4, J' = 3)$ at 2.2 eV. The use of state-specific spectroscopic detection schemes such as molecular Rydberg tagging or, in our case, REMPI for the detection of $HD(v', J')$ products permits the isolation of a particular quantum state of the product, with almost no overlaps with other product states. This ability to isolate particular quantum states is particularly useful in two situations: (1) when we want to measure the differential cross section into states that constitute a small fraction of the overall product flux, i.e, highly excited products; and (2) when the collision energies are sufficiently high for many HD product channels to be open, thus increasing the number of nearly isoenergetic D-atom translational states. It is for this reason that the work of Schnieder et al. has not been capable of providing in their high-collision-energy experiments at 2.2 eV [366] and 2.67 eV [367] the same amount of information as that obtained in their beautiful experiments at 1.28 and 0.55 eV. As of the writing of this thesis, the same group has repeated the differential cross section measurements at 2.20 eV with improved D-atom translational energy resolution [368]. Despite some overlaps between different $HD(v', J')$ product states the agreement with quantum-mechanical calculations on the Boothroyd, Keogh, Martin, Peterson (BKMP2) [66] surface is very good.

This chapter presents the first systematic studies of angular distributions from the $H + D_2$ reaction using the photoloc technique. For this reason, each section contains a detailed account of the experimental method followed for each set of measurements. We also describe qualitatively the trends found in the angular distributions as a function of the internal energy (vibrational and/or rotational) of the product, and compare our results with other experiments.

## 8.2 $\mathbf{HD(v' = 1, J' = 1, 5, 8)}$ at 1.70 eV

### 8.2.1 Experimental Protocol

The experimental setup, the calibration of the time-of-flight and the characterization of reaction conditions have been described in detail in Chapters 3, 5 and 6. Here we will restrict ourselves to a brief account of the apparatus and the salient features of the experimental method followed in this particular set of measurements.

A 1:4 HBr (Matheson, 99.9% purity) and $D_2$ (Cambridge Isotope Laboratories, 99.8% purity) mixture held at a stagnation pressure of 300 Torr in a passivated reagent manifold is expanded into a vacuum chamber with a pulsed solenoid valve (General Valve Corporation, series 900, 0.5 mm orifice) operating at 10 Hz. Typical gas pulses, as measured by monitoring $D_2$ EF $^1\Sigma_g^+ \leftarrow$ X $^1\Sigma_g^+$ and HBr H $^1\Sigma_g^+ \leftarrow$ X $^1\Sigma_g^+$ (2+1) REMPI ion signals, are approximately 600 $\mu$s. The pulsed solenoid valve injects the gas pulse into the extraction region of a Wiley-McLaren time-of-flight spectrometer [122] at nominal pressures of 5.0-10.0x$10^{-7}$ Torr. It is in this region that reaction takes place.

The linearly polarized output of a dye laser (Lambda Physik SCANMATE 2E) pumped by the second harmonic of an injection-seeded Nd:YAG laser (Spectra Physics GCR-4) is doubled and mixed in BBO crystals to reach 208-220 nm. Typical output powers in this wavelength range are between 0.5-1.5 mJ/pulse with pulse durations of 5-6 ns as measured with a fast photodiode (ET 2000). The UV output is efficiently separated from the fundamental and doubled beams by the use of dichroic mirrors (CVI corporation). The beam is sent through a 3:1 Galilean telescope prior to being focused by a 600 mm fused silica plano-convex lens to enhance beam focusing, and through a set of UV polarizers (CVI corporation) for fine control of the laser power. The state of polarization of the beam is controlled by the use of a halfwave plate (Optics for Research) mounted on a rotatable optical stage.

In the experiments described in this section, the same laser is used to photolyze HBr and to detect the resulting reaction product created within the laser temporal pulse width (5-6 ns). In this regime, it is safe to neglect effects caused by fly-out of the reaction product, as it has already been shown in past integral cross section measurements in this laboratory [315–317]. The laser beam traverses the vacuum chamber perpendicular to both the nozzle and time-of-flight axes. Chemical reaction occurs at 25-35 nozzle diameters away from the nozzle exit so as to ensure single-collision conditions (See Section 6.2). During these experimental runs we have further checked for secondary collisions affecting the velocity distributions by recording time-of-flight profiles at different nozzle distances and ensuring that the measured velocity profiles correspond to those of a nascent distribution.

HD($\mathrm{v}' = 1, \mathrm{J}'$) product molecules are detected via (2+1) REMPI in a quantum-specific manner using the Q-branch members of the HD EF $^1\Sigma_g^+ \leftarrow$ X $^1\Sigma_g^+$ (0,1) band [200, 202]. This detection scheme is largely insensitive to the rotational polarization of the product as explicitly shown in Chapter 4. Consequently, $HD^+$ ion intensities can be related to the ground state populations of the quantum rovibrational state of interest. $HD^+$ ions are then extracted into the acceleration and free drift regions of the time-of-flight apparatus, core-extracted by a 3 mm conical mask (Beam Dynamics Inc.), and finally detected with a Chevron-type multichannel-plate detector (Galileo Corporation) held at 2.0-2.4 kV. Ion signals are recorded in a digital oscilloscope (Tektronix TDS620) and sent via GPIB interface (National Instruments) to a personal computer for further analysis.

### 8.2.2 Results

Table 8.1 summarizes the reaction parameters for the HD($\mathrm{v}' = 1, \mathrm{J}' = 1, 5, 8$) states detected ca. 1.70 eV. Since we are using the same laser to photolyze and detect the

| Reaction Parameter | HD($v' = 1, J'$) product $J' = 1$ | $J' = 5$ | $J' = 8$ |
|---|---|---|---|
| Collision energy (eV) | 1.71 | 1.70 | 1.66 |
| Center-of-mass speed (m/s) | 4059 | 4028 | 3986 |
| $D_2$ vibrational energy (eV) | 0.191 | 0.191 | 0.191 |
| $D_2$ rotational energy (eV) | 0.005 | 0.005 | 0.005 |
| HD vibrational energy (eV) | 0.683 | 0.683 | 0.683 |
| HD rotational energy (eV) | 0.011 | 0.156 | 0.364 |
| HD center-of-mass speed (m/s) | 5497 | 5086 | 4432 |
| HD laboratory speed (m/s) | | | |
| Fast (forward scattered) | 9556 | 9114 | 8418 |
| Slow (backward scattered) | 1439 | 1057 | 446 |

Table 8.1: Summary of reaction parameters for HD($v' = 1, J'$) experiments.

HD product, the collision energy varies slightly from 1.71 eV for $J' = 1$ to 1.66 for $J' = 8$. This change in collision energy is still within the collision energy spread of 50 meV inherent in these experiments. The collision energy spread corresponds to an upper limit obtained from measurements of the translational temperatures of the reagents ($\approx$ 45 K), and the rotational distribution of the HBr reagent. The $D_2$ reagent distribution has been measured by (2+1) REMPI and corresponds to 0.45:0.35:0.10 in the J=0, 1, and 2 levels of the ground state vibrational level. The reagent and product internal energies have been calculated from the spectroscopic values for the ground state of the HD molecule as given by Huber and Herzberg [94].

The center-of-mass and laboratory speeds of the HD products are listed in the last two rows of Table 8.1. Accounting for the photolysis branching ratio [250, 347], the different rate constants [322], and the detection geometry the contribution of the slow photolysis channel to the signal is not more than 10-15% in the worst case scenario.

Figure 8.1 shows typical core-extracted time-of-flight profiles for the three rovibrational states pertinent to this section. The profiles for HD($v' = 1, J' = 5$) and HD($v' = 1, J' = 8$) were obtained at a extraction voltage of 50 V whereas that for

$HD(v' = 1, J' = 1)$ required, because of small signal levels, an extraction voltage of 100 V. This increase in extraction voltage from 50 V to 100 V translates into a twofold temporal compression of the ion packet. For ease of comparison with the other two time-of-flight profiles, the time axis for $HD(v' = 1, J' = 1)$ has been expanded by a factor of two. With the experimental data plotted in this manner, a given time-of-flight shift from zero corresponds to the same speed along the time-of-flight axis for all three profiles shown in Fig. 8.1.

Each profile is the result of counting all the ions arriving at $m/e = 3$ during 20000 laser shot intervals. All three profiles were recorded with the laser polarization perpendicular to the time-of-flight axis. The signals were carefully checked for experimental artifacts including improper centering of the core extractor and space-charge effects arising from the concomitant production of $Br^+$ and $HBr^+$ ions. We should point out that the use of HBr as a photolytic precursor helped at greatly reducing reagent ion backgrounds. At typical probe wavelengths, between 200 and 240 nm, experiments using HI produced large amounts of $I^+$ and $HI^+$ ions, mostly correlating with the power of the focused probe beam. We attribute this difference in backgrounds for HBr compared to HI as being caused by the lower ionization potential of the later. Direct two-photon ionization of HI or I is possible below 238 nm, whereas for HBr and Br the wavelength threshold is moved to ca. 210 nm. Young has proposed this (1+1) multiphoton direct ionization scheme as a means of detecting HI molecules [369] and clusters [370, 371]. The large disparity between reagent and product number densities in the reaction region also explains why ion peaks arising from two-photon direct ionization can overwhelm the mass spectrum and cause unexpected distortions in the measured velocity distributions.

The solid line accompanying each profile in Fig. 8.1 is the result of a linear least-squares fit using a total of twelve evenly-spaced basis functions. The fit was performed via both a singular-value decomposition [243] and a maximum entropy plus simulated annealing algorithm [117, 121, 241]. The results from either fitting procedure are indistinguishable within the error of our measurements. The core-extracted velocity basis functions were generated via a Monte-Carlo simulation of the instrument. The instrumental calibration parameters used for the modeling of these basis functions

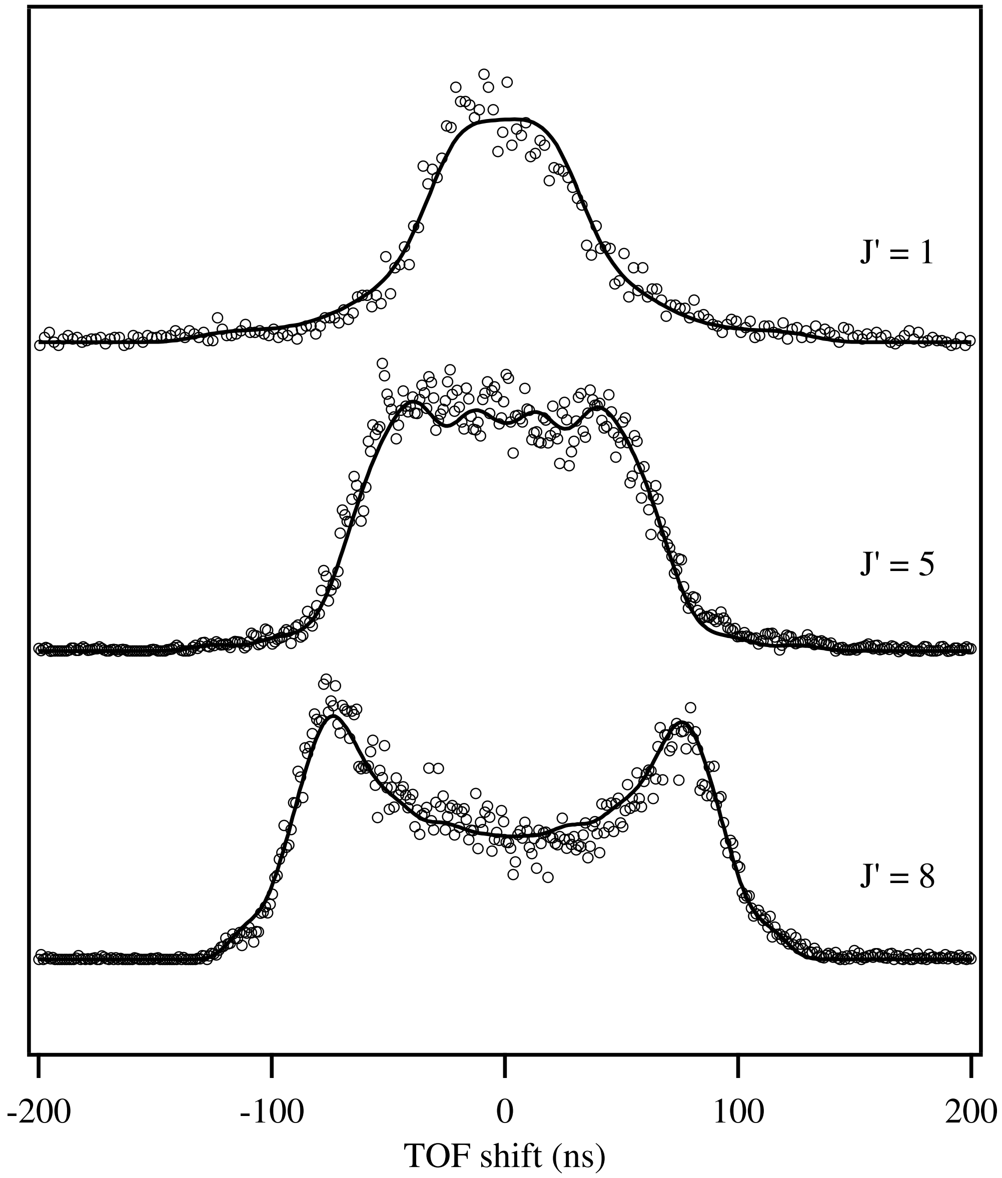


Figure 8.1: Core-extracted time-of-flight profiles for HD($v' = 1, J'$) products at collision energies ca. 1.7 eV. HD detection was accomplished by (2+1) REMPI through the Q-branch members of the HD EF $^1\Sigma_g^+ \leftarrow$ X $^1\Sigma_g^+$ (0,1) band. The solid lines are least-squares fits to the experimental profiles using the methods described in the text. For clarity, the profile for $J' = 1$, taken at half the velocity resolution, has been expanded by a factor of two along the abcissa.

have been described in Chapter 5.

Each laboratory speed of the HD reactive product corresponds to a unique scattering angle in the center-of-mass frame according to the law of cosines. Similarly, the product angular distribution and, hence, the differential cross section are then related to the measured velocity distribution by a simple Jacobian transformation as shown by Eq. 5.2 of Section 5.1. Figure 8.2 shows the angular distributions derived from the core-extracted fime-of-flight profiles of Fig. 8.1. At least five measurements were performed for each rovibrational state. The $1\sigma$ error bars shown include both the statistical uncertainties arising from the linear least-squares fits as well as the systematic variations from separate measurements. We estimate an angular resolution of 5-6$^{\rm o}$ in the backward region and 12-13$^{\rm o}$ in the forward scattering region with the velocity resolution of these measurements.

The angular distributions of Fig. 8.2 show a marked dependence on the final rotational quantum number of the $\mathrm{HD}(\mathrm{v}' = 1, \mathrm{J}')$ product. For $\mathrm{J}' = 1$, it peaks at $\sim 170^{\rm o}$ and the distribution is quite sharp, reaching twenty percent of its maximal value at $\sim 130^{\rm o}$. The larger error bars in this angular distribution arise from an incrased covariance between basis functions as a consequence of a higher extraction voltage (i.e., worse velocity resolution) required for the measurement of this particular product state.

Figure 8.2b shows the angular distribution for $\mathrm{J}' = 5$. Its peak has shifted to $\sim 133^{\rm o}$ and a broader range of angles contributes to product scattering. In addition to these coarse features, the angular distribution appears to show a local minimum at $\sim 155^{\rm o}$. This feature is present in all the time-of-flight profiles measured for this state and persists if the basis-set calibration parameters are varied over a reasonable but wide range of values.

Finally, for $\mathrm{J}' = 8$ the maximum in the angular distribution has shifted to $\sim 100^{\rm o}$ and its breadth has roughly doubled with respect to that at $\mathrm{J}' = 5$. A preference exists, however, for scattering into the backward hemisphere, as evidenced by the asymmetry of the distribution with respect to complete side scattering at $90^{\rm o}$.

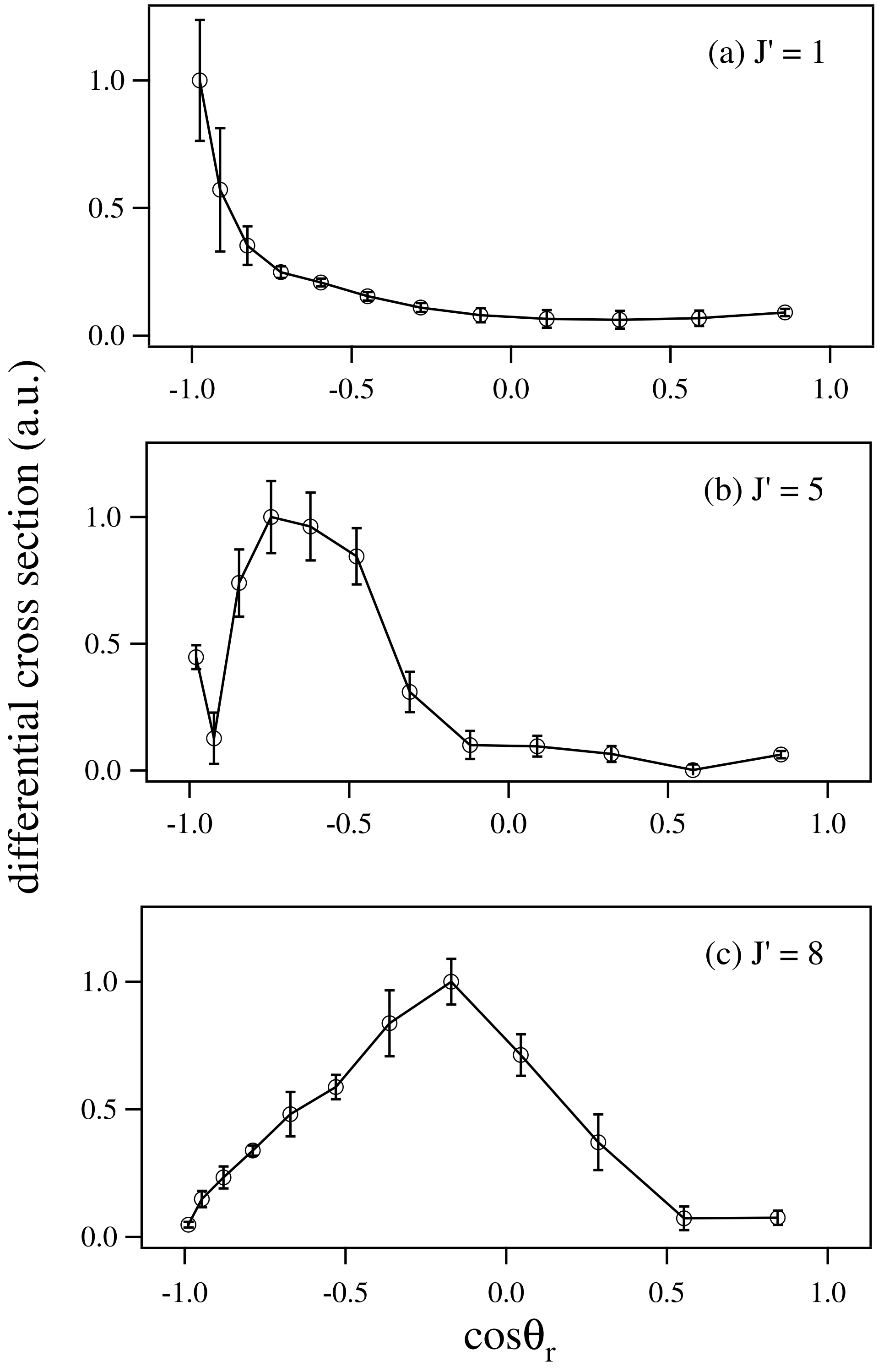


Figure 8.2: Angular distributions derived from the core-extracted time-of-flight profiles shown in Fig. 8.1. The solid lines are guides to the eye. Error bars are $1\sigma$ and they include both random and systematic errors in the measurements.

### 8.2.3 Discussion and Comparison with Other Work

Presently, no theoretical calculations exist for this reaction at these collision energies. In the future, it would be interesting to compare our results with theoretical calculations carried out with and without the Geometric Phase, because the presence of this effect is predicted [321, 344] to have more pronounced effects at higher collision energies than those probed in other experiments performed up to the present time.

Comparison with the theoretical and experimental work at 1.28 eV shows that, qualitatively, the reaction behaves in a similar manner at both collision energies. The angular distributions of Schnieder and co-workers [340] for the same states we have probed peak at approximately 175°, 120°, and 90°. They also show a similar broadening of the angular distribution with rotational quantum number. Such a similarity in behavior at post-threshold collision energies suggests that, to a first order approximation, the same dynamics determine the measured angular distributions.

## 8.3 $\mathbf{HD(v' = 2, J' = 0, 3, 5)}$ at 1.55 eV

### 8.3.1 Improvement of Experimental Protocol

More complete descriptions of the experimental protocol has been given in Section 8.2. As with the $\mathrm{HD(v' = 1, J')}$ measurements presented in Section 8.2, we have used the same laser pulse to detect the nascent $\mathrm{HD(v' = 2, J')}$ product. Product detection was accomplished via the Q-branch members of the HD EF $^1\Sigma_g^+ \leftarrow$ X $^1\Sigma_g^+$ (0,2) band. The sensitivity of this particular spectroscopic band is of a similar magnitude as the (0,1) band previously employed for the detection of $\mathrm{HD(v' = 1, J')}$ product [200, 202].

Linearly polarized radiation around 217 nm was generated by tripling the output of a pulsed dye laser pumped by the doubled output of an Nd:YAG laser. Typical output powers ranged between 1.0 and 1.5 mJ/pulse. The beam was recollimated and focused by a 500 mm plano convex lens prior to entering the vacuum chamber. Special care was exercised to have a well-defined laser polarization entering the vacuum chamber. The purity of the polarization is crucial for a proper modeling of the core-extracted time-of-flight signals. The state of polarization of the laser light was checked before and after the reaction region to ensure it was preserved after passing through the fused-silica chamber windows which, under stress, may display birefringence. These windows were periodically taken out of the beam line and checked for burns or spot marks produced by repeated exposure to UV radiation. The laser power was fine-controlled by a set of two UV polarizers (CVI corporation). Careful control of the laser power proved to be crucial in these experiments because excessive laser fluences tended to produce severe distortions in the time-of-flight profiles. Reaction was initiated by the photolysis-probe laser at 25 to 35 nozzle diameters below the nozzle orifice to ensure single-collision conditions.

A smaller cross section leading to $\mathrm{HD}(\mathrm{v}' = 2, \mathrm{J}')$ levels make the measurements presented here more challenging than those reported for the $\mathrm{HD}(\mathrm{v}' = 1, \mathrm{J}')$ vibrational manifold. Consequently, additional care had to be exercised to remove ion backgrounds at other masses produced by the high intensity of the focused laser beam. These backgrounds arise from the breakage and further ionization of the reagents HBr and $D_2$, whose number densities are several orders of magnitude larger than those from the desired reaction products. Large backgrounds from $D^+$ and $D_2^+$ were very dependent on the laser power and the temporal delay between the firing of the pulsed nozzle and the laser pulse, i.e., the local number density in the beam. Too large ion signals at these masses, specially from the $D^+$ at $\mathrm{m/e} = 2$, tended to leak into the mass window corresponding to HD product, contributing to baseline degradation and instability. Moreover, high-mass ions such as $HBr^+$ and $Br^+$ arising from multiphoton dissociation and ionization of the HBr reagent were particularly detrimental to the lineshape of the $HD^+$ ion signal. Owing to the large mass of these ions, they have very long residence times in the extraction region of the time-of-flight spectrometer compared to those of the lighter reaction products. The presence of large quantities of these quasi-static ions in the extraction region caused severe distortions in the time-of-flight profiles, thus impairing the extraction of reliable velocity information. Because of the characteristics of our time-of-flight apparatus [347], ion peaks for a given mass should appear symmetric about the arrival time of an ion with no speed along the detection axis. This symmetry requirement served as a very useful diagnostic tool to improve the experimental conditions. The data presented in this

| Reaction Parameter | HD($v' = 2, J'$) product $J' = 0$ | $J' = 3$ | $J' = 5$ |
|---|---|---|---|
| Collision energy (eV) | 1.56 | 1.55 | 1.53 |
| Center-of-mass speed (m/s) | 3856 | 3844 | 3826 |
| $D_2$ vibrational energy (eV) | 0.191 | 0.191 | 0.191 |
| $D_2$ rotational energy (eV) | 0.005 | 0.005 | 0.005 |
| HD vibrational energy (eV) | 1.109 | 1.109 | 1.109 |
| HD rotational energy (eV) | 0 | 0.060 | 0.148 |
| HD center-of-mass speed (m/s) | 3919 | 3684 | 3309 |
| HD laboratory speed (m/s) | | | |
| Fast (forward scattered) | 7775 | 7528 | 7136 |
| Slow (backward scattered) | 62 | 160 | 517 |

Table 8.2: Summary of reaction parameters for HD($v' = 2, J'$) experiments.

section has been measured under conditions in which all these experimental artifacts have been reduced to an acceptable level. No attempt has been made to symmetrize the time-of-flight profile about zero time delay a posteriori or to artificially remove spurious ion backgrounds.

Once we were capable of finding reactive signal from the reaction, the laser power and reagent number densities were reduced to levels under which background ion peaks were insignificant and did not affect the product velocity distributions. This conditions generally required us to operate under single-ion counting conditions, and to acquire data for time intervals of at least 20-30 minutes. As we found in previous angular distribution measurements, the optimal place to probe for nascent reaction products is located within the first 50 to 100 $\mu$s of the 600-$\mu$s gas pulse. Under these operating conditions the rotational distribution of the $D_2$ reagent and the collision energy spread was found to be the same as previously reported in Section 8.2

### 8.3.2 Results

Table 8.2 summarizes the reaction parameters pertinent to this study. Owing to the proximity of the rotational lines used for product detection, the change in collision energy in these measurements is less than 30 meV. This value is still within the measured collision energy spread of 50 meV. Therefore, the three states measured in this study can be considered to be at the same collision energy. The HD center-of-mass speeds shown in the last two rows of this table have been calculated from a straightforward application of energy and momentum conservation following the procedures of Chapter 2.

Although the slower HBr photolysis channel can still contribute to reaction product, our measurements of the HBr photolysis branching ratio at these wavelengths (cf. Table 5.2) show that only 14% of this slower channel is produced under the current experimental conditions. Moreover, our probing scheme is sensitive to the state-to-state reaction rate and not to the reaction cross section. Since we are probing more energetic products than in the HD($v' = 1$) case, the contribution of the slow channel to the reactive signal is at most 8-10 %, if we take into account both the slightly lower collision energy as well as the smaller reaction cross section [308, 322]. We are thus confident that, within the uncertainties in the measurements presented below, the velocity distributions and, consequently, the center-of-mass differential cross sections arise from the fast photolysis channel.

Figure 8.3 shows representative core-extracted time-of-flight profiles for HD($v' = 2$, $J' = 0, 3, 5$) taken with the laser polarization perpendicular to the time-of-flight axis. Despite the expected lower cross sections for reaction compared to HD($v' = 1, J'$) product, we have been able to obtain background-free reactive product signals of comparable, if not better, quality to the HD($v' = 1, J'$) previously presented.

The extraction voltage conditions used in these experiments are such that reactive signal should be found 120 ns on either side from the center of the time-of-flight profile for the three rotational states shown in Fig. 8.3. These expectations are clearly fulfilled by the time-of-flight profiles shown in this figure. We should note the lack of any spurious background outside the physical bounds determined from the reaction kinematics and energetics for each of these products. Also the profiles

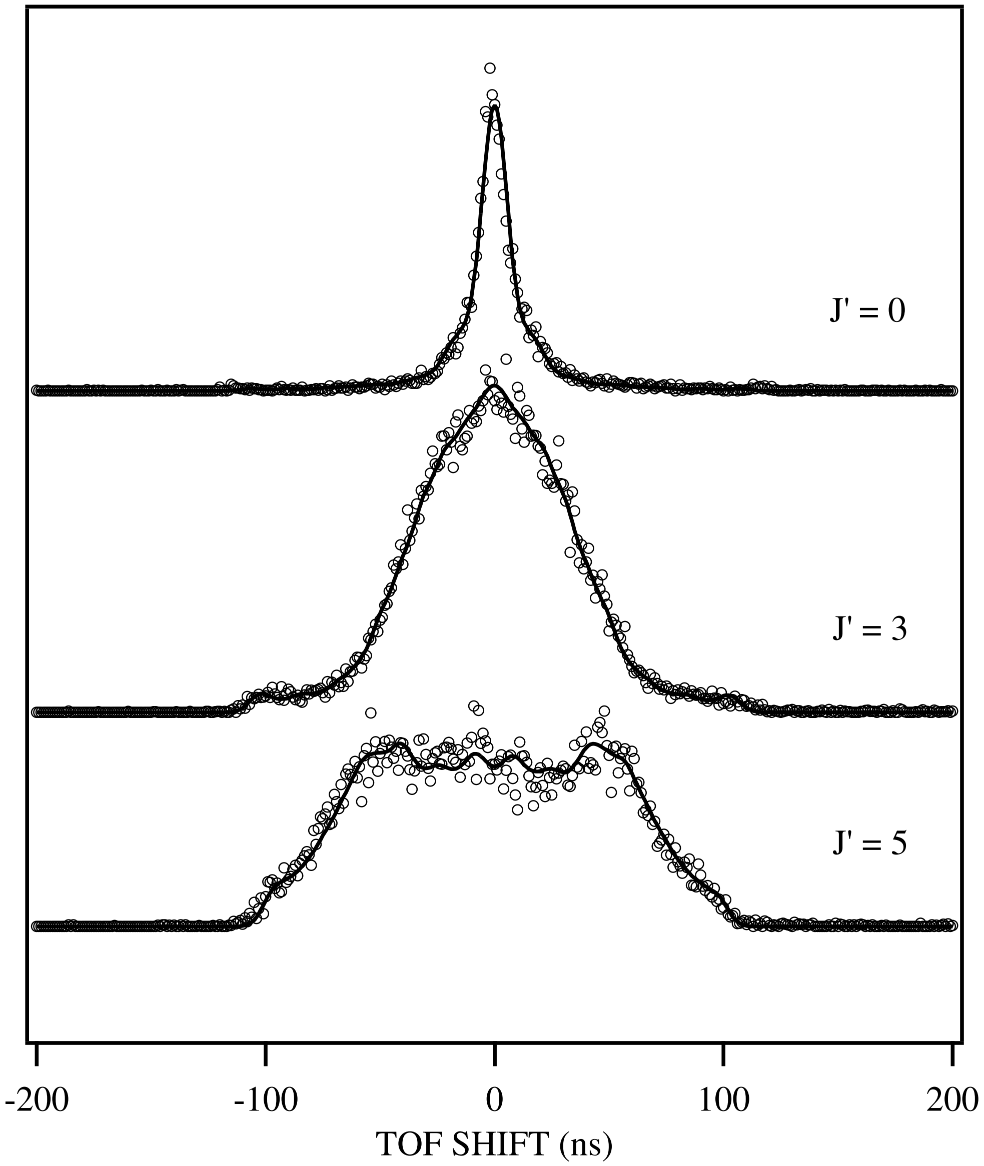


Figure 8.3: Core-extracted time-of-flight profiles for HD($v' = 2, J'$) products at collision energies ca. 1.55 eV. HD detection was accomplished by (2+1) REMPI through the Q-branch members of the HD EF $^1\Sigma_g^+ \leftarrow$ X $^1\Sigma_g^+$ (0,2) band. The solid lines are the result of a fit to the experimental profiles using the basis function generation and least-squares methods described in the text.

show a large degree of symmetry about their center. In general, distortions in the velocity distributions caused by space-charge effects initially produce a decrease of the signal arising from the late-arriving ions (i.e., signal with a positive time-of-flight shift). As the background ion production is increased, we observe an overall decrease of the ion signal but more so for those ions that spend more time in the extraction region. After a certain laser power threshold, half of the profile, corresponding to the late-arriving ions, completely disappears and only a single compressed ion peak arriving at earlier times is discernible. The shift in the arrival time is small compared to the total flight time but of a sufficient magnitude to be clearly observable. We believe this peak arises from those ions that managed to escape the highly congested extraction region, receiving an overall extra push toward the detector by the large number of positive ions left behind, which naturally translates into an earlier arrival time.

The extraction voltages used to collect the signals shown in Fig. 8.3 are also the lowest compatible with measurable signal levels. They correspond to electric field strengths of 20 V/cm (50-V voltage drop across the 0.9-inch long extraction region). The use of low extraction voltages has two beneficial consequences. First, it increases the velocity resolution of the instrument to a degree for which it is possible to use a relatively large number of single-speed basis functions for the linear least-squares fitting of the signal. Second, low extraction voltages allow the ion cloud to expand as much as possible as it travels along the detection axis, making the measured profile less susceptible to shape changes caused by improper centering of the ion packet onto the core extractor. Obviously, the greatest limitation in the core extraction technique is the steep drop in the number of ions that make it through the core extractor. As the extraction voltage is lowered, the observed signal decreases approximately as the cube of the applied extraction voltage. Fortunately, the use of the very sensitive (2+1) REMPI scheme for HD($v'$, $J'$) detection in conjunction with relatively long collection times enables us to use the Wiley-McLaren time-of-flight spectrometer at a resolution very close to the maximum one currently attainable with our experimental setup, i.e., other blurring factors such as laser pulse duration become predominant at this point.

Because the laboratory speed range for all three states is quite similar (cf. Table 8.2), any differences in the shape of the profiles shown in Fig. 8.3 are directly attributable to differences in the center-of-mass angular distributions. It is quite fulfilling to be able to discern so clearly these differences directly from the core-extracted time-of-flight profiles without recourse to further analysis of the experimental signals. For example, the laboratory speed distribution for $\mathrm{HD(v'=2, J'=0)}$ is extremely narrow and centered around zero. Thus, the center-of-mass angular distribution must be preferentially backward scattered. As we move to $\mathrm{J'} = 3$ and $\mathrm{J'} = 5$ the velocity distributions become wider and flatter, which indicates that scattering becomes more sideways.

The solid lines accompanying each profile in Fig. 8.3 are the result of a singular-value decomposition fit [243] to the signal using twelve evenly-spaced velocity basis functions. It was very encouraging to find that our instrumental parameters, as described in Chapter 5, could be used without further modification to fit the signals presented here. The core-extracted time-of-flight profile for $\mathrm{HD(v'=2, J'=0)}$ is extremely narrow. As such, it can be regarded as a good testing ground of the accuracy of the single-speed velocity basis functions generated via the Monte-Carlo simulation of the instrument. It was quite reassuring to find that our description of the instrument function could faithfully account for the width and shape of this distribution without any adjustments. For example, overestimation of the instrument function by our calibration procedures would have made it extremely difficult to fit this profile properly. In this case, the width and height of the profile is caused by a very small range of laboratory speeds and therefore spurious cancellations of nearby and partially overlapping velocity basis functions cannot account for its features to the degree shown in Fig. 8.3.

Examination of the covariance matrix from the linear least-squares fit to the signal suggests that it is possible to use between 13 and 15 basis functions before there is significant covariance between adjacent velocity basis functions. We have chosen to adopt a more conservative approach and only use the number of basis functions that our knowledge of the instrument function prescribes. This number of basis functions is between 12 and 13 and leads to an angular resolution of about $3^{\mathrm{o}}$ for backward scattering and about 13$^o$ for forward scattering.

Figure 8.4 shows the angular distributions derived from the core-extracted time-of-flight profiles of Fig. 8.3. Twelve points span the whole center-of-mass angular range. The error bars for each point represent the $1\sigma$ uncertainty associated with random (Poisson) and reproducibility errors obtained from at least five measurements of each rovibrational state. We should stress the fact that these error bars are therefore a direct measure of our ability to measure these angular distributions repeatedly with our instrument as opposed to just providing the error or variance associated with a single fit to the signal.

As Fig. 8.4 shows, there is a clear and systematic change in the peak and breadth of the angular distributions as the rotational energy of the product increases. For $\mathrm{HD(v'=2, J'=0)}$ the differential cross section is stronly peaked in the backward direction. For $\mathrm{HD(v'=2, J'=3)}$ the peak of the distribution has shifted to $\sim 144^o$ and a wider range of angles around this value contribute to product scattering. Finally, for $\mathrm{HD(v'=2, J'=5)}$, the most probable scattering angle has moved to $\sim 115^o$ and a sizable amount of scattering occurs over much of the angular range.

### 8.3.3 Discussion and Comparison with Other Work

Comparison of the present set of angular distributions with the $\mathrm{HD(v'=1, J')}$ measurements described in Section 8.2 shows the same overall trends with product rotational quantum number. Specifically, we find strong backscattering for low J' and a gradual shift of the angular distribution toward smaller angles with increased product rotational quantum number.

Lack of theoretical calculations for this reaction system at our collision energies precludes us at this point from a direct comparison with either quantum mechanical or quasiclassical calculations. We hope these measurements will be put to test against the most accurate calculations for the $\mathrm{H + D_2}$ reaction system including effects such as the Geometric Phase. As predicted by Kuppermann and co-workers [85, 86, 321, 344, 372–375] our collision energies should be sufficiently high to observe the effects of this phenomenon, specially if comparison between if theory and experiment is possible

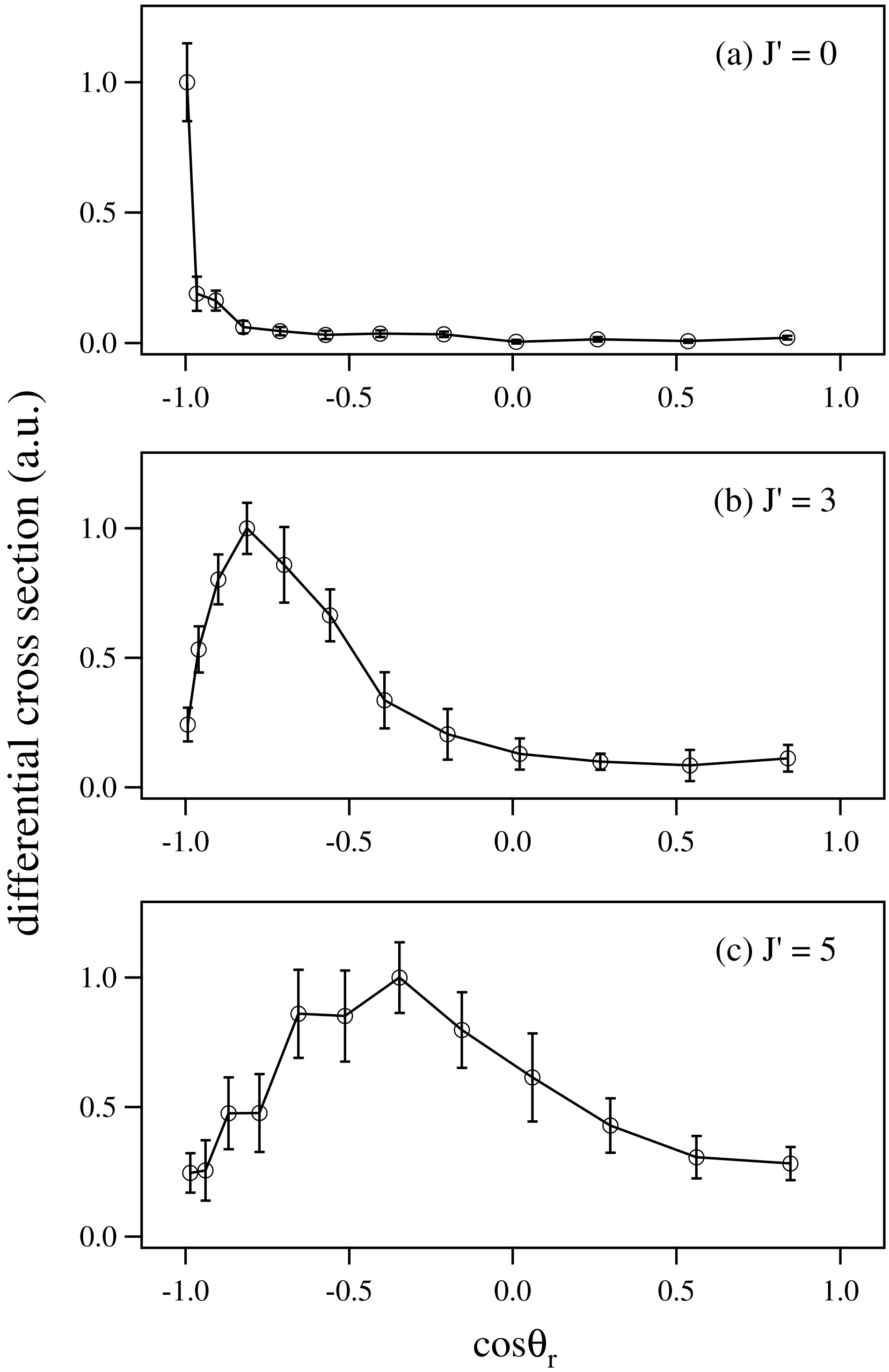


Figure 8.4: Angular distributions derived from the core-extracted time-of-flight profiles shown in Fig. 8.3. The solid lines are guides to the eye. Error bars are $1\sigma$ and they include both random and systematic errors in the measurements.

at the level of rovibrationally state-resolved differential cross sections. The question remains open, however, as to whether our differential cross section measurements are sensitive to these effects.

Moreover, it is of interest to compare our differential cross sections to those reported at different collision energies. The state-resolved angular distributions of Schnieder et al. [340] at 1.28 eV for the same internal states show a similar dependence of the angular distribution with product rotational quantum number. For this lower collision energy, the angular distributions peak at $\sim 170 - 180^{\circ}$ for $\mathrm{J}' = 0$, $\sim 140^{\circ}$ for $\mathrm{J}' = 3$, and $\sim 120^{\circ}$ for $\mathrm{J}' = 5$. However, the differential cross section for $\mathrm{J}' = 0$ in the work of Schnieder et al. [340] at 1.28 eV shows a broader range of angles, extending down to $\sim 120^{\circ}$, than we have observed. Similarly, recent measurements by the same group at 2.20 eV [368] show angular distributions peaking at $\sim 180^{\circ}$ for $\mathrm{HD}(\mathrm{v}' = 2, \mathrm{J}' = 0)$, $\sim 150^{\circ}$ for $\mathrm{HD}(\mathrm{v}' = 2, \mathrm{J}' = 3)$, and $\sim 115^{\circ}$ for $\mathrm{HD}(\mathrm{v}' = 2, \mathrm{J}' = 6)$. The experimental differential cross section for $\mathrm{HD}(\mathrm{v}' = 2, \mathrm{J}' = 3)$ at this collision energy of 2.20 eV, however, shows a clear additional local maximum at $\sim 180^{\circ}$, similar to the one we found for $\mathrm{HD}(\mathrm{v}' = 1, \mathrm{J}' = 5)$ at 1.70 eV. It thus seems that current experiments are sensitive to the fine details of the shape of the angular distributions and, as such, theory should be capable of reproducing these features. In conclusion, as much as rovibrationally state-resolved center-of-mass angular distributions at different collision energies can be compared, the same qualitative trends are found in the most recent experimental studies of this reaction.

# Chapter 9

# A Simple Model for $\mathbf{H + H_2}$ Dynamics

*We have to remember that what we observe is not nature in itself but nature exposed to our method of questioning.*

W. Heisenberg

## 9.1 Qualitative Remarks

In Chapters 7 and 8 we showed how the photoloc technique may be applied successfully to the measurement of both state-resolved integral and differential cross sections for the hydrogen-atom hydrogen-molecule exchange reaction. Before suggesting an interpretation of the results already described qualitatively, a few remarks on what is known about the nature of this reaction are in order.

An extensive amount of theoretical work, both classical and quantum mechanical, show that the hydrogen exchange reaction is direct in character [5, 376, 377], although computations [47, 72, 79, 378–380] have provided some evidence for the possibility of more complicated behavior, such as complex formation and scattering resonances.

Very simple physical considerations can shed some light onto the claim that this reaction is direct in character. The H atom and, in our case, the $D_2$ molecule are "small," with van der Waals radii on the order of $a_o$ ($a_o = 0.529$ Å). Using $a_o$ as the "characteristic" collision radius for the $H + D_2$ reaction, we can arrive at a cross section of $\pi a_o^2 = 0.9$ Å$^2$, a value reasonably close to the calculated and measured reactive cross sections at the collision energies of our experiments which are well above threshold. Of course, this simple estimate does not capture the inherent collision energy dependence of the reaction cross section which is quite steep at low collision energies, but at least it predicts the right order of magnitude in regard to the nature of the collision ultimately leading to the reactive event. Such a small cross section also implies a small and narrow range of impact parameters leading to reaction, usually on the order of $b = 1 - 2\ a_o$. These impact parameters correspond to values of the initial orbital angular momentum at our collision energies of

$$L = \frac{\mu v_{rel} b}{\hbar} = 10 - 20 \tag{9.1}$$

Next, we consider the timescales of the various molecular motions involved in the reaction. This is necessary because under our experimental conditions there is a mixture of $D_2(v = 0, J = 0, 1, 2)$ levels. The classical rotational period of a diatomic molecule is given by the following expression

$$t_{rot} = \frac{\hbar}{J \cdot B_{rot}}, \tag{9.2}$$

where J is the rotational quantum number and $B_{rot}$ is the rotational constant (in energy units) of the diatomic molecule. For $D_2(v = 0, J = 1)$ this amounts to approximately 170 fs. This timescale is in contrast with the classical vibrational period of 4 fs given by

$$t_{vib} = \frac{1}{\omega_{vib}}, \tag{9.3}$$

where $\omega_{vib}$ is the vibrational frequency of the diatomic bond expressed in Hz. Similarly, the characteristic collision time as estimated from

$$t_{coll} = \frac{a_o}{v_{rel}}, \tag{9.4}$$

where $a_o$ is the Bohr radius defined above and taken to be approximately the range of the interparticle potential; $v_{rel}$ is the relative velocity of the reagents. For collision energies of 1.7 eV, this time is approximately 4 fs. Therefore, the disparity of the timescales for rotational motion versus vibrational and translational motion allows us to treat, to a large degree of confidence, this degree of freedom as frozen or adiabatic during the reactive event. In other words, rotational effects arising from reorientation of the reagent of the collision can be ruled out. It is thus expected that the distribution of rotational levels in the $D_2(v = 0)$ reagent inherent in our experiments has little effect on the measured integral and differential cross sections. This claim is further substantiated by quasiclassical trajectory calculations performed by Aoiz et al. [381] for the $H + D_2$ reaction at 1.29 eV. We should point out that for collision energies approaching the reaction threshold this behavior no longer would hold, as shown by calculations by Aoiz et al. [381, 382], and Mielke, Truhlar, and Schwenke [383].

The most accurate *ab initio* calculations of the $H_3$ potential energy surface show a large energy dependence on the angle of attack, $\gamma$, of the incoming atom. This "angle of attack" is also related to the bending motion of the $H_3$. In fact, most of the resonance behavior observed in theoretical studies for this reaction arises from reactive trajectories accessing these bending modes for short periods of time. We define $\gamma$ as the $H - D - D$ angle that becomes zero when the approach of the H atom is collinear with the $D_2$ bond axis. The barrier height for reaction changes from 0.4 eV for collinear approach to 2.0 eV [61, 62] for a geometry where the hydrogen atom approaches a given D atom from the "wrong" side, corresponding to an angle of attack of roughly 110°. This angle-dependent barrier to reaction may be obtained from the LSTH potential energy surface and has been given by several authors [61, 377, 384]. For the purpose of the calculations presented later in this chapter we have fitted the LSTH angle-dependent reaction barrier to a second-order polynomial in $\cos\gamma$ of the form

$$V_b = V_b^0 + V_b^2 \cos\gamma + V_b^2 \cos^2\gamma \tag{9.5}$$

where $\gamma$ has been defined previously, and the parameters $V_b^0 = 1.32$ eV, $V_b^1 =$

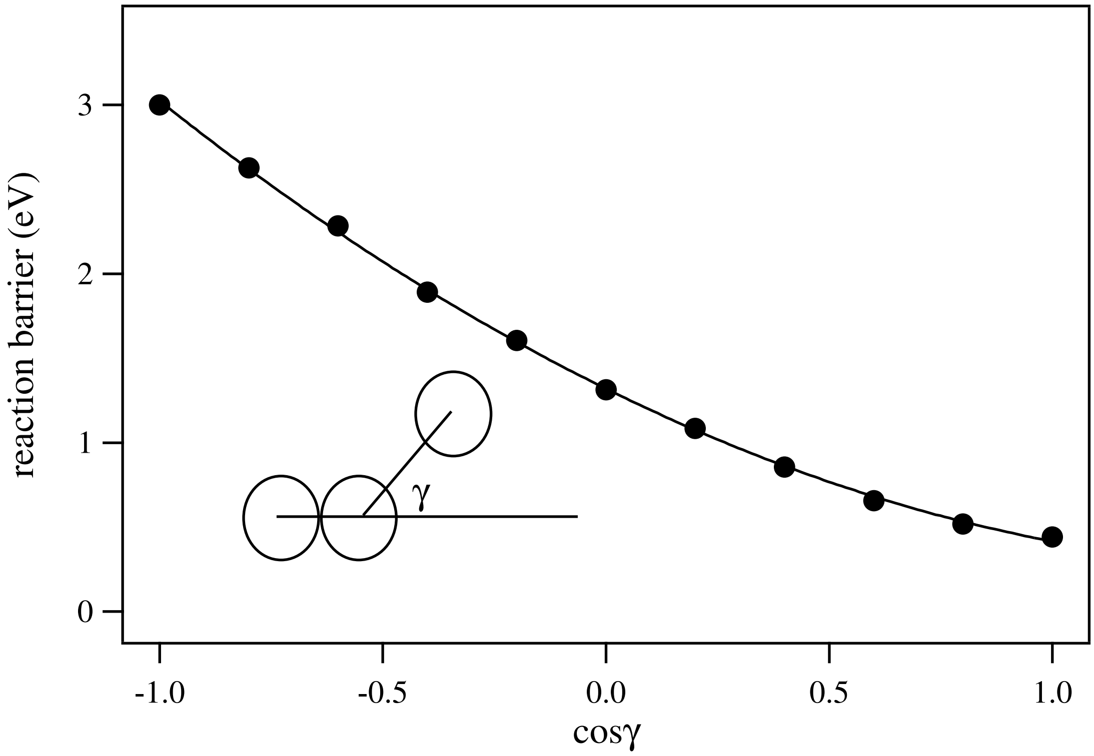


Figure 9.1: Angle-dependent barrier for the $\mathrm{H} + \mathrm{H_2}$ reaction.

$-1.30$ eV, and $\mathrm{V_b^2} = 0.40$ eV are obtained from a least-squares polynomial fit to the *ab initio* points. Fig. 9.1 shows the corresponding plot of this angle-dependent barrier.

From these considerations it can be expected that there is large preference for those trajectories that approach a collinear geometry to react. The steep dependence of the potential energy with angle $\gamma$ ensure that even at collision energies as high as 1.5-2.0 eV we can still expect to see its manifestation in measured observables such as angular distributions. Also, and as we will discuss in more detail later, this preference for a collinear geometry is especially true for those collisions at large impact parameters where there is less energy energy along the line of centers to surmount the barrier to reaction. In this case a smaller range of transition state geometries can therefore contribute to reactive flux.

## 9.2 Development of the Model

We note that both the timescales presented in the previous section, which allowed us to assess the relevance of various molecular motions during the collision process, as well as the barrier energetics are solely related to the entrance-channel properties of this reactive system. At no point during this discusion we have worried about what happens during (transition state) or after (exit-channel dynamics) the reactive event. We will next consider whether a model that only incorporates the characteristics of the entrance channel to reaction can account for the observed trends in the integral and differential cross section measurements.

To this end, we start with the simplest extension of the optical model to reactive scattering [385–391]. We begin by writing the total scattering angle, $\theta_{\mathrm{r}}$, for the reactive product as the sum of reactant and product contributions, both governed by potentials of two-body type. This last restriction ensures that the deflection function can only depend on initial impact parameter and collision energy and requires further justification. The intermolecular potential between the hydrogen atom and the hydrogen molecule has been measured experimentally [60, 392] and has been analyzed by Tang and Toennies [393] and by Partridge et al. [394] using a combination of theoretical and experimental data. Such a potential deviates little from a radial potential interaction and the onset of “chemical forces” is located on the repulsive part of the intermolecular potential [395, 396].

Because it is customary to define $\theta_{\mathrm{r}}$ as the angle between the initial and final relative velocity vectors, the relationship between the product scattering angle in the center-of-mass frame and the reactant and product deflection angles can be written as

$$\theta_r = \pi - [\theta(b, E_T)_{react} + \theta(b', E'_T)_{prod}] \tag{9.6}$$

where we have explicitly written the dependence of the deflection angles $\theta_{\mathrm{react}}$ and $\theta_{\mathrm{prod}}$ on impact parameter b and relative translational energy $\mathrm{E_T}$. The translational energy dependence may be removed if $\theta_{\mathrm{react}}$ and $\theta_{\mathrm{prod}}$ are assumed to follow hard-sphere scattering. If this hard-sphere scattering assumption holds, then the relationship between entrance and exit angles and their corresponding impact parameters is simply given by

$$\sin \theta_{react} = \frac{b}{d} \tag{9.7}$$

$$\sin \theta_{prod} = \frac{b'}{d'} \tag{9.8}$$

where d and d′ are the hard-sphere radii characterizing the interaction between reagents and products respectively.

In the $H + D_2$ reaction, the reactant and product channels are expected to have a very similar hard-sphere diameter, i.e., d ≈ d′, and a very similar (small) range of impact parameters. All these approximations, however crude they may seem, lead to the celebrated "specular" reflection approximation whereby

$$\theta_r = \pi - 2 \arcsin \left( \frac{b}{d} \right) \tag{9.9}$$

or written in a more useful form for our purposes

$$\cos \theta_r = 2 \frac{b^2}{d^2} - 1 \tag{9.10}$$

Clearly, the one-to-one correlation between impact parameter and scattering angle invoked above in Eqs. (9.7) and (9.8) is generally invalid for reactive scattering. The expression for the total scattering angle shown by Eq. (9.6) reflects the "ultra-direct" character of the process in question and this limitation should be kept in mind throughout this discussion. For instance, if the chemical reaction proceeds via the formation of a long-lived complex the products have no way of "remembering" the initial conditions and such an approximation should fail completely. However, for direct reactions taking place via a linear complex one can show that there exists a one-to-one relationship between b and b′. Other geometries of the transition state lead to a distribution of b′ values for each initial b with an average value approaching the linear limit [390]. Thus, for chemical reactions in which the reaction complex is short-lived and its geometry is preferentially collinear such limit can still be qualitatively approached. Similar arguments to the ones presented here have been used by Kwei and Herschbach [397] to predict product total angular distributions.

We first examine under these considerations the $\mathrm{HD}(\mathrm{v}' = 1, \mathrm{J}')$ differential cross section data presented in Section 8.2. Eq. (9.10) relates an initial impact parameter leading to reaction with a product scattering angle in such a manner that small-impact-parameter collisions lead to complete product backward-scattering. The experimental data shows a clear correlation between low-J′ product states and backward scattering. As the rotational quantum number of the product increases, the distributions become more sideways and broader. These trends suggest that low-J′ product states correlate with reactive collisions at small impact parameters and high-J′ states with large impact parameters. Classically, this correspondence between low-J′ states and backward scattering is easy to picture by taking into account the collinear character of the minimum energy path in the potential energy surface. For b=0, reactive collisions are preferentially head-on and of a rebound character. Consequently, little torque is imparted on the emerging HD product. As b increases, the collision becomes more glancing, but the preferred geometry for the switchover between reagents and products is even more strongly collinear. In this situation some of the initial translational energy is converted into rotational energy of the product, i.e., the H-D-D axis is not parallel to the incoming relative velocity vector at the point where reaction takes place. Figure 9.2 shows a ball-and-stick pictorial representation of these ideas. This figure emphasizes the fact that for large impact parameters the range of reactive geometries is more constrained than for collisions at zero impact parameter because the available energy along the line-of-centers, namely $\mathrm{E_T}(1 - \frac{\mathrm{b}^2}{\mathrm{d}^2})$, decreases as b increases. More explicity, the presence of an energy barrier of at least 0.41 eV along the minimum energy path allows us to write the following expression for the maximum impact parameter energetically accessible

$$b_{max} = d \cdot \left(1 - \frac{E_0}{E_T}\right)^{\frac{1}{2}} \tag{9.11}$$

where $\mathrm{E_0}$ is the minimum energy barrier and $\mathrm{E_T}$ is the total energy available. Beyond this value, not sufficient energy exists to cross the reaction barrier. The implications of this expression will become clear once we examine the state-to-state angular distributions.

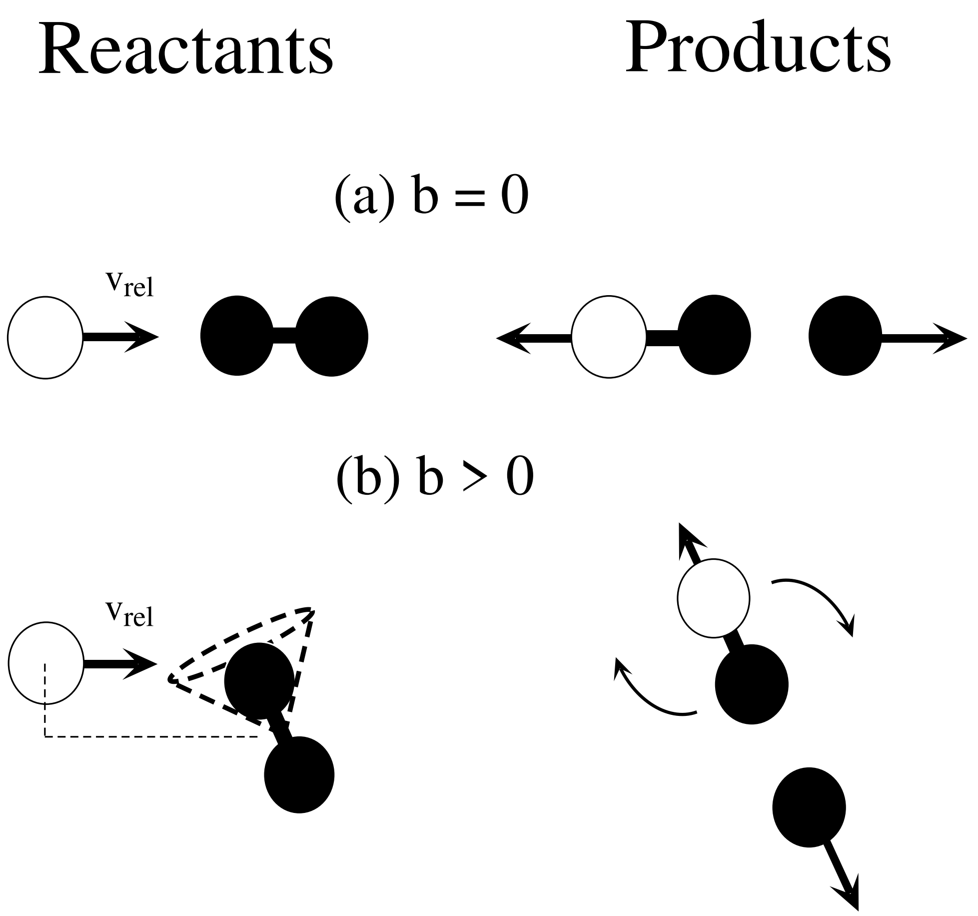


Figure 9.2: Pictorial representation of the relationship between reactive impact parameter b and product rotational angular momentum J′. Panel (a) shows a zero-impact-parameter collision leading to rotationally cold, backscattered product. Panel (b) shows a large impact parameter collision leading to more rotational excitation and smaller, more side-scattered angles. Panel (b) also includes an approximate "cone of acceptance" for collisions leading to reactive product. The larger impact parameter necessarily implies a smaller amount of energy to surmount the angle-dependent barrier. Consequently, a narrower range of transition state geometries is energetically available.

This simplistic and inherently classical picture for the dependence of the differential cross section on product rotation can be further refined if we consider the correlation between the initial and final angular momenta of a generic A + BC reactive system, and incorporate in a semiquantitative manner kinematic and energetic constraints. As Gordon et al. [398, 399] have argued, activated and direct reactions generally display a correlation between the initial orbital angular momentum $\vec{\mathrm{L}}$ and the rotational angular momentum of the product $\vec{\mathrm{J}}'$ of the form

$$\vec{J'} = \alpha \cdot \vec{L} + ... \tag{9.12}$$

This expression is reminiscent of the well-known kinematic effect displayed by reactions of the type H + HL → HH + L where the mass combination in conjunction with conservation of angular momentum imply a complete conversion of initial orbital angular momentum into rotation of the HH product in the limit of H/L → ∞ [400–405]. The implications of this expression are more profound than what one may suspect at first sight. Eq. (9.12) tells us that a rotational distribution as the ones we have measured can be used to derive a coarse opacity function for reaction for each product vibrational level. In our case, we can use a similar line of thought and postulate that if the deflection function follows hard-sphere, specular scattering as shown before in Eq. (9.10) then we can examine, at least qualitatively, the J′ dependence of the opacity function for this reaction. More explicitly, we can show that if Eq. (9.10) can faithfully represent the deflection function, then the relationship between the opacity function, P(b), and the product angular distribution is given by

$$\frac{\partial \sigma}{\partial \cos\theta_r} = 2\pi b P(b) \frac{\partial b}{\partial \cos\theta_r} = P(b)\left(\frac{\pi d^2}{2}\right) \tag{9.13}$$

## 9.3 Analysis of Angular Distributions

Table 9.1 shows a summary of the angular distributions described in Chapter 8. As the last column shows, both vibrational manifolds behave in a very similar fashion, namely, there is backward scattering for low-J′ states and the most probable value of the scattering angle shifts to smaller angles as the rotational excitation of the product

| Collision energy (eV) | Vibrational level v′ | Rotational level J′ | Total Internal energy (eV) | MP scattering angle (degrees) |
|---|---|---|---|---|
| 1.71 | 1 | 1 | 0.694 | 170 |
| 1.70 | 1 | 5 | 0.839 | 133 |
| 1.66 | 1 | 8 | 1.047 | 100 |
| 1.56 | 2 | 0 | 1.109 | 175 |
| 1.55 | 2 | 3 | 1.169 | 144 |
| 1.53 | 2 | 5 | 1.257 | 115 |

Table 9.1: Summary of HD(v′, J′) product states probed to present.

increases. It is worthwhile noting the insensitivity of the angular distributions to the total internal energy of the product. Rows three and four of this table belong to two states which are almost isoenergetic yet the most probable scattering angles are very different for the HD($v' = 1$) and HD($v' = 2$) product states. From an experimental viewpoint, we also note that these two states would be very hard to resolve if we chose to detect the atomic fragment instead of the diatomic product since their energies are only tens of meV apart.

To put these qualitative observations on a firmer ground, we can test the validity of the proposed correlation between the magnitude of $J'$ and impact parameter b within the context of the model presented in the previous section. For this purpose we have plotted in Fig. 9.3a the most probable value of the scattering angle for the angular distributions of Chapter 8 as a function of $J'^2$. We plot the data in this manner because if there exists both a correlation between initial orbital and final rotational angular momentum and the deflection is of a hard-sphere type, then Eq. (9.10) holds and the points fall on a straight line. From a linear fit of these points we can obtain the scaling of the reduced impact parameter with $J'$ for each particular manifold. Figure 9.3b also shows a plot of the scattering angle as function of reduced impact parameter $b_{red} = b/d$. The straight line shows the hard-sphere functional form, whereas the points belong to the experimental angular distributions

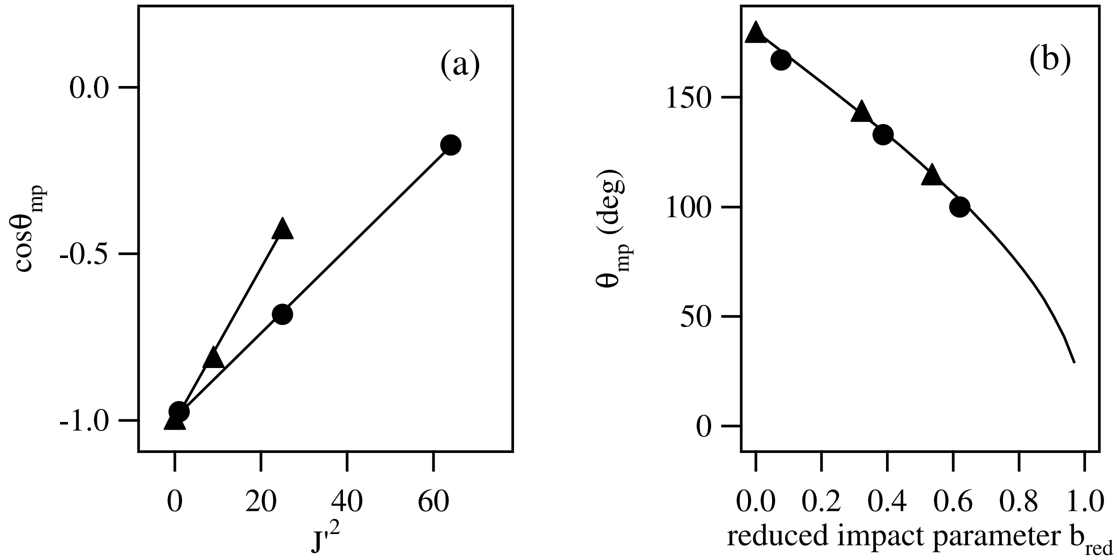


Figure 9.3: (a) Correlation between the most probable scattering angle and product rotational angular momentum. Circles correspond to HD(v$'$ = 1) and triangles to HD(v$'$ = 2). Note the different slopes indicative of a different hard-sphere radius for each vibrational manifold. (b) Relationship between scattering angle and reduced impact parameter $b_{red}$ deduced from the correlation shown in (a). The solid line represents the hard-sphere limit, given by Eq. (9.10).

The most salient feature of this analysis is that each vibrational manifold displays a linear correlation independently. That is, the slope of the linear fit to the points in Fig. 9.3 varies with product vibrational excitation. The most probable scattering angle decreases at a faster rate for $v' = 2$ vs $v' = 1$ products. Because $b_{red} = b/d$, we are led to interpret this result as arising from a smaller hard sphere radius d for $v' = 2$ vs $v' = 1$ product. This result is not surprising in view of the fact that vibrational excitation of the product is more probable for small impact parameters, i.e., conversion of initial translational energy into vibrational energy of the product is more facile. This finding implies that the opacity function leading to vibrationally excited product has an earlier cutoff for products with increased vibrational energy.

We can further investigate the behavior of the angular distributions by considering the cutoff in the impact parameter caused by the energetic constraints of the reaction (cf. Eq. (9.11)). Whereas we have found that the reduced impact parameter

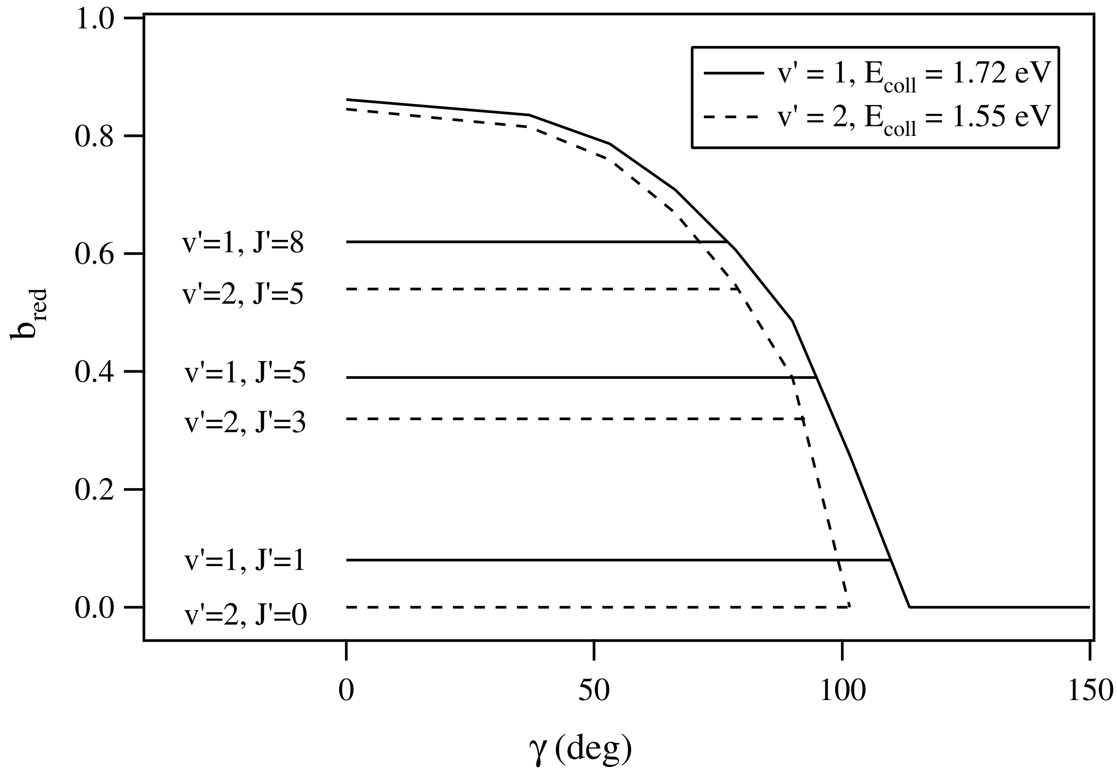


Figure 9.4: Reduced impact parameter $b_{red}$ vs maximum angle of attack $\gamma$ taking into account the energy-dependent barrier to reaction (See text for a more detailed discussion). Each horizontal line represents a given HD rovibrational state. From the figure it is clear that each vibrational manifold converges to a different maximum rotational quantum number for $b_{red}^{max}$, namely $J' = 11$ for $v' = 1$, and $J' = 8$ for $v' = 2$.

and most probable scattering angles are correlated, there should be a cutoff beyond which there is not sufficient energy to surmount the barrier to reaction. This reduced impact parameter is readily calculated from the lowest barrier to reaction by the use of Eq. (9.11). With our empirical correlation between impact parameter and rotational quantum number we should therefore be able to predict the maximally allowed rotational quantum number accessible by this proposed direct reaction mechanism. In Fig. 9.4 we have plotted the reduced impact parameter vs the maximally energetically allowed angle of approach $\gamma$. Shown with solid and dashed lines are the two rotational progressions for each vibrational manifold. Despite the minor collision energy differences between the two sets of measurements, the maximum reduced impact parameter is ca. 0.85 for both vibrational states. From these progressions we can predict maximum rotational quantum numbers of $\mathrm{J}' = 11$ for $\mathrm{v}' = 1$ and $\mathrm{J}' = 8$ for $\mathrm{v}' = 2$. This figure brings out another important point regarding the dynamics of this reaction. The range of angles of attack decreases with increasing rotational excitation of the product. For low-$\mathrm{J}'$ states insertion trajectories can lead to reaction whereas for high-$\mathrm{J}'$ states this is less likely. Therefore, one should expect more interesting behavior for the low-$\mathrm{J}'$ states. Indeed, quantum mechanical scattering calculations [344, 368] show forward-scattering peaks in the differential cross section for low-$\mathrm{J}'$ states, an indication that dynamics involving reaction complexes is restricted to those collisions at low impact parameters.

## 9.4 Connection with Rotational Distributions

The analysis of the angular distributions under the assumptions of a direct model for reaction was capable of making definite predictions about the cutoff of the rotational distributions. We are now in a position to relate the features of the differential cross sections to the rotational distributions presented in Chapter 7.

To make the discussion a little more quantitative, we would also like to have a means of predicting not only the cutoff but also the approximate shape of the rotational distributions without introducing too many unjustified assumptions. Since we have already established that product rotation is correlated with initial impact parameter, knowledge of the opacity function for reaction should be sufficient to predict the shape of the product rotational distribution. Determination of the opacity function, however, requires a full scattering calculation and will not be pursued here. Instead, we will assume the simplest functional form consistent with the notion that collision events will be more reactive the more energy is available to break the D-D chemical bond, that is, zero-impact parameter collisions are the most reactive. With this assumption, the opacity function for a given vibrational level is given by

$$P_v(b) = C_v \left(1 - \frac{b}{b_{max}}\right) \tag{9.14}$$

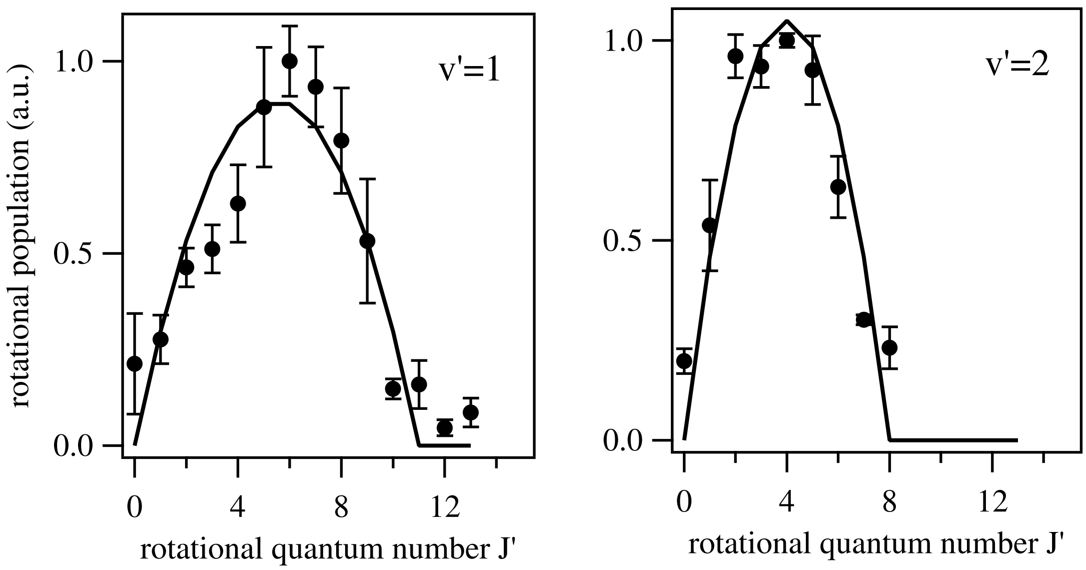


Figure 9.5: Comparison of measured rotational distributions with the functional form shown by Eq. (9.15). The maximum rotational quantum number is that obtained from the progression of the angular distributions.

where $C_v$ is a constant depending on the product vibrational manifold and other features of the dynamical process leading to reaction, and $b_{max}$ is the maximum reactive impact parameter. With this opacity function, and taking into account a correlation of the type b $\alpha$ J$'$, the rotational distribution into a particular vibrational level is simply given by

$$P_v(J') \sim J' \left(1 - \frac{J'}{J'_{max}}\right) \tag{9.15}$$

where $J'_{max}$ is the maximum rotational quantum number as inferred from the analysis of the angular distributions presented in the previous section. Fig. 9.5 shows the measured rotational distributions plotted against those derived from Eq. (9.15). The agreement between the model and measured distributions is quite encouraging not only in regard to the cutoff of the rotational distributions but also in regard to their shape. This agreement suggests that the model initially put forth to explain the angular distributions is quite consistent with other experimental observables of this reaction. It also suggests that the use of the experimentally derived quantity $J'_{max}$

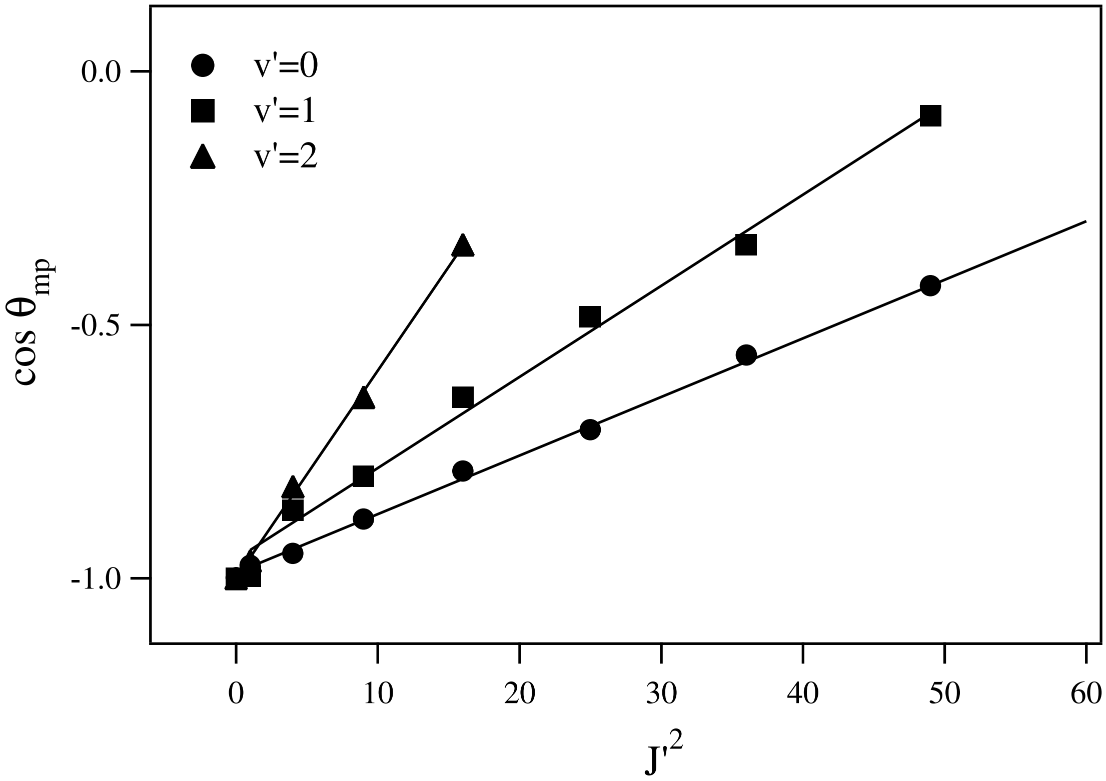


Figure 9.6: Correlation between the most probable scattering angle and product rotational angular momentum from the differential cross section measurements of Schnieder et al. at 1.29 eV.

as a reduced variable may help ellucidating and differentiating the proposed reaction mechanism against other possible ones.

## 9.5 Work at Other Collision Energies

State-resolved angular and integral cross section measurements have been already carried out at a collision energy of 1.29 eV by Schnieder and co-workers [340]. It is instructive to analyze this experimental data in the same way we have done for our measurements.

Figure 9.6 shows a plot of the most probable scattering angle vs rotational quantum number for the three vibrational states measured by Schnieder et al. This data

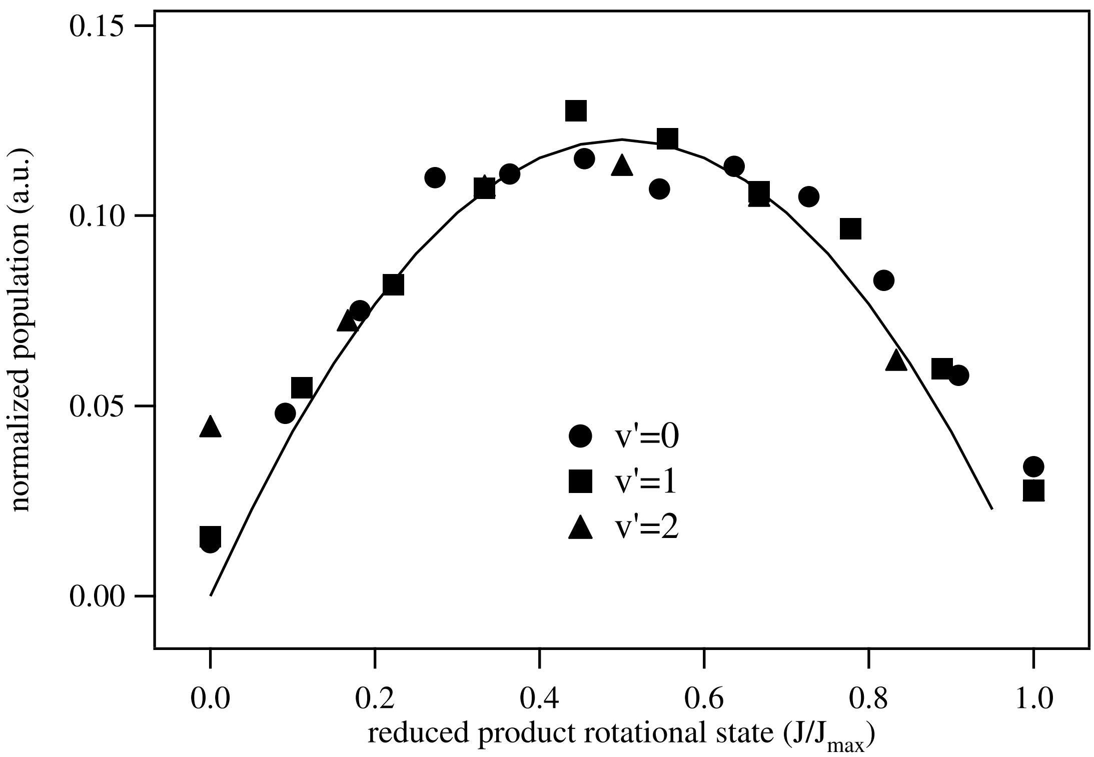


Figure 9.7: Normalized rotational distributions at 1.29 eV. $J_{max}$ has been obtained from the progression shown in Fig. 9.6.

shows the same trends with product rotation and vibration as we found previously, indicating that the same collision dynamics operates at this lower collision energy. Regarding the dependence of the most probable scattering angle with rotation, all the vibrational manifolds show a linear correlation between angle and the square of the product angular momentum, an indication that there is a linear relationship between impact parameter and product rotation. The dependence with vibrational quantum number is also the one expected from the requirement of smaller impact parameters leading to more vibrational excitation.

From the rotational progressions shown in Fig. 9.6 we can also extract the maximum rotational quantum number expected to be populated at this collision energy. Using this maximum rotational quantum number for each product vibrational state we can plot the rotational distributions against $J'/J'_{max}$. With the experimental data plotted in such a manner we should expect all vibrational manifolds to behave in an identical manner. In Fig. 9.7 we plot the experimental points for the three vibrational manifolds against the reduced rotational quantum number. Included in this figure is the model prediction based on Eq. (9.15). As the plot shows, the agreement is quite satisfactory. From this we conclude that the simple model introduced in this chapter is capable of accounting for the gross features of the experimental data gathered for this reaction system.

# Chapter 10

# Conclusions and Future Prospects

*A day will come in which zealous research over long periods of time will bring to light things that now still lie hidden. The life of a single man even if he devotes it entirely to the heavens, is insufficient to fathom so broad a field. Knowledge will thus unfold only over the course of generations. But there will come a time when our descendants will marvel that we did not know the things that seem so simple to them. Many discoveries are reserved for future centuries, however, when we are long forgotten. Our universe would be deplorably insignificant had it not offered every generation new problems. Nature does not surrender her secrets once and for all.*

*Seneca, "Naturales Quaestiones" (1$^{\text{st}}$ Century A. D.)*

The major aim of this thesis has been to show the possibility of performing state-resolved integral and, most importantly, differential cross section measurements for the hydrogen exchange reaction at well-defined collision energies. This goal has been accomplished by the utilization of the photoloc technique which allows quantum-state and angular-resolved cross section measurements via the utilization of laser photolysis for the initiation of the reaction and velocity-sensitive time-of-flight mass spectrometry for the measurement of the distribution of product laboratory speeds. We have gone at great lengths to describe the experimental procedures necessary for a successful application of this technique. These procedures include the calibration of the time-of-flight instrument as well as an exhaustive measurement of the reaction conditions. From these studies we concluded that the typical collision energy spread is at most 50 meV FWHM and the angular resolution in the differential cross sections varies from 3-5$^o$ for backward scattering to 12-15$^o$ for forward scattering. Furthermore, the simple relationship between the laboratory product velocity distribution and the center-of-mass differential cross section permits the full coverage of the center-of-mass angular range, in contrast with the partial angular coverage typical of crossed-beam experiments.

Both the integral and differential cross sections into particular rovibrational product states are consistent with a simple model that links the most probable scattering angle with product rotational angular momentum. Backward scattering is strongly correlated with low product rotational excitation and small reactive impact parameters. As the product rotational excitation increases, the angular distributions shift toward smaller angles in a manner consistent with hard-sphere specular scattering. The model allows for a straightforward analysis of the angular distributions. Its predictions regarding the cutoff and overall shape of the product rotational distributions are in good agreement with our experimental data. Experimental data by other groups at collision energies of 1.28 eV and 2.2 eV show the same overall trends in regard to the dependence of the angular distributions with product rotation. Attention is called for the need at the present time for accurate quantum mechanical scattering calculations to compare against our experiments.

There remains much to be done in this reaction system. In Fig. 10.1 we present preliminary time-of-flight profiles for the $\mathrm{H} + \mathrm{D}_2$ reaction at 1.55 eV detecting all the energetically accessible $\mathrm{HD}(\mathrm{v}' = 3, \mathrm{J}')$ product states. These experiments have been conducted with an independent HBr photolysis source and, therefore, the collision energy is the same for all states shown. In addition, this vibrational manifold can only be populated by the fast HBr photolysis. As such, it constitutes a very clean

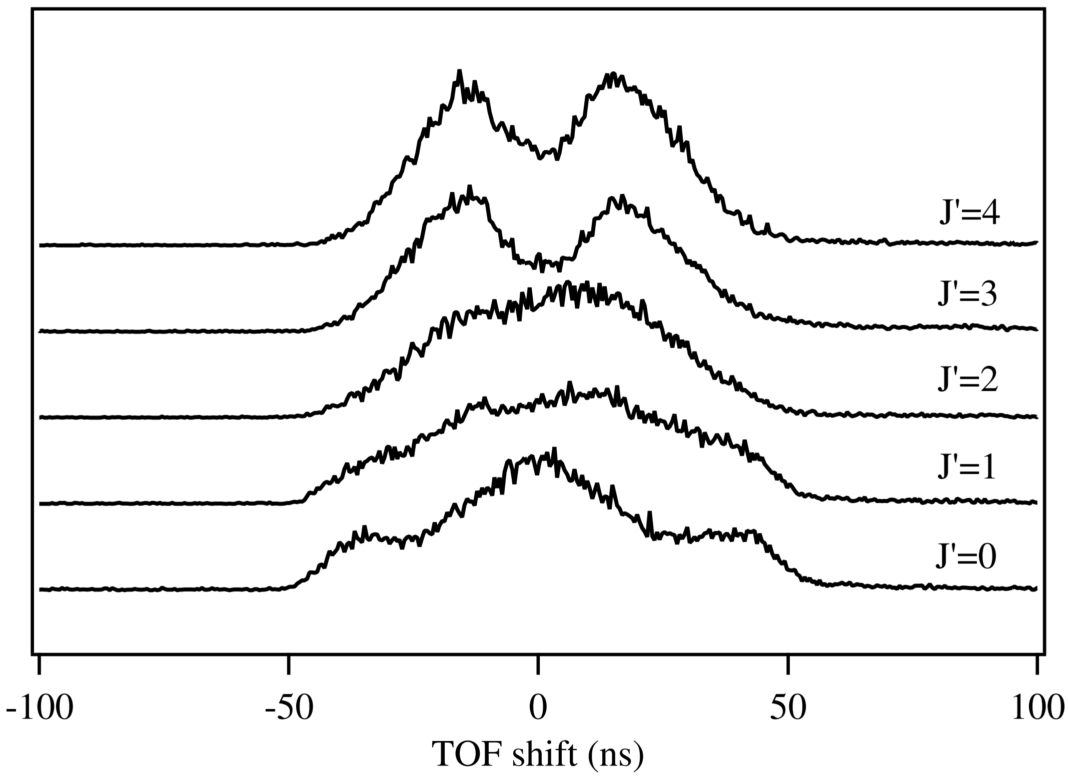


Figure 10.1: Core-extracted time-of-flight profiles for HD($v' = 3, J'$) products at 1.55 eV using an independent photolysis source.

measurement with no interference from other undesired reaction channels. The calculated reaction cross sections into these internal energy levels at these collision energies are about 0.001 $Å^2$, which translates into a sensitivity to reaction product into a given angular bin in the order of $0.0001 - 0.0002$ $Å^2$. Qualitatively, the progression from backward to sideways scattering with product rotation is also seen in the time-of-flight profiles of Fig. 10.1. There is even some evidence for forward scattering tails in the $J' = 0$ time-of-flight profile. The low signal levels from these product states precluded us from having much angular resolution (about 4-5 velocity basis functions) in these experiments. At this low resolution, it is difficult to perform a direct inversion of these profiles and be confident of the reliability of the angular distributions. Current efforts in our laboratory are being channeled into an improvement of the experimental conditions so that sufficient signal levels can be attained for these very-high internal energy levels of the reaction product.

Obvious extensions to the work presented in this thesis are to tune the collision energy and obtain detailed maps of state-resolved differential cross sections to be compared against theory. In particular, use of HI as a photolytic precursor will enable an increase in collision energy up to 2.2-2.3 eV using similar photolysis wavelengths. These measurements will provide a good ground for comparison with the experimental results of Schnieder and co-workers. Additionally, our current collision energy resolution allows us to tune the collision energy over small ranges and, at the same time, record state-resolved differential cross sections. It is currently believed that this is a very sensitive way to detect resonance behavior in this reaction.

The decade of the 80's marked the beginning of exhaustive experimental studies on the hydrogen exchange reaction. For about a decade it was generally thought it would be extremely hard, if not impossible, to measure anything beyond state-resolved integral cross sections. By the end of the 1990's, it has finally been possible to perform the first state-resolved diffferential cross section measurements. It would be unfair to believe this is the end of the story. The ability to pump the diatomic reagent using laser techniques would, for example, open a completely new direction in this reaction system. It would allow, for example, to assess the effect of reagent vibrational energy in the reaction dynamics. Moreover, the use of polarized laser radiation permits the alignment of the distribution of rotor axes in space, making feasible the study of steric effects. For this reaction system these effects are expected to be very large. Also, the use of laser spectroscopy may lead us beyond center-of-mass angular distributions and look at the product $(\mathrm{J}', \mathrm{M}')$ populations. In Chapter 4 we already hinted at this possibility when we presented spectra from a transition that is quite sensitive to the spatial anisotropy of angular momenta. Furthermore, the center-of-mass angular distributions of Chapter 8 and the model presented in Chapter 9 give us a hint about the magnitude of the product polarization for this reaction system. The correlation we found between product rotation and impact parameter has a vector nature associated with it, i.e., the impact parameter is proportional to the total initial angular momentum. As such, we expect to see a large correlation between the initial orbital and final product angular momenta, which implies that the product $\mathrm{J}'$ vector will be preferentially pointing in a direction perpendicular to the scattering plane. Aside from these predictions, the capability to measure the higher moments of the differential cross section will provide the experimentalist with a very powerful tool aimed at the ellucidation of the most intricate details of the most elementary reactive event. In this sense, the center-of-mass angular distributions presented here are just the beginning of a very long yet fruitful road.

# Bibliography


[1] H. Eyring, D. Henderson, and W. Jost, *Physical Chemistry. An Advanced Treatise* (Academic Press, New York, 1974), Vol. VIA.

[2] I. W. M. Smith, *Kinetics and Dynamics of Elementary Gas Reactions* (Butterworths, London, 1980).

[3] R. B. Bernstein, *Chemical Dynamics via Molecular Beams and Laser Techniques* (Oxford University Press, Oxford, 1982).

[4] J. Steinfeld, J. Francisco, and W. Hase, *Chemical Kinetics and Dynamics* (Prentice Hall, New Jersey, 1989).

[5] R. D. Levine and R. B. Bernstein, *Molecular Reaction Dynamics and Chemical Reactivity* (Oxford University Press, New York, 1989).

[6] S. Arrhenius, Z. Physik. Chem. **1**, 110 (1887).

[7] G. Scoles, *Atomic and Molecular Beam Methods* (Oxford University Press, New York, 1988), Vol. I and II.

[8] A. J. Alexander and R. N. Zare, J. Chem. Ed. **75**, 1105 (1998).

[9] A. H. Zewail, Science **242**, 1645 (1988).

[10] A. H. Zewail, *Femtochemistry: Ultrafast Dynamics of the Chemical Bond* (World Scientific, Singapore, 1994).

[11] M. Dantus, M. J. Rosker, and A. H. Zewail, J. Chem. Phys. **87**, 2395 (1987).

[12] M. D. M. J. Rosker and A. H. Zewail, J. Chem. Phys. **241**, 1200 (1988).

[13] A. H. Zewail, Faraday Discuss. Chem. Soc. **91**, 207 (1991).

[14] M. Dantus and G. Roberts, Comments At. Mol. Phys. **26**, 131 (1991).

[15] J. L. Magee, J. Chem. Phys. **8**, 687 (1940).

[16] J. J. Valentini, Y. T. Lee, and D. J. Auerbach, J. Chem. Phys. **67**, 4866 (1977).

[17] D. M. Neumark, A. M. Wodkte, G. N. Robinson, C. C. Hayden, and Y. T. Lee, J. Chem. Phys. **82**, 3045 (1985).

[18] D. M. Neumark, A. M. Wodkte, G. N. Robinson, C. C. Hayden, K. Shobatake, R. K. Sparks, T. P. Shafer, and Y. T. Lee, J. Chem. Phys. **82**, 3067 (1985).

[19] R. N. Zare and P. J. Dagdigian, Science **185**, 739 (1974).

[20] R. N. Zare, Ber. Bunsenges Phys. Chem. **86**, 422 (1982).

[21] H. J. Loesch, Ann. Rev. Phys. Chem. **46**, 555 (1994).

[22] R. N. Zare and R. B. Bernstein, Phys. Today **33**, 43 (1980).

[23] S. R. Leone, Ann. Rev. Phys. Chem. **35**, 109 (1984).

[24] R. N. Zare, Faraday Discuss. Chem. Soc. **82**, 391 (1986).

[25] B. L. van der Waerden, *Sources of Quantum Mechanics* (Dover, New York, 1968).

[26] J. Baggott, *The Meaning of Quantum Theory* (Oxford Science Publications, Oxford, 1992).

[27] F. London, Z. Elektrochem. **35**, 552 (1929).

[28] H. Eyring and M. Polanyi, Z. Phys. Chem. B **12**, 279 (1931).

[29] J. O. Hirschfelder, H. Eyring, and B. Topley, J. Chem. Phys. **4**, 170 (1936).

[30] J. O. Hirschfelder, Int. J. Quantum Chem. **3**, 17 (1969).

[31] S. Sato, J. Chem. Phys. **23**, 592 (1955).

[32] J. C. Polanyi and W. H. Wong, J. Chem. Phys. **51**, 1439 (1969).

[33] M. H. Mok and J. C. Polanyi, J. Chem. Phys. **51**, 1451 (1969).

[34] B. A. Hodgson and J. C. Polanyi, J. Chem. Phys. **55**, 4745 (1971).

[35] J. C. Polanyi, Acc. Chem. Res. **5**, 161 (1972).

[36] J. C. Polanyi, Science **236**, 680 (1987).

[37] D. G. Truhlar and R. E. Wyatt, Ann. Rev. Phys. Chem. **27**, 1 (1976).

[38] S. Datz and E. H. Taylor, J. Chem. Phys. **39**, 1896 (1963).

[39] J. Geddes, H. F. Krause, and W. L. Fite, J. Chem. Phys. **56**, 3298 (1972).

[40] J. O. Kaufman, Ann. Rev. Phys. Chem. **20**, 45 (1969).

[41] E. E. Marinero, C. T. Rettner, and R. N. Zare, J. Chem. Phys. **80**, 4142 (1984).

[42] D. P. Gerrity and J. J. Valentini, J. Chem. Phys. **79**, 5202 (1983).

[43] G. H. Kwei and V. W. S. Lo, J. Chem. Phys. **72**, 6265 (1980).

[44] R. Götting, H. R. Mayne, and J. P. Toennies, J. Chem. Phys. **85**, 6396 (1986).

[45] S. A. Buntin, C. F. Giese, and W. R. Gentry, J. Chem. Phys. **87**, 1443 (1987).

[46] R. E. Continetti, B. A. Balko, and Y. T. Lee, J. Chem. Phys. **93**, 5719 (1990).

[47] W. H. Miller, Ann. Rev. Phys. Chem. **41**, 245 (1990).

[48] H. Buchenau, J. P. Toennies, J. Arnold, and J. Wolfrum, Ber. Bunsenges. Phys. Chem. **94**, 1231 (1990).

[49] G. Herzberg, J. Chem. Phys. **70**, 4806 (1979).

[50] B. A. Collins, J. C. Polanyi, M. A. Smith, A. Stolow, and A. W. Tarr, Phys. Rev. Lett. **59**, 2551 (1987).

[51] R. Bruckmeier, C. Wunderlich, and H. Figger, Phys. Rev. Lett. **72**, 2550 (1994).

[52] D. Azinović and H. Figger, Z. Phys. D **42**, 105 (1997).

[53] D. Azinovic, R. Bruckmeier, C. Wunderlich, H. Figger, G. Theodorakopoulos, and I. D. Petsalakis, Phys. Rev. A **58**, 1115 (1998).

[54] S. Mahapatra and H. Köppel, Phys. Rev. Lett. **81**, 3116 (1998).

[55] S. Mahapatra and H. Köppel, J. Chem. Phys. **109**, 1721 (1998).

[56] P. C. Cosby and H. Helm, Phys. Rev. Lett. **61**, 298 (1988).

[57] U. Müller and P. C. Cosby, J. Chem. Phys. **105**, 3532 (1996).

[58] U. Müller and P. C. Cosby, Phys. Rev. A **59**, 3632 (1999).

[59] U. Müller, M. Beckert, M. Braun, and H. Helm, presented at the XVIII International Symposium on Molecular Beams, Ameland, The Netherlands, June 1999 (unpublished).

[60] D. G. Truhlar and R. E. Wyatt, Adv. Chem. Phys. **36**, 141 (1977).

[61] P. Siegbahn and B. Liu, J. Chem. Phys. **68**, 2457 (1978).

[62] D. G. Truhlar and C. J. Horowitz, J. Chem. Phys. **68**, 2466 (1978).

[63] G. C. Schatz and A. Kuppermann, J. Chem. Phys. **65**, 4668 (1976).

[64] A. J. C. Varandas, F. B. Brown, C. A. Mead, D. G. Truhlar, and N. C. Blais, J. Chem. Phys. **86**, 6258 (1987).

[65] A. I. Boothroyd, W. J. Keogh, P. G. Martin, and M. R. Peterson, J. Chem. Phys. **95**, 4343 (1991).

[66] A. I. Boothroyd, W. J. Keogh, P. G. Martin, and M. R. Peterson, J. Chem. Phys. **104**, 7139 (1996).

[67] Y.-S. M. Wu, A. Kuppermann, and J. B. Anderson, Phys. Chem. Chem. Phys. **1**, 929 (1999).

[68] D. L. Diedrich and J. B. Anderson, Science **258**, 786 (1992).

[69] G. C. Schatz, Ann. Rev. Phys. Chem. **39**, 317 (1988).

[70] W. R. Schulz and D. J. Le Roy, J. Chem. Phys. **42**, 3869 (1965).

[71] R. M. Marshall and J. H. Purnell, J. Chem. Soc. A 2301 (1968).

[72] R. D. Levine and S.-F. Wu, Chem. Phys. Lett. **11**, 557 (1971).

[73] R. D. Levine, Acc. Chem. res. **3**, 273 (1970).

[74] W. H. Miller, Adv. Chem. Phys. **30**, 99 (1975).

[75] P. A. Fraser and S. K. Burley, Eur. J. Phys. **3**, 230 (1982).

[76] J.-C. Nieh and J. J. Valentini, Phys. Rev. Lett. **60**, 519 (1988).

[77] J.-C. Nieh and J. J. Valentini, J. Chem. Phys. **92**, 1083 (1990).

[78] D. A. V. Kliner, D. E. Adelman, and R. N. Zare, J. Chem. Phys. **94**, 1069 (1991).

[79] W. H. Miller and J. Z. H. Zhang, J. Phys. Chem. **95**, 12 (1991).

[80] H. C. Longuett-Higgins, *Advances in Spectroscopy* (Interscience Publishers Inc., New York, 1961), Vol. II, pp. 429–472.

[81] C. A. Mead and D. G. Truhlar, J. Chem. Phys. **70**, 2284 (1979).

[82] C. A. Mead, J. Chem. Phys. **72**, 3839 (1980).

[83] Y. Aharonov and D. Bohm, Phys. Rev. **115**, 3 (1959).

[84] *Geometric Phases in Physics*, Vol. 5 of *Advanced Series in Mathematical Physics* (World Scientific, London, 1989).

[85] A. Kuppermann and Y.-S. M. Wu, Chem. Phys. Lett. **205**, 577 (1993).

[86] A. Kuppermann, in *Dynamics of Molecules and Chemical Reactions*, edited by R. E. Wyatt and J. Z. H. Zhang (Marcel Dekker Inc., New York, 1996).

[87] N. E. Shafer, Ph.D. thesis, Columbia University, 1990.

[88] N. E. Shafer, A. J. Orr-Ewing, W. R. Simpson, H. Xu, and R. N. Zare, Chem. Phys. Lett. **212**, 155 (1993).

[89] N. E. Shafer-Ray, A. J. Orr-Ewing, and R. N. Zare, J. Phys. Chem. **99**, 7591 (1995).

[90] R. N. Zare and D. R. Herschbach, Proc. IEEE **51**, 173 (1964).

[91] R. N. Zare, *Angular Momentum. Understanding Spatial Aspects in Chemistry and Physics* (John Wiley & Sons, New York, 1988).

[92] M. B. Robin, *Higher Excited States of Polyatomic Molecules* (Academic Press, New York, 1974), Vol. I and II.

[93] H. Sato, *Photodissociation of Simple Molecules in the Gas Phase* (Bunshin Publishing Co., Tokio, 1992).

[94] K. P. Huber and G. Herzberg, *Molecular Spectra and Molecular Structure IV. Constants of Diatomic Molecules* (Van Nostrand Reinhold Company, New York, 1979).

[95] S. H. S. Wilson, J. D. Howe, and M. N. R. Ashfold, Mol. Phys. **88**, 841 (1996).

[96] M. N. R. Ashfold, D. H. Mordaunt, and S. H. S. Wilson, *Advances in Photochemistry* (John Wiley & Sons Inc., New York, 1996), Vol. 21, pp. 217–295.

[97] G. P. Morley, I. R. Lambert, D. H. Mordaunt, S. H. S. Wilson, M. N. R. Ashfold, R. N. Dixon, and C. M. Western, J. Chem. Soc. Faraday Trans. **89**, 3865 (1993).

[98] L. Schnieder, K. Seekamp-Rahn, J. Borkowski, E. Wrede, K. H. Welge, F. J. Aoiz, L. Bañares, M. J. D'Mello, V. J. Herrero, V. Sáez Rábanos, and R. E. Wyatt, Science **269**, 207 (1995).

[99] W. Demtröder, *Laser Spectroscopy* $2^{nd}$ *ed.* (Springer, Berlin, 1996).

[100] K. L. Reid and A. J. McCaffery, J. Chem. Phys. **96**, 5789 (1992).

[101] T. L. D. Collins, A. J. McCaffery, J. P. Richardson, R. J. Wilson, and M. J. Wynn, J. Chem. Phys. **102**, 4419 (1995).

[102] A. J. McCaffery, Chem. Soc. Rev. **25**, 49 (1996).

[103] R. J. Wilson and A. J. McCaffery, Chem. Phys. Lett. **261**, 195 (1996).

[104] N. Billy, B. Girard, G. Gouédard, and J. Vigué, Laser Chem. **10**, 319 (1990).

[105] B. Girard, N. Billy, G. Gouédard, and J. Vigué, J. Chem. Phys. **95**, 4056 (1991).

[106] J. L. Kinsey, J. Chem. Phys. **66**, 2560 (1977).

[107] E. J. Murphy, J. H. Brophy, G. S. Arnold, W. L. Dimpfl, and J. L. Kinsey, J. Chem. Phys. **70**, 5910 (1979).

[108] E. J. Murphy, J. H. Brophy, and J. L. Kinsey, J. Chem. Phys. **74**, 331 (1981).

[109] J. A. Serri, J. L. Kinsey, and D. E. Pritchard, J. Chem. Phys. **75**, 663 (1981).

[110] M. Brouard, S. P. Duxon, P. A. Enríquez, R. Sayos, and J. P. Simons, J. Phys. Chem. **95**, 8169 (1991).

[111] M. Brouard, S. P. Duxon, P. A. Enríquez, and J. P. Simons, J. Chem. Phys **97**, 7414 (1992).

[112] M. Brouard, S. P. Duxon, P. A. Enríquez, and J. P. Simons, J. Chem. Soc. Faraday Trans. **89**, 1435 (1993).

[113] M. Brouard, S. P. Duxon, P. A. Enríquez, and J. P. Simons, Isr. J. Chem. **34**, 67 (1994).

[114] A. J. Alexander, Ph.D. thesis, University of Oxford, 1997.

[115] A. J. Alexander, F. J. Aoiz, L. Bañares, M. Brouard, J. Short, and J. P. Simons, J. Phys. Chem. A **101**, 7544 (1997).

[116] M. Brouard, D. W. Hughes, K. S. Kalogerakis, and J. P. Simons, J. Phys. Chem. A **102**, 9559 (1998).

[117] H. L. Kim, M. A. Wickramaaratchi, X. Zheng, and G. E. Hall, J. Chem. Phys. **101**, 2033 (1994).

[118] R. J. Cotter, *Time-of-flight Mass Spectrometry* (Americal Chemical Society, Washington DC, 1994).

[119] N. E. Shafer, H. Xu, R. P. Tuckett, M. Springer, and R. N. Zare, J. Phys. Chem. **98**, 3369 (1994).

[120] H. Xu, N. E. Shafer-Ray, F. Merkt, D. J. Hughes, M. Springer, R. P. Tuckett, and R. N. Zare, J. Chem. Phys. **103**, 5157 (1995).

[121] W. R. Simpson, A. J. Orr-Ewing, T. P. Rakitzis, S. A. Kandel, and R. N. Zare, J. Chem. Phys. **103**, 7299 (1995).

[122] W. C. Wiley and I. H. McLaren, Rev. Sci. Instrum. **26**, 1150 (1955).

[123] G. E. Yefchak, C. G. Enke, and J. F. Holland, Int. J. Mass Spect. and Ion Proc. **87**, 313 (1989).

[124] F. Chandezon, B. Huber, and C. Ristori, Rev. Sci. Instrum. **65**, 3344 (1994).

[125] R. I. Hall, I. Čadež, M. Landau, F. Pichou, and C. Schermann, Phys. Rev. Lett. **60**, 337 (1988).

[126] P. J. Eenshuistra, J. H. M. Bonnie, J. Los, and H. J. Hopman, Phys. Rev. Lett. **60**, 341 (1988).

[127] J. D. Buck, D. C. Robie, A. P. Hickman, D. J. Bamford, and W. K. Bischel, Phys. Rev. A **39**, 3932 (1989).

[128] D. C. Robie, L. E. Jusinski, and W. K. Bischel, Appl. Phys. Lett. **56**, 722 (1990).

[129] J. L. Wiza, Nucl. Instrum. Methods **162**, 587 (1979).

[130] E. H. Eberhardt, Appl. Optics **18**, 1418 (1979).

[131] V. D. Dimitriev, S. M. Luk'yanov, Y. É. Penionzhkevich, and D. K. Sattarov, Instruments and Experimental Techniques (translation of Pribori i Tekhnika Éksperimenta) **25**, 283 (1982).

[132] D. A. Dahl, *SIMION 3D version 6.0* (U.S. Department of Energy, Office of Energy Research, Idaho Falls, 1995).

[133] A. R. Waugh, J. Phys. E. (Sci. Instrum.) **11**, 49 (1978).

[134] B. A. Jacoby, D. E. Kotecki, and R. D. Lear, IEEE Trans. Nucl. Sci. **NS-30**, 4624 (1983).

[135] O. Almen, W. Hartmann, K. Frank, and J. Christiansen, J. Phys. E. (Sci. Instrum.) **22**, 382 (1989).

[136] M. C. Marconi, J. J. Roca, and G. J. Krausse, J. Phys. E. (Sci. Instrum.) **22**, 849 (1989).

[137] D. M. Bishop and L. M. Cheung, Adv. Quantum Chemistry **12**, 1 (1980).

[138] H. Pummer, H. Egger, T. S. Luk, T. Srinivasan, and C. K. Rhodes, Phys. Rev. A **28**, 795 (1983).

[139] H. Eichert and M. Fischer, Int. J. Hydrogen Energy **11**, 117 (1986).

[140] D. J. Rose and M. Clark, *Plasmas and Controlled Fusion* (Wiley, New York, 1961).

[141] E. W. Rothe, G. S. Ondrey, and P. Andresen, Opt. Comm. **58**, 113 (1986).

[142] W. W. Duley and D. A. Williams, *Interstellar Chemistry* (Academic Press, London, 1984).

[143] W. T. Huntress, Jr., Adv. At. Mol. Phys. **10**, 295 (1974).

[144] E. F. van Dishoeck and J. H. Black, Astroph. J. **334**, 771 (1988).

[145] P. P. Sorokin and J. H. Glownia, Chem. Phys. Lett. **234**, 1 (1995).

[146] P. C. Hinnen and W. Ubachs, Chem. Phys. Lett. **240**, 351 (1995).

[147] P. P. Sorokin and J. H. Glownia, Astrophys. J. **473**, 900 (1996).

[148] P. Essenwanger and H. P. Gush, Can. J. Phys. **62**, 1680 (1984).

[149] W. Kołos and L. Wolniewicz, J. Chem. Phys. **43**, 2429 (1965).

[150] W. Kołos and L. Wolniewicz, J. Chem. Phys. **48**, 3672 (1968).

[151] W. Kołos and L. Wolniewicz, J. Chem. Phys. **50**, 3228 (1969).

[152] L. Wolniewicz and K. Dressler, J. Mol. Spec. **67**, 416 (1977).

[153] W. Kołos and L. Wolniewicz, J. Mol. Spec. **91**, 128 (1982).

[154] L. Wolniewicz, J. Chem. Phys. **78**, 6173 (1983).

[155] K. Dressler and L. Wolniewicz, Can. J. Phys. **62**, 1706 (1984).

[156] L. Wolniewicz and K. Dressler, J. Chem. Phys. **100**, 444 (1994).

[157] L. Wolniewicz, J. Chem. Phys. **105**, 10691 (1996).

[158] T. E. Sharp, Atomic Data **2**, 119 (1971).

[159] R. Hilbig and R. Wallenstein, IEEE J. Quantum Electronics **QE-17**, 1566 (1981).

[160] E. E. Marinero, R. Vasudev, and R. N. Zare, J. Chem. Phys. **78**, 692 (1983).

[161] C. T. Rettner, E. E. Marinero, R. N. Zare, and A. H. Kung, J. Phys. Chem. **88**, 4459 (1984).

[162] C. R. Vidal, *Tunable Lasers* (Springer-Verlag Topics in Applied Physics, Berlin, 1987), Vol. 59, pp. 57–113.

[163] G. Hilber, A. Lago, and R. Wallenstein, J. Opt. Soc. Am. B **4**, 1753 (1987).

[164] T. Okada, T. Aoi, M. Maeda, K. Muraoka, and M. Akazari, Japanese J. App. Phys. Part I **27**, 1550 (1988).

[165] J. P. Marangos, N. Shen, H. Ma, M. H. R. Hutchinson, and J. P. Connerade, J. Opt. Soc. Am. B **7**, 1254 (1990).

[166] C. E. M. Strauss and D. J. Funk, Opt. Lett. **16**, 1192 (1991).

[167] P. C. Hinnen, S. E. Werners, S. Stolte, W. Hogervorst, and W. Ubachs, Phys. Rev. A **52**, 4425 (1995).

[168] P. C. Hinnen, Ph.D. thesis, Vrije Universiteit te Amsterdam, 1997.

[169] E. Reinhold, W. Hogervorst, W. Ubachs, and L. Wolniewicz, submitted to J. Chem. Phys. (1999).

[170] E. Reinhold, A. de Lange, W. Hogervorst, and W. Ubachs, J. Chem. Phys. **109**, 9772 (1998).

[171] E. Reinhold, W. Hogervorst, and W. Ubachs, Chem. Phys. Lett. **296**, 411 (1998).

[172] K. Tsukiyama, S. Shimizu, and T. Kasuya, J. Mol. Spec. **155**, 352 (1992).

[173] K. Tsukiyama, J. Ishii, and T. Kasuya, J. Chem. Phys. **97**, 875 (1992).

[174] H. Suzuki, M. Nakata, Y. Ogi, and K. Tsukiyama, J. Mol. Spec. **191**, 142 (1998).

[175] F. Merkt, H. Xu, and R. N. Zare, J. Chem. Phys. **104**, 950 (1996).

[176] H. Xu, Ph.D. thesis, Stanford University, 1998.

[177] W. A. Chupka, J. Chem. Phys. **98**, 4520 (1993).

[178] F. Merkt and R. N. Zare, J. Chem. Phys. **101**, 3495 (1994).

[179] L. A. Pinnaduwage and Y. Zhu, Chem. Phys. Lett. **277**, 147 (1997).

[180] L. Schnieder, W. Meier, K. H. Welge, M. N. R. Ashfold, and C. M. Western, J. Chem. Phys. **92**, 7027 (1990).

[181] W. M. McClain, Acc. Chem. Res. **7**, 129 (1974).

[182] W. M. McClain and R. A. Harris, *Excited States* (Academic Press Inc., New York, 1977), pp. 1–56.

[183] R. L. Swofford and A. C. Albrecht, Ann. Rev. Phys. Chem. **29**, 421 (1978).

[184] W. K. Bischel, J. Bokor, D. J. Kligler, and C. K. Rhodes, IEEE J. Quantum Electronics **QE-15**, 380 (1979).

[185] D. M. Friedrich and W. M. McClain, Ann. Rev. Phys. Chem. **31**, 559 (1980).

[186] S. H. Lin, Y. Fujimura, H. J. Neusser, and E. W. Schlag, *Multiphoton Spectroscopy of Molecules*, *Quantum Electronics - Principles and Applications* (Academic Press, London, 1984).

[187] C. R. Scheper, W. J. Buma, C. A. de Lange, and W. J. van der Zande, J. Chem. Phys. **109**, 8319 (1998).

[188] S. T. Pratt, P. M. Dehmer, and J. L. Dehmer, J. Chem. Phys. **85**, 3379 (1986).

[189] S. T. Pratt, P. M. Dehmer, and J. L. Dehmer, J. Chem. Phys. **86**, 1727 (1987).

[190] W. Richter, *Dye Lasers 25 Years* (Springer Verlag, Berlin, 1961), Vol. 70 of Topics in Applied Physics, pp. 183–194.

[191] D. K. Veirs, G. M. Rosenblatt, and J. J. Valentini, J. Chem. Phys. **83**, 1605 (1985).

[192] D. J. Kligler and C. K. Rhodes, Phys. Rev. Lett. **40**, 309 (1978).

[193] E. E. Marinero, C. T. Rettner, and R. N. Zare, Phys. Rev. Lett. **48**, 1323 (1982).

[194] B. Ritchie, E. J. McGuire, J. M. Peek, and C. W. Hand, J. Chem. Phys. **77**, 877 (1982).

[195] W. M. Huo and R. L. Jaffe, Chem. Phys. Lett. **101**, 463 (1983).

[196] S. L. Anderson, G. D. Kubiak, and R. N. Zare, Chem. Phys. Lett. **105**, 22 (1984).

[197] D. W. Chandler and L. R. Thorne, J. Chem. Phys. **85**, 1733 (1986).

[198] H. Rudolph, D. L. Lynch, S. N. Dixit, V. McKoy, and W. M. Huo, J. Chem. Phys. **86**, 1748 (1987).

[199] P. Senn and K. Dressler, J. Chem. Phys. **87**, 1205 (1987).

[200] K.-D. Rinnen, D. A. V. Kliner, R. N. Zare, and W. M. Huo, Isr. J. Chem. **29**, 369 (1989).

[201] W. M. Huo, K.-D. Rinnen, and R. N. Zare, J. Chem. Phys. **95**, 205 (1991).

[202] K.-D. Rinnen, M. A. Buntine, D. A. V. Kliner, R. N. Zare, and W. M. Huo, J. Chem. Phys. **95**, 214 (1991).

[203] A. J. Heck, W. M. Huo, R. N. Zare, and D. W. Chandler, J. Mol. Spectrosc. **173**, 452 (1995).

[204] K. R. Lykke and B. D. Kay, J. Chem. Phys. **95**, 2252 (1991).

[205] D. S. Zakheim and P. M. Johnson, Chem. Phys. **46**, 263 (1980).

[206] P. Agostini, A. T. Georges, S. E. Wheatley, P. Lambropoulos, and M. D. Levenson, J. Phys. B (Atom. Mol. Phys.) **11**, 1733 (1978).

[207] J. Xie and R. N. Zare, J. Chem. Phys. **93**, 3033 (1990).

[208] J. Xie and R. N. Zare, J. Chem. Phys. **97**, 2891 (1992).

[209] R. L. Swofford and W. M. McClain, Chem. Phys. Lett. **34**, 455 (1975).

[210] S. Speiser and J. Jortner, Chem. Phys. Lett. **44**, 399 (1976).

[211] R. G. Bray and R. M. Hochstrasser, Mol. Phys. **31**, 1199 (1976).

[212] J. B. Halpern, H. Zacharias, and R. Wallenstein, J. Mol. Spec. **79**, 1 (1980).

[213] M. Hippler, Mol. Phys. **97**, 105 (1999).

[214] K. m. Chen and E. S. Yeung, J. Chem. Phys. **69**, 43 (1978).

[215] S. N. Dixit and V. McKoy, J. Chem. Phys. **82**, 3546 (1985).

[216] H. Meyer, Chem. Phys. Lett. **230**, 510 (1994).

[217] F. Metz, W. E. Howard, L. Wunsch, H. J. Neusser, and E. W. Schlag, Proc. Roy. Soc. Lond. A **363**, 381 (1978).

[218] B. Girard, G. O. Sitz, and R. N. Zare, J. Chem. Phys **97**, 26 (1992).

[219] S. Xu, G. Sha, J. He, and C. Zhang, J. Chem. Phys. **100**, 1866 (1993).

[220] A. C. Kummel, G. O. Sitz, and R. N. Zare, J. Chem. Phys. **85**, 6874 (1986).

[221] A. C. Kummel, G. O. Sitz, and R. N. Zare, J. Chem. Phys. **88**, 6707 (1988).

[222] U. Fano and J. H. Macek, Rev. Mod. Phys. **45**, 553 (1973).

[223] I. V. Hertel and W. Stoll, Adv. At. Mol. Phys. **13**, 113 (1978).

[224] Y. Mo and T. Suzuki, J. Chem. Phys. **109**, 4691 (1998).

[225] T. P. Rakitzis, Ph.D. thesis, Stanford University, 1997.

[226] D. A. Varshalovich, A. N. Moskalev, and V. K. Khersonskii, *Quantum Theory of Angular Momentum: Irreducible Tensors, Spherical Harmonics, Vector Coupling Coefficients, 3nj Symbols* (World Scientific Pub., Singapore, 1988).

[227] C. H. Townes and A. L. Schawlow, *Microwave Spectroscopy* (Dover Publications Inc., New York, 1975).

[228] W. E. Quinn, J. M. Baker, J. T. LaTourrette, and N. F. Ramsey, Phys. Rev. **112**, 1929 (1958).

[229] R. F. Code and N. F. Ramsey, Phys. Rev. A **4**, 1945 (1971).

[230] R. Altkorn, Ph.D. thesis, Stanford University, 1984.

[231] R. Altkorn, R. N. Zare, and C. H. Greene, Mol. Phys. **55**, 1 (1985).

[232] A. J. Orr-Ewing, W. R. Simpson, T. P. Rakitzis, and R. N. Zare, Israel J. Chem. **34**, 95 (1994).

[233] C. Cornaggia, A. Giusti-Suzor, and C. Jungen, J. Chem. Phys. **87**, 3934 (1987).

[234] E. F. McCormack, S. T. Pratt, J. L. Dehmer, and P. M. Dehmer, J. Chem. Phys. **92**, 4734 (1990).

[235] T. F. Hanisco and A. C. Kummel, J. Phys. Chem. **97**, 8565 (1991).

[236] T. F. Hanisco, C. Yan, and A. C. Kummel, J. Phys. Chem. **96**, 2982 (1992).

[237] C. Jungen, I. Dabrowski, G. Herzberg, and M. Vervloet, J. Chem. Phys. **93**, 2289 (1990).

[238] G. Herzberg, *Molecular Spectra and Molecular Structure I. Spectra of Diatomic Molecules* (Krieger Publishing Co., Malabar, reprinted in 1989).

[239] H. Lefebvre-Brion and R. W. Field, *Perturbations in the Spectra of Diatomic Molecules* (Academic Press, Orlando, 1986).

[240] B. P. Roe, *Probability and Statistics in Experimental Physics* (Springer-Verlag, New York, 1992).

[241] W. R. Simpson, Ph.D. thesis, Stanford University, 1994.

[242] P. R. Bevington, *Data Reduction and Error Analysis for the Physical Sciences* (McGraw-Hill, New York, 1969).

[243] W. H. Press, B. P. Flannery, S. A. Teukolsky, and W. T. Vetterlich, *Numerical Recipes in Fortran* (Cambridge University Press, Cambridge, 1986).

[244] J. H. Kalivas, *Adaption of Simulated Annealing Problems to Chemical Optimization Problems* (Elsevier, Amsterdam, 1995).

[245] R. M. Bevensee, *Maximum Entropy Solutions to Scientific Problems* (Prentice Hall, New Jersey, 1993).

[246] B. J. Huebert and R. M. Martin, J. Phys. Chem. **72**, 3046 (1968).

[247] J. B. Nee, M. Suto, and L. C. Lee, J. Chem. Phys. **85**, 4919 (1986).

[248] Z. Xu, B. Koplitz, and C. Wittig, J. Phys. Chem. **92**, 5518 (1988).

[249] T. Kinugawa and T. Arikawa, J. Chem. Phys. **96**, 4801 (1992).

[250] P. M. Regan, S. R. Langford, A. J. Orr-Ewing, and M. N. R. Ashfold, J. Chem. Phys. **110**, 281 (1999).

[251] G. C. Bjorklund, C. P. Ausschnitt, R. R. Freeman, and R. H. Storz, Appl. Phys. Lett. **33**, 54 (1978).

[252] Y. Matsumi and M. Kawasaki, J. Chem. Phys. **93**, 2481 (1991).

[253] Y.-L. Huang and R. J. Gordon, J. Chem. Phys. **94**, 2640 (1991).

[254] K. Tonokura, N. Shafer, Y. Matsumi, and M. Kawasaki, J. Chem. Phys. **95**, 3394 (1991).

[255] J. J. Lin, D. W. Hwang, Y. T. Lee, and X. Yang, J. Chem. Phys. **109**, 1758 (1998).

[256] A. T. J. B. Eppink and D. H. Parker, Rev. Sci. Instrum. **68**, 3477 (1997).

[257] A. T. J. B. Eppink, D. H. Parker, M. H. Janssen, B. Buijsse, and W. J. van der Zande, J. Chem. Phys. **108**, 1305 (1998).

[258] B. Buijsse, W. J. van der Zande, A. T. J. B. Eppink, D. H. Parker, B. R. Lewis, and S. T. Gibson, J. Chem. Phys. **108**, 7229 (1998).

[259] D. J. Bamford, M. J. Dyer, and W. K. Bischel, Phys. Rev. A **36**, 3497 (1987).

[260] D. A. V. Kliner, K. D. Rinnen, and R. N. Zare, J. Chem. Phys. **90**, 4625 (1989).

[261] D. A. V. Kliner, K.-D. Rinnen, M. A. Buntine, D. A. Adelman, and R. N. Zare, J. Chem. Phys. **95**, 1663 (1991).

[262] P. M. Aker and J. J. Valentini, J. Phys. Chem. **97**, 2078 (1993).

[263] P. M. Aker, G. J. Germann, and J. J. Valentini, J. Chem. Phys. **96**, 2756 (1992).

[264] P. M. Aker, G. J. Germann, K. D. Tabor, and J. J. Valentini, J. Chem . Phys. **90**, 4809 (1989).

[265] P. M. Aker, G. J. Germann, and J. J. Valentini, J. Chem. Phys. **90**, 4795 (1989).

[266] P. A. Jansson, *Deconvolution with Applications to Spectroscopy* (Academic Press, Orlando, 1984).

[267] C. E. Moore, *Atomic Energy Levels* (National Bureau of Standards, Washington, 1971), Vol. III.

[268] J. Bokor, R. R. Freeman, J. C. White, and R. H. Storz, Phys. Rev. A **24**, 612 (1981).

[269] J. E. M. Goldsmith, R. J. M. Anderson, and L. R. Williams, Opt. Lett. **15**, 78 (1990).

[270] Chemical Rubber Co., *CRC Handbook of Chemistry and Physics* (CRC Press, Cleveland, 1998), Vol. 78.

[271] R. Callaghan and R. J. Gordon, J. Chem. Phys. **93**, 4624 (1990).

[272] Á. Kvaran, Á. Logadóttir, and H. Wang, J. Chem. Phys. **109**, 5856 (1998).

[273] D. S. Green, G. A. Bickel, and S. C. Wallace, J. Mol. Spec. **150**, 303 (1991).

[274] D. S. Green, G. A. Bickel, and S. C. Wallace, J. Mol. Spec. **150**, 354 (1991).

[275] D. S. Green, G. A. Bickel, and S. C. Wallace, J. Mol. Spec. **150**, 388 (1991).

[276] S. A. Wright and J. D. McDonald, J. Chem. Phys. **101**, 238 (1994).

[277] S. T. Pratt and M. L. Ginter, J. Chem. Phys. **102**, 1882 (1995).

[278] R. M. Jonkman, G. J. Prangsma, I. Ertas, H. F. P. Knaap, and J. J. M. Beenakker, Physica **38**, 441 (1968).

[279] R. M. Jonkman, G. J. Prangsma, R. A. J. Keijser, R. A. Aziz, and J. J. M. Beenakker, Physica **38**, 451 (1968).

[280] L. M. Valley and R. C. Amme, J. Chem. Phys. **50**, 3190 (1969).

[281] J. D. Lambert, *Vibrational and Rotational Relaxation in Gases* (Clarendon Press, Oxford, 1977).

[282] U. Buck, Comments At. Mol. Phys. **17**, 143 (1986).

[283] K. C. Smyth, G. J. Rosasco, and W. S. Hurst, J. Chem. Phys. **87**, 1001 (1987).

[284] R. M. Jonkman, G. J. Prangsma, R. A. J. Keijser, H. F. P. Knaap, and J. J. M. Beenakker, Physica **38**, 456 (1968).

[285] P. McGuire and D. J. Kouri, J. Chem. Phys. **60**, 2488 (1974).

[286] P. M. Agrawal and M. P. Saksena, J. Phys. B (Atom. Molec. Phys.) **8**, 1575 (1975).

[287] J. I. Steinfeld, P. Ruttenberg, G. Millot, G. Fanjoux, and B. Lavorel, J. Phys. Chem. **95**, 9638 (1991).

[288] I. F. Silvera, Rev. Mod. Phys. **52**, 393 (1980).

[289] C. Yu, K. B. Whaley, C. S. Hogg, and S. J. Sibener, J. Chem. Phys. **83**, 4217 (1985).

[290] N. S. Sullivan, D. Zhou, and C. M. Edwards, Cryogenics **30**, 734 (1990).

[291] E. Ilisca, Prog. Surf. Sci. **41**, 217 (1992).

[292] W. J. van der Zande, R. Zhang, and R. N. Zare, in *Spectral Line Shapes*, edited by L. Frommhold and J. W. Keto (American Institute of Physics, Austin TX, 1990), Vol. 6, pp. 301–310.

[293] W. J. van der Zande, R. Zhang, R. N. Zare, K. G. McKendrick, and J. J. Valentini, J. Phys. Chem. **95**, 8205 (1991).

[294] F. J. Aoiz, M. Brouard, P. A. Enríquez, and R. Sayos, J. Chem. Soc. Faraday Trans. **89**, 1427 (1993).

[295] S. Kennedy, K. Dharmesena, S. Moser, M. Auzinsh, and N. E. Shafer-Ray, Chem. Phys. **244**, 449 (1999).

[296] G. M. McClelland, K. L. Saenger, J. J. Valentini, and D. R. Herschbach, J. Phys. Chem. **83**, 947 (1979).

[297] S. DePaul, D. Pullman, and B. Friedrich, J. Phys. Chem. **97**, 2167 (1993).

[298] D. M. Lubman, C. T. Rettner, and R. N. Zare, J. Phys. Chem. **86**, 1129 (1982).

[299] M. P. Sinha, C. D. Caldwell, and R. N. Zare, J. Chem. Phys. **61**, 491 (1974).

[300] A. G. Visser, J. P. Bekooy, L. K. van der Meij, C. de Vreugd, and J. Korving, Chem. Phys. **20**, 391 (1977).

[301] W. R. Sanders and J. B. Anderson, J. Phys. Chem. **88**, 4479 (1984).

[302] D. P. Pullmann, B. Friedrich, and D. R. Herschbach, J. Chem. Phys. **93**, 3224 (1990).

[303] M. J. Weida and D. J. Nesbitt, J. Chem. Phys. **100**, 6372 (1994).

[304] V. Aquilanti, D. Ascenzi, D. Cappelletti, and F. Pirani, Nature **371**, 399 (1994).

[305] S. Harich and A. M. Wodtke, J. Chem. Phys. **107**, 5983 (1997).

[306] V. Aquilanti, D. Ascenzi, M. Bartolomei, D. Cappelletti, S. Cavalli, M. de Castro Vítores, and F. Pirani, Phys. Rev. Lett. **82**, 69 (1999).

[307] C. T. Rettner, E. E. Marinero, and R. N. Zare, *Electronic and Atomic Collisions* (Elsevier Science Publishers, North Holland, Amsterdam, 1984), pp. 51–61.

[308] N. C. Blais and D. G. Truhlar, Chem. Phys. Lett. **102**, 120 (1983).

[309] N. C. Blais and D. G. Truhlar, J. Chem. Phys. **83**, 2201 (1985).

[310] D. P. Gerrity and J. J. Valentini, J. Chem. Phys. **81**, 1298 (1984).

[311] D. P. Gerrity and J. J. Valentini, J. Chem. Phys. **82**, 1323 (1985).

[312] D. L. Phillips, H. B. Levene, and J. J. Valentini, J. Chem. Phys. **90**, 1600 (1989).

[313] H. B. Levene, D. L. Phillips, J.-C. Nieh, D. P. Gerrity, and J. J. Valentini, Chem. Phys. Lett. **143**, 317 (1988).

[314] R. S. Blake, K.-D. Rinnen, D. A. V. Kliner, and R. N. Zare, Chem. Phys. Lett. **153**, 365 (1988).

[315] K.-D. Rinnen, D. A. V. Kliner, R. S. Blake, and R. N. Zare, Chem. Phys. Lett. **153**, 371 (1988).

[316] D. A. V. Kliner, K.-D. Rinnen, and R. N. Zare, Chem. Phys. Lett. **166**, 107 (1990).

[317] D. E. Adelman, H. Xu, and R. N. Zare, Chem. Phys. Lett. **203**, 573 (1993).

[318] D. A. V. Kliner and R. N. Zare, J. Chem. Phys. **92**, 2107 (1990).

[319] D. Neuhauser, R. S. Judson, D. J. Kouri, D. E. Adelman, N. E. Shafer, D. A. V. Kliner, and R. N. Zare, Science **257**, 519 (1992).

[320] D. E. Adelman, N. E. Shafer, D. A. V. Kliner, and R. N. Zare, J. Chem. Phys. **97**, 7323 (1992).

[321] Y.-S. M. Wu and A. Kuppermann, Chem. Phys. Lett. **201**, 178 (1993).

[322] N. C. Blais and D. G. Truhlar, Chem. Phys. Lett. **162**, 503 (1989).

[323] F. J. Aoiz, L. Bañares, T. Díez-Rojo, V. J. Herrero, and V. Sáez Rábanos, J. Phys. Chem. **100**, 4071 (1996).

[324] R. B. Bernstein and R. D. Levine, J. Chem. Phys. **57**, 434 (1972).

[325] R. D. Levine, B. R. Johnson, and R. B. Bernstein, Chem. Phys. Lett. **19**, 1 (1973).

[326] R. D. Levine and R. B. Bernstein, Acc. Chem. Res. **7**, 393 (1974).

[327] R. E. Wyatt, Chem. Phys. Lett. **34**, 167 (1975).

[328] J. L. Kinsey, J. Chem. Phys. **54**, 1206 (1971).

[329] E. Zamir, R. D. Levine, and R. B. Bernstein, Chem. Phys. Lett. **107**, 217 (1984).

[330] R. E. Wyatt and J. Z. H. Zhang, *Dynamics of Molecules and Chemical Reactions* (Marcel Dekker Inc., New York, 1996).

[331] M. N. R. Ashfold and J. E. Baggott, *Bimolecular Collisions*, *Advances in Gas-Phase Photochemistry and Kinetics* (Royal Society of Chemistry, London, 1989).

[332] D. C. Clary, *The Theory of Chemical Reaction Dynamics*, *NATO ASI Series* (Reidel Publishing Company, Dordrecht, 1985).

[333] D. G. Truhlar, *Potential Energy Surfaces and Dynamics Calculations for Chemical Reactions and Molecular Energy Transfer* (Plenum Press, New York, 1981).

[334] R. B. Bernstein, *Atom-Molecule Collision Theory: A Guide for the Experimentalist* (Plenum Press, New York, 1979).

[335] K. Tsukiyama, B. Katz, and R. Bersohn, J. Chem. Phys. **84**, 1034 (1986).

[336] G. W. Johnson, B. Katz, T. Tsukiyama, and R. Bersohn, J. Phys. Chem. **91**, 5445 (1987).

[337] U. Gerlach-Meyer, K. Kleinermanns, E. Linnebach, and J. Wolfrum, J. Chem. Phys. **86**, 3047 (1987).

[338] R. A. Brownsword, M. Hillenkamp, T. Laurent, H.-R. Wolpp, J. Wolfrum, R. K. Vatsa, and H.-S. Yoo, J. Phys. Chem. A **101**, 6448 (1997).

[339] R. Götting, H. R. Mayne, and J. P. Toennies, J. Chem. Phys. **80**, 2230 (1984).

[340] L. Schnieder, K. Seekamp-Rahn, E. Wrede, and K. H. Welge, J. Chem. Phys. **107**, 6175 (1997).

[341] E. Wrede and L. Schnieder, J. Chem. Phys. **107**, 786 (1997).

[342] L. Bañares, F. J. Aoiz, V. J. Herrero, M. J. D'Mello, B. Niederjohann, K. Seekamp-Rahn, E. Wrede, and L. Schnieder, J. Chem. Phys. **108**, 6160 (1998).

[343] F. J. Aoiz, L. Bañares, M. J. D'Mello, V. J. Herrero, V. Sáez Rábanos, L. Schnieder, and R. E. Wyatt, J. Chem. Phys. **101**, 5781 (1994).

[344] Y.-S. M. Wu and A. Kuppermann, Chem. Phys. Lett. **235**, 105 (1995).

[345] M. P. de Miranda, D. C. Clary, J. F. Castillo, and D. E. Manolopoulos, J. Chem. Phys. **108**, 3142 (1998).

[346] M. P. de Miranda, F. J. Aoiz, L. Bañares, and V. Sáez Rábanos, submitted to J. Chem. Phys. (1999).

[347] F. Fernández-Alonso, B. D. Bean, and R. N. Zare, J. Chem. Phys. **111**, 1022 (1999).

[348] W. R. Simpson, A. J. Orr-Ewing, and R. N. Zare, Chem. Phys. Lett. **212**, 163 (1993).

[349] W. R. Simpson, T. P. Rakitzis, S. A. Kandel, T. Lev-On, and R. N. Zare, J. Phys. Chem. **100**, 7938 (1996).

[350] S. A. Kandel, T. P. Rakitzis, T. Lev-On, and R. N. Zare, J. Chem. Phys. **105**, 7550 (1996).

[351] S. A. Kandel, T. P. Rakitzis, T. Lev-On, and R. N. Zare, Chem. Phys. Lett. **265**, 121 (1996).

[352] S. A. Kandel, T. P. Rakitzis, T. Lev-On, and R. N. Zare, J. Phys. Chem. A **102**, 2270 (1998).

[353] T. P. Rakitzis, S. A. Kandel, T. Lev-On, and R. N. Zare, J. Chem. Phys. **107**, 9392 (1997).

[354] T. P. Rakitzis, S. A. Kandel, and R. N. Zare, J. Chem. Phys. **107**, 9382 (1997).

[355] A. J. Orr-Ewing, W. R. Simpson, T. P. Rakitzis, S. A. Kandel, and R. N. Zare, J. Chem. Phys. **106**, 5961 (1997).

[356] S. A. Kandel, Ph.D. thesis, Stanford University, 1998.

[357] *Stereodynamics Issue*, J. Phys. Chem. **91**, 5365 (1987).

[358] *Stereodynamics Issue*, J. Chem. Soc. Faraday Trans. **85**, 925 (1989).

[359] G. E. Hall and P. L. Houston, Ann. Rev. Phys. Chem. **40**, 375 (1989).

[360] *Richard B. Bernstein Memorial Issue on Molecular Dynamics*, J. Phys. Chem. **95**, 7961 (1991).

[361] *Orientation and Polarization Effects in Chemical Reaction Dynamics*, J. Chem. Soc. Faraday Trans. **89**, 1401 (1993).

[362] A. J. Orr-Ewing and R. N. Zare, Ann. Rev. Phys. Chem. **45**, 315 (1994).

[363] M. Brouard and J. P. Simons, *The Chemical Dynamics and Kinetics of Small Radicals* (Academic Press Inc., World Scientific Pub., 1995), pp. 795–841.

[364] A. J. Orr-Ewing and R. N. Zare, *The Chemical Dynamics and Kinetics of Small Radicals* (Academic Press Inc., World Scientific Pub., 1995), pp. 936–1063.

[365] *Stereodynamics of Chemical Reactions*, J. Phys. Chem. A **101**, 7461 (1997).

[366] E. Wrede, L. Schnieder, K. H. Welge, L. Bañares, and V. J. Herrero, Chem. Phys. Lett. **265**, 129 (1997).

[367] E. Wrede, L. Schnieder, K. H. Welge, F. J. Aoiz, L. Bañares, V. J. Herrero, B. Martínez-Haya, and V. Sáez Rábanos, J. Chem. Phys. **106**, 7862 (1997).

[368] E. Wrede, L. Schnieder, K. H. Welge, F. J. Aoiz, L. Bañares, J. F. Castillo, B. Martínez-Haya, and V. J. Herrero, J. Chem. Phys. **110**, 9971 (1999).

[369] M. A. Young, J. Phys. Chem. **97**, 13508 (1993).

[370] M. A. Young, J. Phys. Chem. **98**, 7790 (1994).

[371] M. A. Young, J. Chem. Phys. **102**, 7925 (1995).

[372] B. Lepetit and A. Kuppermann, Chem. Phys. Lett. **166**, 581 (1990).

[373] Y.-S. M. Wu, A. Kuppermann, and B. Lepetit, Chem. Phys. Lett. **186**, 319 (1991).

[374] A. Kuppermann, Faraday Disc. Chem. Soc. (Chemical Reaction Theory) **110**, 212 (1998).

[375] A. Kuppermann, Faraday Disc. Chem. Soc. (Chemical Reaction Theory) **110**, 217 (1998).

[376] R. D. Levine, J. Phys. Chem. **94**, 8872 (1990).

[377] R. D. Levine and R. B. Bernstein, Chem. Phys. Lett. **105**, 467 (1984).

[378] J. G. Muga and R. D. Levine, Chem. Phys. Lett. **162**, 7 (1989).

[379] J. G. Muga and R. D. Levine, J. Chem. Soc. Faraday Trans. **86**, 1669 (1990).

[380] F. J. Aoiz, V. J. Herrero, and V. Sáez Rábanos, J. Chem. Phys. **97**, 7423 (1992).

[381] F. J. Aoiz, V. J. Herrero, O. Puentedura, and V. Sáez Rábanos, Chem. Phys. Lett. **198**, 321 (1992).

[382] F. J. Aoiz, V. J. Herrero, and V. Sáez Rábanos, J. Chem. phys. **94**, 7991 (1991).

[383] S. L. Mielke, D. G. Truhlar, and D. W. Schwenke, J. Phys. Chem. **98**, 1053 (1994).

[384] M. H. M. Janssen and S. Stolte, J. Phys. Chem. **91**, 5480 (1987).

[385] D. R. Herschbach, Applied Optics (Supplement on Chemical Lasers) 128 (1965).

[386] D. R. Herschbach, Adv. Chem. Phys. **10**, 319 (1966).

[387] R. D. Levine and R. B. Bernstein, Isr. J. Chem. **7**, 315 (1969).

[388] R. Grice, Mol. Phys. **19**, 501 (1970).

[389] R. Grice and D. R. Hardin, Mol. Phys. **21**, 805 (1971).

[390] J. L. Kinsey, G. H. Kwei, and D. R. Herschbach, J. Chem. Phys. **64**, 1914 (1976).

[391] I. Schetchter and R. D. Levine, J. Chem. Soc. Faraday Trans. 2 **85**, 1059 (1989).

[392] R. Gengenbach, C. Hahn, and J. P. Toennies, J. Chem. Phys. **62**, 3620 (1975).

[393] K. T. Tang and J. P. Toennies, Chem. Phys. Lett **151**, 301 (1988).

[394] H. Partridge, C. W. Bauschlicher Jr., J. R. Stallcop, and E. Levin, J. Chem. Phys. **99**, 5951 (1993).

[395] I. Schechter, R. Kosloff, and R. D. Levine, Chem. Phys. Lett. **121**, 297 (1985).

[396] I. Schechter, R. Kosloff, and R. D. Levine, J. Phys. Chem. **90**, 1006 (1986).

[397] G. H. Kwei and D. R. Herschbach, J. Phys. Chem. **83**, 1550 (1979).

[398] I. R. Elsum and R. G. Gordon, J. Chem. Phys. **76**, 3009 (1982).

[399] I. Schechter, R. D. Levine, and R. G. Gordon, J. Phys. Chem. **95**, 8201 (1991).

[400] A. Siegel and A. Schultz, J. Chem. Phys. **76**, 4513 (1982).

[401] C. Noda and R. N. Zare, J. Chem. Phys. **86**, 3968 (1987).

[402] W. S. Hartree, J. P. Simons, and González-Ureña, J. Chem. Soc. Faraday Trans. **86**, 17 (1990).

[403] P. H. Vaccaro, A. A. Tsekouras, D. Zhao, C. A. Leach, and R. N. Zare, J. Chem. Phys. **96**, 2786 (1992).

[404] A. A. Tsekouras, C. A. Leach, K. S. Kalogerakis, and R. N. Zare, J. Chem. Phys. **97**, 7220 (1992).

[405] K. S. Kalogerakis and R. N. Zare, J. Chem. Phys. **104**, 7947 (1996).